Government of Western Australia

Department of
**Mines and Petroleum**

REPORT
155

# UNRAVELLING THE UPPER-AMPHIBOLITE FACIES GLENBURGH GOLD DEPOSIT, GASCOYNE PROVINCE — EVIDENCE FOR METAMORPHOSED MINERALIZATION

by LK Roche

Geological Survey of Western Australia

Government of **Western Australia**
Department of **Mines and Petroleum**

**REPORT 155**

# UNRAVELLING THE UPPER-AMPHIBOLITE FACIES GLENBURGH GOLD DEPOSIT, GASCOYNE PROVINCE — EVIDENCE FOR METAMORPHOSED MINERALIZATION

**by**
**LK Roche**

**Perth 2016**

**Geological Survey of Western Australia**

**MINISTER FOR MINES AND PETROLEUM**
**Hon. Bill Marmion MLA**

**DIRECTOR GENERAL, DEPARTMENT OF MINES AND PETROLEUM**
**Richard Sellers**

**EXECUTIVE DIRECTOR, GEOLOGICAL SURVEY OF WESTERN AUSTRALIA**
**Rick Rogerson**

**REFERENCE**
**The recommended reference for this publication is:**
Roche, LK 2016, Unravelling the upper-amphibolite facies Glenburgh gold deposit, Gascoyne Province — evidence for metamorphosed mineralization: Geological Survey of Western Australia, Report 155, 44p.

**National Library of Australia Cataloguing-in-Publication entry**

| | |
|---|---|
| **Creator**: | Roche, L. K., author. |
| **Title:** | Unravelling the upper-amphibolite facies Glenburgh gold deposit : evidence for metamorphosed mineralization / LK Roche. |
| **ISBN:** | 9781741686500 (ebook) |
| **Subjects:** | Amphibolite–Western Australia–Gascoyne River Region.<br>Gold ores–Geology–Western Australia–Gascoyne River Region.<br>Geology–Western Australia–Gascoyne River Region |
| **Dewey Decimal Classification:** | 553.4109941 |

Grid references in this publication refer to the Geocentric Datum of Australia 1994 (GDA94). Locations mentioned in the text are referenced using Map Grid Australia (MGA) coordinates, Zone 50. All locations are quoted to at least the nearest 100 m.



Copy editor: F Eddison
Cartography: AK Symonds, J Peng
Desktop publishing: RL Hitchings

**Published 2016 by Geological Survey of Western Australia**
This Report is published in digital format as part of a digital dataset on USB, and is available online at <www.dmp.wa.gov.au/GSWApublications>.

**Further details of geological publications and maps produced by the Geological Survey of Western Australia are available from:**
Information Centre | Department of Mines and Petroleum | 100 Plain Street | EAST PERTH | WESTERN AUSTRALIA 6004
Telephone: +61 8 9222 3459 Facsimile: +61 8 9222 3444 **www.dmp.wa.gov.au/GSWApublications**

**Cover photograph:** Glenburgh view of terrane

# Contents



# Appendices



# Figures

## Tables

# Unravelling the upper-amphibolite facies Glenburgh gold deposit, Gascoyne Province — evidence for metamorphosed mineralization

**by**

**LK Roche**

## Abstract

Gold deposits are rare in upper-amphibolite to granulite facies environments. Known examples commonly attract debate about whether they formed at these high temperatures, or instead represent metamorphosed, metasomatic or superimposed (retrograde) mineralization. The one-million ounce Glenburgh gold deposit was formed in the Paleoproterozoic, upper-amphibolite facies Glenburgh Terrane in the southern Gascoyne Province of Western Australia. Gold at the Glenburgh deposit is free and disseminated within quartz–biotite–garnet gneiss, amphibolite and (post-gold) quartz–chlorite veins. Gold lodes are discontinuous and trend east-northeasterly. Lithologies strike east-northeasterly within a tightly folded and steep northerly dipping package. The whole package and gold lodes are offset by the Deadman Fault. No clear association with a specific host lithology has been identified at the Glenburgh deposit, and mineralization does not have a visually distinct proximal alteration assemblage.

Evidence from field mapping, visual and hyperspectral logging of drill samples, thin-section petrography, gold-microstructure analysis and zircon U–Pb geochronology of the Zone 126 and Icon lodes at the Glenburgh deposit demonstrates that this is a metamorphosed gold deposit. Features within the internal structure of gold grains, such as high-purity gold veinlets, incoherent twinning and low silver content, suggest the gold has been through postdepositional processes such as metamorphism and deformation. The presence of rounded sulfide inclusions within almandine, a peak metamorphic mineral, illustrates there was a sulfide phase present prior to the peak of metamorphism. The lack of a definitive alteration assemblage further suggests that the alteration assemblage and mineralization were recrystallized and perhaps remobilized during deformation and metamorphism. Geochronology data based on U–Pb indicates that mineralization must have formed later than c. 2035 Ma — the maximum depositional age of the metasedimentary host rocks — and prior to c. 1991 Ma — the peak of metamorphism during the Glenburgh Orogeny.

An analysis of petrographic and geophysical data suggests that Ca and K abundances increase, and magnetic susceptibility decreases, towards gold mineralization. These potentially constitute ore vectors. Slight variations in host mineralogy, such as an increase in white micas and chlorite at the Icon lode, are also evident along the mineralized trend, perhaps partly reflecting metamorphosed alteration, although a more detailed investigation is required.

**KEYWORDS**: amphibolite facies, geochronology, gold, metamorphism, migmatite

## Introduction

'Orogenic' gold deposits commonly form in greenschist facies terrains, and are rare in high-grade metamorphic rocks (Groves, 1993). This is conventionally attributed to gold mineralization forming from gold complexes transported in hydrothermal fluids that were sourced from the breakdown of chlorite in rocks undergoing moderate-grade (500–550°C) transitional greenschist–amphibolite metamorphism (Tomkins, 2010), which then moved along retrograde metamorphic paths (Goldfarb et al., 2005). However, relationships observed between gold mineralization and associated alteration assemblages in high-grade metamorphic host rocks led some workers to conclude that gold was precipitated during the peak of metamorphism (Chown et al., 1984; Phillips, 1985; Groves et al., 1992; Groves, 1993).

The 'crustal continuum model' was developed based on Archean lode-gold deposits to explain how 'gold only' deposits might form during an orogenic event at the peak to slightly postpeak period of medium- to high-grade metamorphism (Colvine et al., 1984; Groves, 1993; Groves et al., 1998). A combination of fluid inclusion data and mineral equilibria calculations suggest that lode-gold deposits of the continuum model reflect pressure–temperature (P–T) conditions from 180°C at <1 kb to 700°C at about 5 kb (Groves, 1993).

The continuum model has been subsequently challenged by researchers who have more recently re-examined the deposits hosted in high-grade metamorphic rocks previously used to support the model, including type examples such as the Big Bell and Griffins Find deposits (Phillips and Powell, 2009). Knowledge of the physical

behaviour of partially melted metamorphic rocks associated with gold mineralization has also advanced (Tomkins and Mavrogenes, 2002; White and Powell, 2002). Tomkins and Grundy (2009) argue that it is difficult to transmit potentially gold-mineralizing hydrothermal fluids through rocks at temperatures above 600–650°C because the addition of any hydrothermal fluid under these conditions would cause partial melting of the rocks, and consumption of the fluid, thereby inhibiting its transfer as a free phase. Partial melting is indicated by the presence of pegmatite dykes or migmatites in many high-grade metamorphosed gold deposits, including Big Bell, Hemlo, Griffins Find, Challenger and Renco (Tomkins and Mavrogenes, 2002; Tomkins et al., 2004a,b; Phillips and Powell, 2009; Tomkins and Grundy, 2009).

A number of explanations for gold deposits hosted by upper amphibolite- to granulite-facies rocks falls into one of two main categories: formation prior to peak metamorphism (e.g. Hemlo, Challenger, Big Bell and Griffins Find; Tomkins and Mavrogenes, 2002; Tomkins et al., 2004a,b; Phillips and Powell, 2009; Tomkins and Grundy, 2009) or formation during postpeak, retrograde metamorphism (e.g. Renco or Tropicana; Kisters et al., 1998; Doyle et al., 2013, 2014; Blenkinsop and Doyle, 2014; Kolb et al., 2015). Debate persists over whether gold can precipitate at high temperatures and pressures, or if all such deposits represent metamorphosed or retrograde deposits (Groves, 1993; Goldfarb et al., 2005; Tomkins and Grundy, 2009).

In order to establish a relative timing of events in an evolving terrane with progressive metamorphism and deformation, careful petrographic, gold microstructure, and field observations are required. Several methods can be used to determine whether gold mineralization has undergone metamorphism or not. For instance the internal structure of the gold grains, such as the arrangement and size of crystals, and evidence for plastic deformation of the crystal lattice, can help understand their growth history (Nikolaeva et al., 2004). The presence of high-purity gold veinlets between gold grains and incoherent twinning within grains suggest metamorphism and deformation (Nikolaeva et al., 2004). Gold fineness can also be used to understand grain-growth history. Primary hypogene gold commonly contains 5–20% silver content (Hough et al., 2007), which decreases with metamorphism, deformation and contact with aggressive solutions, or any of these separately.

Sulfide minerals are commonly temporally and genetically related to gold mineralization; therefore, determining textures and relative timing of sulfide phases might inform interpretations of gold mineralization, especially when visible gold grains are scarce. Sulfide inclusions within peak-metamorphic minerals indicate a sulfide presence prior to the peak of metamorphism (e.g. sulfides within garnet; Tomkins and Grundy, 2009; Frost et al., 2002; Tomkins et al., 2004a).

## Regional geology and metallogeny

The Glenburgh Terrane forms part of the southern Gascoyne Province of the Capricorn Orogen. The Capricorn Orogen records the two-stage collision of the exotic Glenburgh Terrane with the Archean Pilbara and Yilgarn Cratons to form the West Australian Craton, followed by more than one billion years of intraplate reworking (Occhipinti et al., 2004; Johnson et al., 2010, 2013).

Deep-crustal seismic-reflection surveys have been undertaken across the orogen. It is interpreted from the data that the Glenburgh Terrane forms the basement of the southern half of the Gascoyne Province, and is bounded against the Pilbara and Yilgarn Cratons by suture zones now marked at the surface by the Lyons River and Cardilya Faults, respectively (Fig. 1c,d; Johnson et al., 2011a, 2013). The basement to the northern half of the Gascoyne Province is the Bandee Seismic Province, interpreted as part of the Pilbara Craton (Fig. 1d; Johnson et al., 2011a).

The oldest known rocks in the Glenburgh Terrane belong to the 2555–2430 Ma Halfway Gneiss. These rocks are overlain by the 2240–2145 Ma Moogie Metamorphics and intruded by the 2005–1975 Ma Dalgaringa Supersuite. These are overlain by the 2000–1955 Ma Camel Hills Metamorphics (Occhipinti et al., 2004; Johnson et al., 2011c). The Ashburton (1820–1770 Ma) and Edmund (1680–1465 Ma) Basins overlie the Glenburgh Terrane – Pilbara Craton suture (Fig. 1; Occhipinti et al., 2004; Johnson et al., 2010, 2013).

The collision of the Glenburgh Terrane with the Pilbara Craton must have taken place in the Paleoproterozoic, prior to the formation of the overlying Ashburton and Edmund Basins. The collision may have been contemporaneous with deposition in a foreland basin setting of the 2240–2145 Ma protoliths of the Moogie Metamorphics (Johnson et al., 2011b). This foreland basin is interpreted to have formed in response to uplift of the southern margin of the Pilbara Craton during collision with the Glenburgh Terrane (Occhipinti et al., 2004; Martin and Morris, 2010; Johnson et al., 2010, 2011a). The only known tectono-thermal event of appropriate age in the region is the 2215–2145 Ma Ophthalmian Orogeny (Occhipinti et al., 2004; Rasmussen et al., 2005; Johnson et al., 2010).

Collision of the Glenburgh Terrane with the Yilgarn Craton is inferred to have happened subsequent to the Glenburgh Terrane – Pilbara Craton amalgamation, along a northerly or northwesterly directed subduction zone (Occhipinti et al., 2004; Sheppard et al., 2004; Cawood and Tyler, 2004; Johnson, 2013). The event resulted in the development of the Dalgaringa Arc (magmatic arc growth, $D_{1g}$). Associated arc-magmatism was marked by voluminous intrusions of calc-alkaline tonalite–trondhjemite–granodiorite (TTG) of the 2005–1975 Ma Dalgaringa Supersuite (Fig. 2; Sheppard et al., 2004). Magma emplacement was accompanied by high-grade metamorphism at 800–1000°C and 7–10 kbar (Johnson et al., 2010, 2011b), which peaked at c. 1997 Ma (GSWA 185942; Wingate et al., 2010; Johnson et al., 2010, 2011b).

Collision of the combined Glenburgh Terrane – Pilbara Craton with the Yilgarn Craton took place during the 1965–1950 Ma $D_{2g}$ phase of the Glenburgh Orogeny (Cawood and Tyler, 2004; Occhipinti et al., 2004;

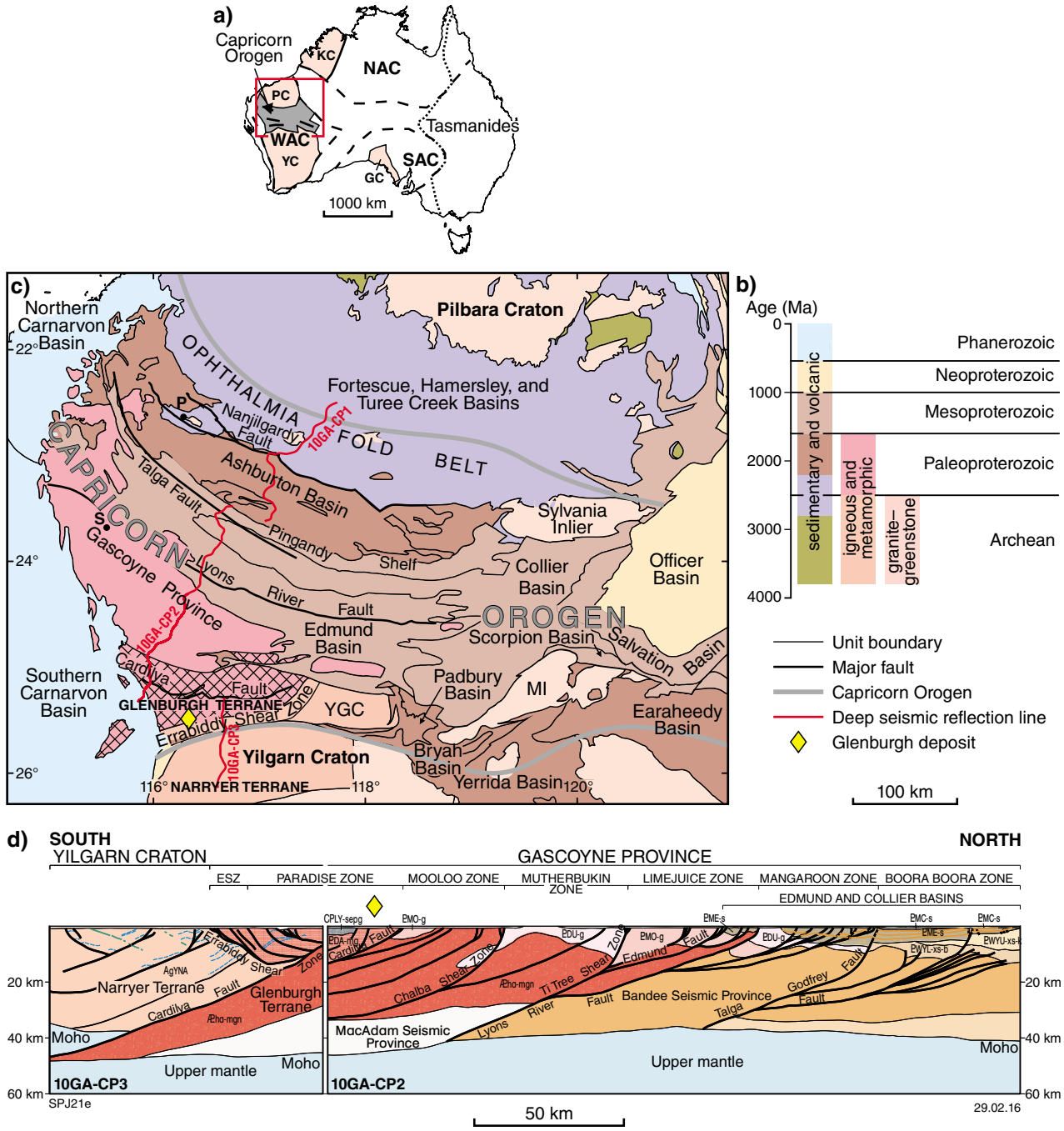


**Figure 1.** **Geology of the Capricorn Orogen: a) location of the Capricorn Orogen within the main crustal elements of Australia. Paleoproterozoic crustal elements (KC – Kimberly Craton; NAC – North Australian Craton; SAC – South Australian Craton; WAC – West Australian Craton) and Archean cratons (YC – Yilgarn Craton; PC – Pilbara Craton; GC – Gawler Craton); b) ages of elements of the Capricorn Orogen and adjacent terranes labelled with dominant rock type; c) geology of the Capricorn Orogen and surrounding cratons and basins. Other abbreviations: MI – Marymia Inlier; YGC – Yarlarweelor Gneiss Complex; d) geological interpretation of the Glenburgh Terrane from Johnson et al. (2011) based on two seismic survey lines 10GA-CP2 and 10GA-CP3. Figures a–c) from Johnson et al. (2013), locations shown in 1c.**

Johnson et al., 2010, 2011b). Assembly of the West Australian Craton was completed before granitic stocks and dykes of the 1965–1945 Ma Bertibubba Supersuite were emplaced into the Errabiddy Shear Zone, which cuts across the northern margin of the Yilgarn block and southern Glenburgh Terrane (Occhipinti et al., 2004; Johnson, 2013).

More than one billion years of intracontinental reworking of the Capricorn Orogen and marginal Pilbara and Yilgarn Cratons followed assembly of the West Australian Craton. This included the 1820–1770 Ma Capricorn Orogeny, the 1680–1620 Ma Mangaroon Orogeny, the 1321–1171 Ma Mutherbukin Tectonic Event, the 1026–954 Ma Edmundian Orogeny and the c. 570 Ma Mulka Tectonic Event (Sheppard et al., 2010). This also included deposition into sedimentary basins of the protoliths of the 1840–1810 Ma Leake Spring Metamorphics, 2008–1786 Ma Wyloo Group, 1760–1685 Ma Pooranoo Metamorphics, 1680–1455 Ma Edmund and Scorpion Groups and 1171–1070 Ma Collier and Salvation Groups (Johnson, 2013).

The Capricorn Orogen appears to be much less well-endowed in metalliferous mineralization than the Yilgarn Craton. Some orogenic gold has been mined in the central to eastern part of the Capricorn Orogen, from reworked Archean basement at Peak Hill and from Paleoproterozoic greenschist facies metasiliciclastic rocks of the Peak Hill Schist, and the Bryah and Padbury Basins (Pirajno, 2004). Copper–gold ore is presently being mined from mafic rocks of the Bryah Basin at the world-class Paleoproterozoic De Grussa volcanic-hosted massive sulfide (VHMS) deposit (Hawke et al., 2015). Other notable mineral deposits in the Capricorn Orogen include gold at Mount Olympus, in the Ashburton Basin, Pb–Cu–Zn at Abra (Pirajno et al., 2010), and rare earth elements at Yangibana (Pearson et al., 1996; Pirajno and Gonzalez-Alvarez, 2014). The De Grussa discovery was only made in 2009, and the apparent poor endowment may be a function of less exploration of the Capricorn Orogen compared with the Yilgarn Craton. Interpretation of crustal-scale structures based on new deep-crustal seismic-reflection survey data highlights the most prospective exploration targeting areas, particularly as all of the aforementioned deposits are spatially associated with major crustal-suture zones and lithospheric-scale faults.

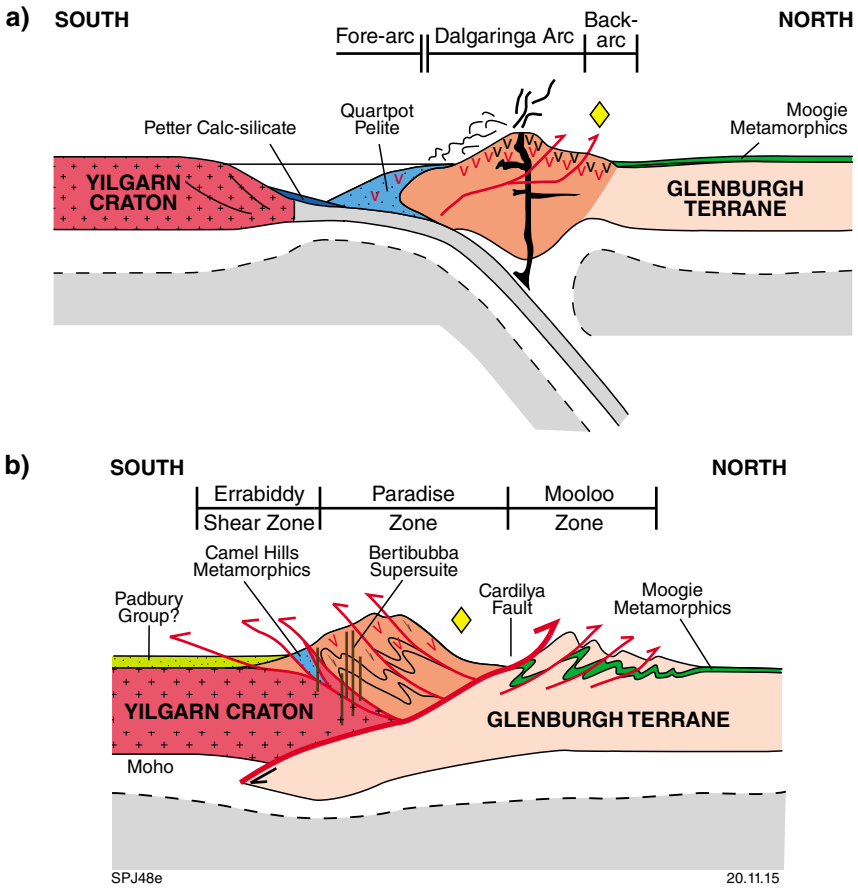


**Figure 2.** **Schematic cross-section showing development of the Glenburgh Orogeny (from Johnson, 2013) and possible tectonic setting of the Glenburgh Orogeny during: a) the Dalgaringa Arc formation; b) subsequent collision of the Glenburgh Terrane with the Yilgarn Craton. Approximate location of the Glenburgh deposit is marked by the yellow diamond.**

## Local geology

Gold mineralization at the Glenburgh deposit (presently owned and operated by Gascoyne Resources Limited) is hosted in Paleoproterozoic upper-amphibolite to granulite facies siliciclastic rocks of the Glenburgh Terrane, in the southern Gascoyne Province of Western Australia (Fig. 3). Gold was first discovered at the Glenburgh deposit in 1994 by Helix Resources during follow-up drilling of soil geochemical anomalies (Overton, 2000). The defined resource currently stands at approximately one million ounces (Gascoyne Resources, 2014). The gold is known to be free milling, and is present in discontinuous, east-northeasterly trending lodes in quartz–feldspar–biotite–garnet gneisses (Fig. 3). Limited knowledge exists regarding the age, style and setting of gold mineralization, and whether there are specific host-rock controls or recognizable alteration associated with the gold.

The Glenburgh deposit is an ideal candidate for further testing of the metallogenic models for orogenic gold deposits in high-grade metamorphic terrains. The goals of this study were to:

- determine the geological setting and timing of the gold within the known tectonic evolution of the Glenburgh Terrane
- determine if there is a recognizable alteration signature associated with gold mineralization
- use this knowledge to better understand the gold prospectivity of the region, and identify potential vectors to gold mineralization within it.

# Methods

The study focused on the small, moderate-grade (2.5 g/t average) Zone 126 lode of the Glenburgh gold deposit and, to a lesser extent, on the larger, slightly lower grade (1.3 g/t average) Icon lode (Figs 3,4). These two lodes were selected in order to compare mineralization at opposite ends of the roughly linear Glenburgh-deposit trend, and due to the higher potential of encountering visible gold.

A program involving field mapping, hyperspectral and visual drill-sample logging, analysis of the internal structure of gold grains and interpretation of recently acquired SHRIMP U–Pb geochronology data was undertaken. Field mapping was completed with the aid of remote sensing and geophysical datasets in order to place mineralization into a regional geology context. Visual logging of drillcore and drill chips was done with the support of hyperspectral data to determine the paragenetic relationship between gold mineralization and host lithologies, and to seek any possible cryptic alteration signatures.

Results from petrography, scanning electron microscopy (SEM) and X-ray diffractometry (XRD) were used to validate these observations. The growth history of individual gold grains was interpreted from their internal structure, which can reveal information on the deformation and metamorphic history of the gold. The internal structure was revealed by acid etching and laser ablation – inductively coupled plasma – mass spectrometry (LA–ICP–MS). Maximum and minimum ages for gold mineralization were constrained by SHRIMP U–Pb dating of detrital and metamorphic zircons in the pelitic migmatite host rocks.

## Field mapping

Geological mapping was conducted over an area of about two by three kilometres extending from Paradise Well (Zone 50, MGA 413799E 7191868N), where the structural and metamorphic history is well defined (Johnson et al., 2010, 2011b), northward into the less well-documented rocks containing the Glenburgh Zone 126 lode, in order to constrain the metamorphic, structural and stratigraphic relationships (Fig. 3). Outcrop in the region is discontinuous, and field mapping was supplemented by available aeromagnetic, radiometric (gamma-ray spectrometric) and Landsat TM data (bands 754 and 741) to interpret structural and lithotectonic-unit trends. The aeromagnetic image used for interpretation comprised the reduced to pole total magnetic intensity (TMI) data and a first vertical derivative of the reduced to pole TMI data (1VD-TMI).

## Hyperspectral logging of drillhole samples

Gascoyne Resources provided drill samples and gold-assay data for eight drillholes intersecting the Glenburgh Zone 126 lode and Icon lode (Table 1, Figs 4,5). Drill samples comprised orientated diamond core and pre-collar rotary air blast (RAB) rock chips, or just rock chips in the case of the reverse circulation (RC) drillholes. Material from each hole was lithologically and structurally logged, then scanned using the Geological Survey of Western Australia's (GSWA) HyLogger for drillcore or HyChips for drill chips using the methodology of Hancock and Huntington (2010). Reflectance spectra for diamond core were collected over the visible and near infrared (VNIR, 400–1000 nm), short-wave infrared (SWIR, 1000–2500 nm) and thermal infrared (TIR, 6000–14 500 nm) wavelength ranges. High-resolution (0.1 mm pixel) digital photographs of core were obtained concurrently. Drill chips were scanned only over the VNIR and SWIR ranges; therefore, mineralogical logging of drillhole GBD021 was limited to white micas, amphiboles and dark micas (feldspars, garnets and other anhydrous silicates require TIR for accurate identification). Spectra were interpreted using The Spectral Geologist (TSG) software. Hyperspectral logging assisted with improved identification of host rock and alteration mineralogy, including chemical and physical characteristics, and with defining lithostratigraphic units and vectors to mineralization.

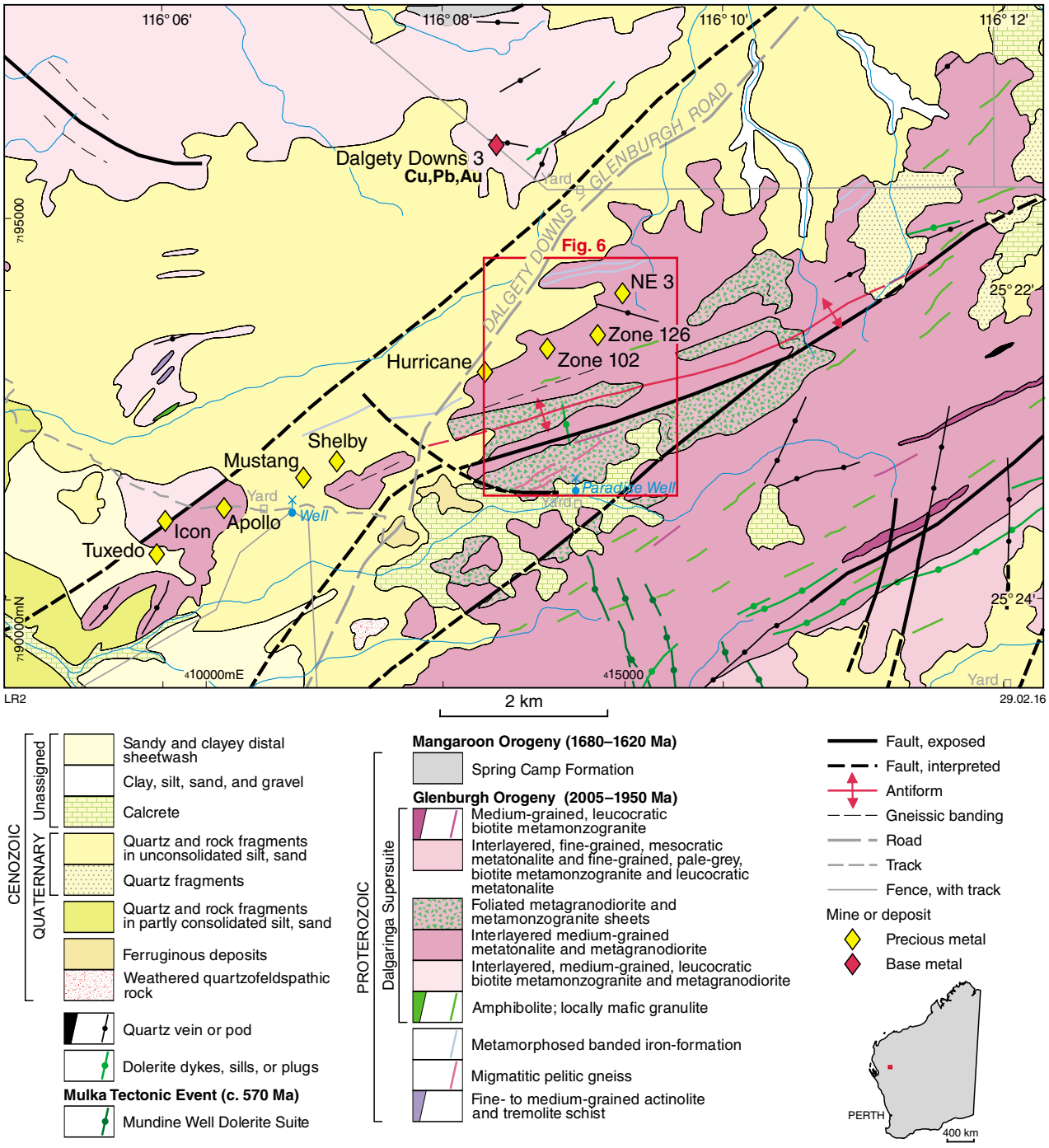


**Figure 3. Part of GLENBURGH, WA Sheet 2147 (2nd edition) 1:100 000 Geological Series map showing location of the Glenburgh project and field mapping area outlined in red. Modified after Occhipiniti et al. (2011)**

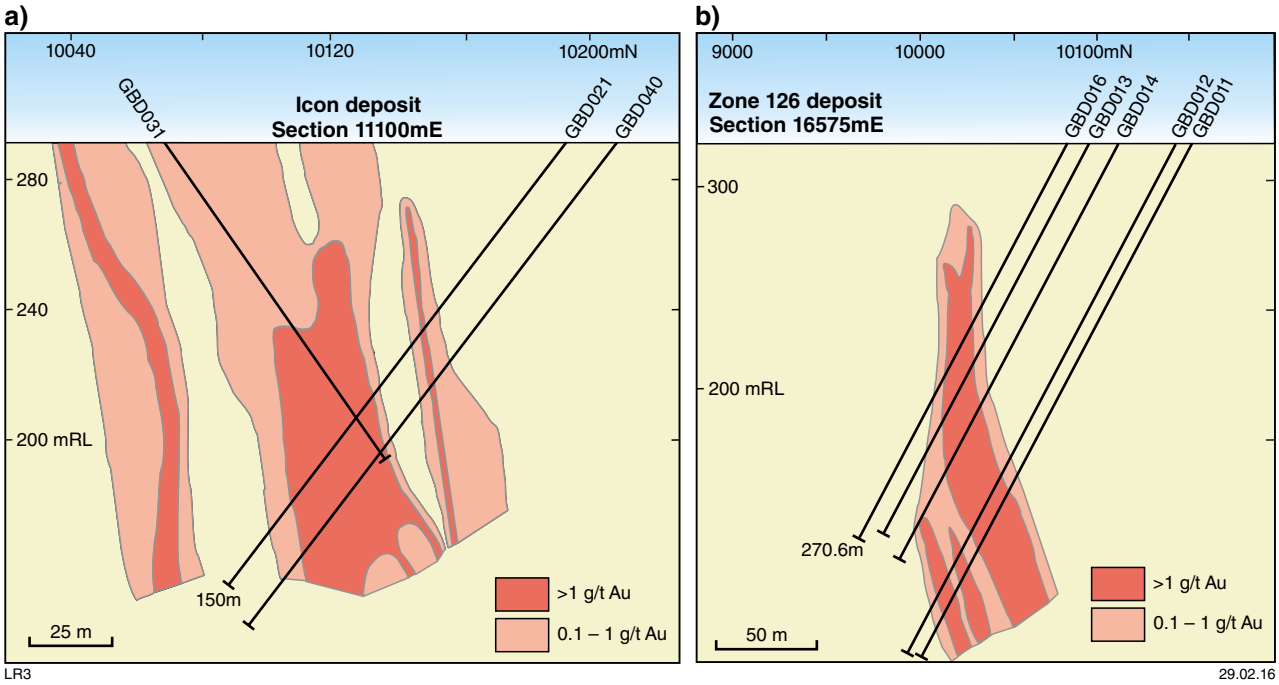


**Figure 4. Cross-sections of Icon and lodes Zone 126: a) Icon; b) Zone 126**

**Table 1. Details of drill samples analysed**

| *Drillhole* | *MGA coordinates (Zone 50)* | *Type* | *Lode intersected* | *RAB pre-collar depth (m)* | *Total depth (m)* |
|---|---|---|---|---|---|
| GBD011 | 414566mE, 7193743mN | Diamond | Zone 126 | 177 | 366.5 |
| GBD012 | 414583mE, 7193749mN | Diamond | Zone 126 | 165 | 330.95 |
| GBD013 | 414646mE, 7193731mN | Diamond | Zone 126 | 177 | 249.65 |
| GBD014 | 414623mE, 7193729mN | Diamond | Zone 126 | 171 | 270.8 |
| GBD016 | 414562mE, 7193675mN | Diamond | Zone 126 | 177 | 228.5 |
| GBD021 | 409466mE, 7191463mN | Rock chips | Icon | 177 | 234.7 |
| GBD031 | 409504mE, 7191399mN | Diamond | Icon | – | 130 |
| GBD040 | 409527mE, 7191561mN | Diamond | Icon | 171 | 358.05 |

# Petrography

Eighteen outcrop and 24 drillcore samples were collected. Thin-section descriptions and location details are provided in Appendix 1. A 30 µm thick, polished thin section was made from each sample for optical identification of the mineral assemblages in each lithological unit and determination of the textural and temporal relationship between gold, sulfides and the host rocks. Several thin sections were further analysed for semiquantitative mineral identification and determination of the silver content of gold grains (silver detection limit of 0.5%), using the Phillips XL40 Controlled Pressure SEM at Commonwealth Scientific and Industrial Research Organisation's (CSIRO) Australian Resources Research Centre, Kensington, with the assistance of Michael Verrell. It was operated in controlled-pressure mode with a chamber pressure between 0.1 and 0.5 mbar to prevent charge buildup on uncoated samples, an accelerating voltage of 30 kV and a beam current of between 1 and 10 nA. Images were collected using a backscattered electron (BSE) detector. Several thin sections were selected for additional SEM and XRD analyses to further define the mineralogy.

# X-ray diffractometry

Independent mineral identification was performed on five representative drillcore samples (leucosome: GSWA 214901, 214910; melanosome: GSWA 214917; amphibolite: GSWA 214906, 214913) using an automated Phillips X-ray diffractometer at the Rosny laboratories of Mineral Resources Tasmania (Appendix 2; Bottrill and Woolley, 2014). Instrument specifications include: PW1729 generator, PW1050 goniometer and PW1710 microprocessor with nickel-filtered copper radiation at 40 kV/30 mA, a graphite monochromator (PW1752), sample spinner and a proportional detector (sealed, gas filled, PW1711). The PW1710 system is driven

by CSIRO's XRD software: 'PW 1710 for Windows' and 'XPLOT for Windows'. Mineral identification and quantification were completed manually by Ralph Bottrill, Mineral Resources Tasmania, using a series of prepared standards for the common minerals to enable some semiquantitative analysis.

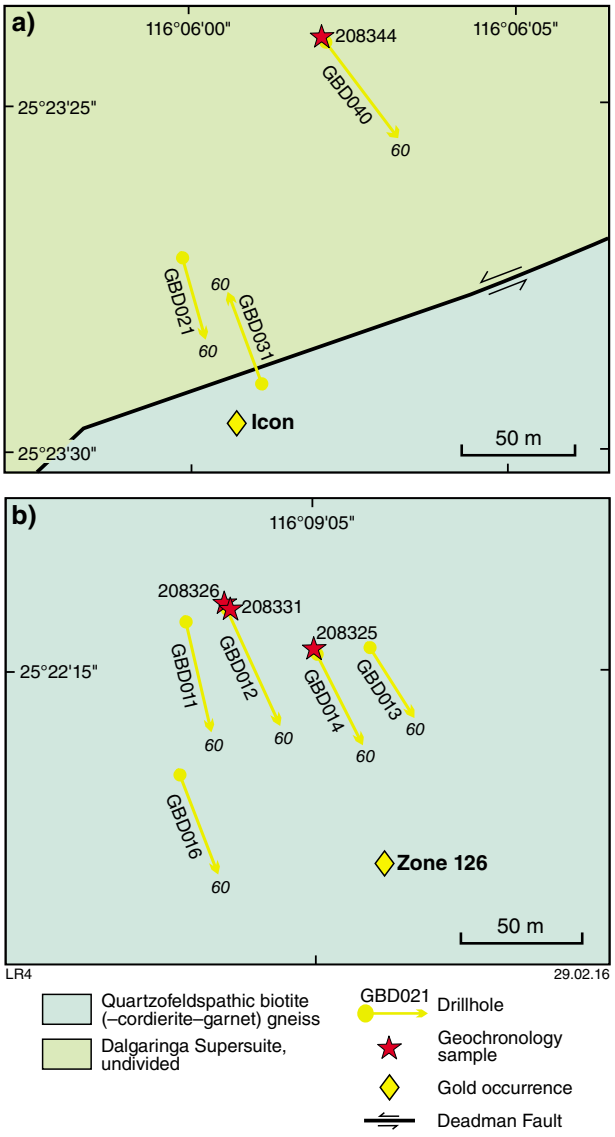


**Figure 5. Plan of drillholes and geochronology locations for Icon and Zone 126 lodes on interpreted bedrock geology map**

## Gold etching

The internal microstructure of one polished gold grain liberated from Glenburgh core (GBD011 at 333.9 m, GSWA 214909) was revealed by leaching in aqua regia for three minutes, then imaging the grain surface using the SEM (under the same conditions described above). The grain was approximately 100 µm in size and other mounted grains were too small to resolve any internal features.

## LA–ICP–MS

The trace-element signatures of Glenburgh gold grains and associated minerals from sample GSWA 214909 (drillhole GBD011) were determined using LA–ICP–MS. This process enables the detection of isomorphic impurities in gold (e.g. Cu, Te, Se, Hg, platinum group elements) and inclusions from surrounding host rocks (e.g. lithophile elements). Thus, trace-element signatures can reveal information on other elements associated with the gold-mineralizing fluid, host rock's mineralogical relationship with gold, and fluid source.

The same gold grains extracted from sample GSWA 214909 that were mounted in epoxy and etched were re-polished and used for LA–ICP–MS analysis. Analyses were conducted by Cameron Scadding (TSW Analytical), using the Resonetics RESOlution M-50A-LR instrument, incorporating a Compex 102 excimer laser, and an Agilent 7700s inductively coupled plasma mass spectrometer. Instrumental settings were optimized using National Institute of Standards and Technology (NIST) glass standards NIST 610 and NIST 612. Samples were ablated for 30 seconds, with a laser energy of 100 mJ, fluence of 4 j/cm$^2$, and a spot size of 33 µm. Only one spot analysis could be made for six of the gold grains (analyses 6, 7, 14, 15, 18, 20) because their small size and thickness lead to their rapid consumption. Analyses were made of the mineral host (tschermakite and ilmenite) and the epoxy resin (without gold) for comparison. The resulting data for 67 elements are reported in Table 2. All data are reported in counts per second (cps) rather than in terms of absolute concentrations (e.g. ppb), and so all element variations are discussed in relative terms.

## Geochronology

Possible maximum and minimum ages for gold mineralization were constrained by U–Pb dating of detrital and metamorphic zircons from four pelitic migmatite samples taken from drillcore (Table 3, Fig. 5). Dates were obtained via secondary-ion mass spectrometry (SIMS) using the sensitive high-resolution ion microprobe (SHRIMP) facility at the John de Laeter Centre of Mass Spectrometry at Curtin University, Perth, Western Australia. Three samples are from the Zone 126 lode (GSWA 208325, 208326, 208331) and one is from the Icon lode (GSWA 208344). Analytical methods for SHRIMP U–Pb zircon geochronology are described in detail by Wingate and Kirkland (2014). Specific details for each sample used in this study, including U–Pb analytical data, are documented by Wingate et al. (2015a,b,c,d).

**Table 2. LA–ICP–MS data for gold from Glenburgh (counts per second)**

| | *1*<br>*Au* | *2*<br>*Au* | *3*<br>*Au* | *6*<br>*Au+HR* | *7*<br>*Au+HR* | *10*<br>*Au+HR* | *11*<br>*Au+HR* | *13*<br>*Au+HR* | *14*<br>*Au+HR* | *15*<br>*Au+HR* | *18*<br>*Au+HR* | *19*<br>*HR* | *20*<br>*Au+HR* | *3*<br>*Resin* | *4*<br>*Resin* | *8*<br>*HR* | *9*<br>*HR* | *21*<br>*HR* |
|---|---|---|---|---|---|---|---|---|---|---|---|---|---|---|---|---|---|---|
| Si | 290 000 | 120 000 | 540 000 | 1 040 000 | 500 000 | 3 600 000 | 3 140 000 | 7 730 000 | 8 100 000 | 7 130 000 | 1 780 000 | 6 590 000 | 2 530 000 | 11 900 000 | 540 000 | 9 820 000 | 8 620 000 | 6 040 000 |
| Li | 0 | 0 | 0 | 10 | 92 | 500 | 380 | 580 | 620 | 240 | 123 | 12 | 390 | 0 | 0 | 580 | 39 | 360 |
| Be | 0 | 0 | 0 | 0 | 0 | 0 | 0 | 0 | 0 | 0 | 0 | 0 | 0 | 0 | 0 | 0 | 0 | 0 |
| B | 0 | 93 | 0 | 20 | 68 | 0 | 38 | 41 | 15 | 0 | 0 | 0 | 33 | 0 | 50 | 145 | 0 | 120 |
| Na | 0 | 0 | 0 | 15 000 | 14 600 | 124 000 | 86 000 | 833 000 | 218 000 | 890 000 | 33 000 | 750 000 | 150 000 | 0 | 0 | 424 000 | 1 058 000 | 267 000 |
| Mg | 110 | 40 | 120 | 18 500 | 9 900 | 112 000 | 110 000 | 346 000 | 150 000 | 352 000 | 44 000 | 325 000 | 113 000 | 0 | 0 | 138 000 | 358 000 | 267 000 |
| Al | 710 | 280 | 540 | 230 000 | 350 000 | 3 020 000 | 3 530 000 | 6 750 000 | 4 060 000 | 6 400 000 | 590 000 | 4 520 000 | 2 680 000 | 620 | 170 | 7 110 000 | 5 970 000 | 7 060 000 |
| P | 1 100 | 600 | 700 | 1 080 | 470 | 0 | 350 | 0 | 80 | 270 | 480 | 700 | 660 | 1 400 | 120 | 480 | 0 | 0 |
| K | 1 800 | 1 000 | 0 | 130 000 | 101 000 | 1 600 000 | 2 550 000 | 1 270 000 | 1 700 000 | 620 000 | 113 000 | 328 000 | 1 200 000 | 0 | 0 | 4 570 000 | 295 000 | 3 850 000 |
| Ca | 600 | 0 | 1 400 | 14 300 | 4 200 | 34 000 | 52 000 | 245 000 | 69 000 | 292 000 | 14 000 | 229 000 | 45 000 | 220 | 0 | 38 400 | 298 000 | 49 000 |
| Sc | 330 | 70 | 260 | 940 | 730 | 4 730 | 8 700 | 12 320 | 6 860 | 11 200 | 1 200 | 8 570 | 5 400 | 250 | 230 | 8 960 | 9 600 | 8 400 |
| Ti | 0 | 0 | 40 | 880 | 820 | 12 100 | 14 300 | 28 100 | 18 500 | 24 000 | 1 500 | 19 100 | 11 000 | 64 | 0 | 29 900 | 24 400 | 19 200 |
| Cr | 90 | 190 | 132 | 90 | 240 | 840 | 890 | 1 370 | 870 | 1 150 | 520 | 1 070 | 850 | 41 | 21 | 1 600 | 1 600 | 1 120 |
| Mn | 4 200 | 0 | 6 000 | 17 400 | 11 900 | 56 000 | 49 000 | 311 000 | 96 000 | 356 000 | 13 000 | 334 000 | 71 000 | 8 900 | 6 200 | 66 800 | 357 000 | 75 000 |
| Fe | 150 | 0 | 0 | 19 300 | 34 000 | 232 000 | 245 000 | 637 000 | 318 000 | 651 000 | 109 000 | 511 000 | 218 000 | 0 | 0 | 261 000 | 571 000 | 458 000 |
| Co | 80 | 0 | 20 | 190 | 360 | 2 640 | 5 900 | 8 100 | 4 050 | 8 300 | 580 | 7 160 | 3 300 | 0 | 30 | 4 210 | 9 270 | 9 100 |
| Ni | 0 | 29 | 20 | 50 | 100 | 780 | 1 700 | 1 880 | 1 190 | 1 950 | 290 | 2 120 | 1 080 | 0 | 10 | 1 780 | 1 840 | 3 670 |
| Cu | 57 000 | 40 000 | 65 800 | 29 000 | 11 500 | 19 600 | 110 000 | 3 600 | 12 700 | 5 900 | 24 000 | 550 | 17 200 | 0 | 14 | 600 | 13 | 320 |
| Zn | 57 | 89 | 56 | 250 | 600 | 3 170 | 12 600 | 9 730 | 4 430 | 9 900 | 740 | 8 600 | 3 300 | 58 | 39 | 1 880 | 8 400 | 4 800 |
| Ga | 0 | 0 | 39 | 108 | 510 | 1 580 | 2 110 | 4 350 | 2 390 | 3 920 | 310 | 3 630 | 1 650 | 0 | 0 | 4 380 | 3 650 | 4 530 |
| Ge | 0 | 0 | 170 | 0 | 190 | 90 | 90 | 340 | 210 | 380 | 80 | 290 | 110 | 20 | 110 | 220 | 430 | 130 |
| As | 0 | 0 | 50 | 66 | 40 | 98 | 118 | 156 | 170 | 240 | 130 | 850 | 130 | 0 | 0 | 119 | 94 | 75 |
| Se | 70 | 290 | 0 | 0 | 0 | 60 | 0 | 0 | 140 | 30 | 0 | 0 | 70 | 0 | 150 | 210 | 50 | 0 |
| Rb | 0 | 62 | 31 | 520 | 520 | 8 480 | 14 300 | 5 100 | 7 420 | 2 700 | 450 | 700 | 6 600 | 0 | 0 | 17 100 | 250 | 17 500 |
| Sr | 0 | 0 | 0 | 125 | 1 420 | 700 | 1 350 | 2 290 | 1 130 | 1 910 | 89 | 1 710 | 650 | 10 | 0 | 5 960 | 2 040 | 1 130 |
| Y | 0 | 14 | 0 | 280 | 3 500 | 3 010 | 4 300 | 12 120 | 4 900 | 13 900 | 1 300 | 8 100 | 2 700 | 0 | 0 | 7 600 | 13 500 | 3 600 |
| Zr | 640 | 470 | 720 | 80 | 300 | 830 | 950 | 880 | 1 500 | 960 | 1 500 | 1 400 | 2 000 | 20 | 0 | 830 | 590 | 910 |
| Mo | 0 | 0 | 0 | 0 | 0 | 0 | 0 | 0 | 0 | 0 | 0 | 0 | 0 | 0 | 0 | 0 | 10 | 0 |
| Ru | 0 | 0 | 0 | 0 | 0 | 0 | 0 | 0 | 0 | 0 | 0 | 0 | 0 | 0 | 0 | 0 | 0 | 0 |
| Rh | 0 | 0 | 0 | 0 | 0 | 0 | 0 | 0 | 0 | 0 | 0 | 0 | 0 | 0 | 0 | 0 | 0 | 0 |
| Pd | 3 000 | 3 100 | 3 400 | 3 380 | 1 880 | 1 700 | 3 700 | 370 | 1 870 | 510 | 1 770 | 0 | 960 | 0 | 0 | 0 | 0 | 0 |
| Ag | 6 900 000 | 6 200 000 | 11 300 000 | 6 000 000 | 2 900 000 | 5 300 000 | 9 100 000 | 1 130 000 | 3 400 000 | 1 400 000 | 3 900 000 | 10 | 5 500 000 | 0 | 0 | 60 | 0 | 60 |
| Cd | 20 | 0 | 20 | 0 | 0 | 0 | 36 | 69 | 0 | 15 | 0 | 0 | 0 | 0 | 0 | 0 | 0 | 0 |
| In | 0 | 75 | 20 | 0 | 0 | 17 | 160 | 117 | 100 | 92 | 150 | 127 | 50 | 0 | 0 | 91 | 60 | 110 |
| Sn | 20 | 0 | 0 | 17 | 92 | 217 | 470 | 710 | 280 | 577 | 133 | 370 | 310 | 0 | 0 | 710 | 580 | 710 |
| Sb | 46 | 0 | 0 | 82 | 111 | 60 | 260 | 141 | 94 | 239 | 140 | 18 | 85 | 0 | 42 | 39 | 0 | 110 |
| Te | 36 | 57 | 13 | 410 | 700 | 1 870 | 7 400 | 2 150 | 650 | 300 | 950 | 19 | 111 | 28 | 0 | 0 | 0 | 0 |
| Cs | 0 | 0 | 36 | 25 | 0 | 140 | 153 | 190 | 122 | 94 | 38 | 29 | 150 | 11 | 0 | 450 | 0 | 670 |

| | *1*<br>*Au* | *2*<br>*Au* | *3*<br>*Au* | *6*<br>*Au+HR* | *7*<br>*Au+HR* | *10*<br>*Au+HR* | *11*<br>*Au+HR* | *13*<br>*Au+HR* | *14*<br>*Au+HR* | *15*<br>*Au+HR* | *18*<br>*Au+HR* | *19*<br>*HR* | *20*<br>*Au+HR* | *3*<br>*Resin* | *4*<br>*Resin* | *8*<br>*HR* | *9*<br>*HR* | *21*<br>*HR* |
|---|---|---|---|---|---|---|---|---|---|---|---|---|---|---|---|---|---|---|
| Ba | 0 | 0 | 0 | 18 | 77 | 1 460 | 1 760 | 1 160 | 1 510 | 520 | 11 | 190 | 840 | 0 | 0 | 870 | 400 | 482 |
| La | 0 | 0 | 0 | 0 | 13 300 | 50 | 700 | 100 | 143 | 193 | 50 | 40 | 62 | 0 | 0 | 1 250 | 20 | 190 |
| Ce | 0 | 0 | 0 | 25 | 42 000 | 280 | 1 530 | 920 | 380 | 710 | 33 | 420 | 340 | 0 | 0 | 4 900 | 470 | 740 |
| Pr | 0 | 0 | 0 | 0 | 7 300 | 42 | 227 | 300 | 164 | 115 | 0 | 127 | 108 | 0 | 0 | 740 | 160 | 140 |
| Nd | 0 | 0 | 0 | 0 | 5 200 | 46 | 210 | 390 | 200 | 380 | 0 | 60 | 77 | 0 | 0 | 570 | 430 | 270 |
| Sm | 420 | 300 | 280 | 280 | 960 | 250 | 530 | 230 | 169 | 340 | 178 | 164 | 320 | 0 | 0 | 127 | 330 | 20 |
| Eu | 0 | 0 | 0 | 0 | 500 | 33 | 64 | 277 | 31 | 240 | 0 | 210 | 58 | 0 | 0 | 220 | 280 | 30 |
| Gd | 0 | 0 | 0 | 0 | 380 | 54 | 133 | 369 | 150 | 200 | 0 | 173 | 46 | 0 | 0 | 145 | 330 | 145 |
| Tb | 0 | 0 | 0 | 0 | 340 | 77 | 180 | 410 | 190 | 350 | 0 | 140 | 85 | 0 | 0 | 230 | 410 | 40 |
| Dy | 0 | 0 | 0 | 0 | 250 | 175 | 210 | 615 | 290 | 590 | 0 | 520 | 167 | 0 | 0 | 340 | 780 | 150 |
| Ho | 0 | 0 | 0 | 0 | 180 | 123 | 130 | 510 | 162 | 590 | 20 | 250 | 64 | 0 | 0 | 420 | 870 | 100 |
| Er | 0 | 0 | 0 | 23 | 86 | 92 | 145 | 490 | 169 | 610 | 11 | 330 | 83 | 0 | 0 | 460 | 540 | 160 |
| Tm | 0 | 0 | 0 | 0 | 31 | 31 | 125 | 185 | 38 | 250 | 0 | 130 | 42 | 0 | 0 | 90 | 230 | 80 |
| Yb | 0 | 0 | 0 | 0 | 17 | 117 | 45 | 400 | 115 | 370 | 22 | 220 | 100 | 0 | 0 | 270 | 430 | 80 |
| Lu | 0 | 0 | 0 | 0 | 92 | 77 | 75 | 310 | 154 | 157 | 0 | 164 | 17 | 0 | 0 | 127 | 182 | 60 |
| Hf | 0 | 0 | 0 | 0 | 0 | 0 | 133 | 50 | 23 | 69 | 20 | 30 | 67 | 0 | 0 | 45 | 55 | 0 |
| Ta | 0 | 0 | 0 | 0 | 0 | 0 | 0 | 0 | 38 | 0 | 0 | 64 | 0 | 0 | 0 | 27 | 0 | 20 |
| W | 180 | 100 | 120 | 17 | 140 | 240 | 300 | 125 | 540 | 62 | 3 200 | 1 310 | 360 | 20 | 0 | 410 | 0 | 250 |
| Re | 0 | 0 | 0 | 0 | 0 | 0 | 0 | 0 | 0 | 0 | 0 | 0 | 0 | 0 | 0 | 0 | 0 | 0 |
| Os | 0 | 0 | 0 | 0 | 0 | 0 | 0 | 0 | 0 | 0 | 0 | 0 | 0 | 0 | 0 | 0 | 0 | 0 |
| Ir | 0 | 0 | 0 | 0 | 0 | 0 | 0 | 0 | 0 | 0 | 0 | 0 | 0 | 0 | 0 | 0 | 0 | 0 |
| Pt | 0 | 0 | 40 | 0 | 15 | 0 | 18 | 0 | 31 | 31 | 33 | 100 | 17 | 0 | 0 | 0 | 0 | 0 |
| Au | 204 000 000 | 176 000 000 | 250 000 000 | 178 000 000 | 720 000 000 | 153 000 000 | 242 000 000 | 24 000 000 | 78 000 000 | 29 000 000 | 97 000 000 | 240 | 133 000 000 | 50 | 1 230 | 2 900 | 0 | 860 |
| Hg | 65 800 | 51 000 | 59 000 | 52 100 | 22 300 | 39 000 | 56 000 | 3 500 | 27 000 | 10 300 | 36 000 | 230 | 33 000 | 0 | 320 | 100 | 0 | 0 |
| Tl | 0 | 0 | 0 | 0 | 0 | 67 | 225 | 85 | 79 | 50 | 0 | 27 | 115 | 0 | 0 | 173 | 0 | 155 |
| Pb | 20 | 62 | 60 | 75 | 360 | 710 | 2 050 | 840 | 440 | 760 | 300 | 450 | 250 | 50 | 0 | 1 160 | 650 | 330 |
| Bi | 20 | 0 | 20 | 6 300 | 7 800 | 10 300 | 52 000 | 6 200 | 3 640 | 2 160 | 14 800 | 20 | 1 310 | 0 | 0 | 320 | 0 | 90 |
| Th | 40 | 0 | 0 | 0 | 2 300 | 0 | 0 | 0 | 0 | 0 | 0 | 0 | 0 | 0 | 0 | 60 | 0 | 0 |
| U | 0 | 0 | 0 | 0 | 650 | 0 | 0 | 46 | 0 | 0 | 0 | 36 | 0 | 0 | 0 | 120 | 0 | 10 |

**NOTES**: HR — host rock (tschermakite and ilmenite) Resin — epoxy resin

**Table 3. Samples collected for U–Pb geochronology**

| *Sample ID* | *Drillhole* | *MGA coordinates (Zone 50)* | *Sample depth interval* | *Lithology* |
|---|---|---|---|---|
| 208325 | GBD014 | 414623mE, 7193729mN | 250.60 – 250.90 m | Fine-grained, biotite-rich pelitic migmatite |
| 208326 | GBD012 | 414583mE, 7193749mN | 164.75 – 164.90 m | Garnet-rich biotite pelitic migmatite with <10% leucosome-restite? |
| 208331 | GBD012 | 414583mE, 7193749mN | 287.10 – 287.40 m | Biotite-rich, garnet-free pelitic migmatite with 20–30% leucosome |
| 208344 | GBD040 | 409527mE, 7191561mN | 294.10 – 294.40 m | Pelitic migmatite (garnet–biotite–chlorite rich) and leucosomes |

# Results

## Field mapping

### Host rocks

Rock units in the study area include: quartzofeldspathic biotite–cordierite–sillimanite–spinel(–garnet) gneiss with inclusions of minor mafic granulite, mafic schist and pelite; psammite; quartzofeldspathic biotite(–cordierite–garnet) gneiss, which includes pelite lenses less than one-metre thick; metapegmatite; metagranite; amphibolite; ferruginous metasandstone and quartzite (Fig. 6). The quartzofeldspathic and psammitic gneisses, including those hosting the Glenburgh deposit, are interpreted to have a sedimentary origin.

Most units are interleaved on the decimetre scale, steeply (~80–85°) north- or south-dipping, predominantly east-northeasterly trending, discontinuous lenses and boudins within the psammitic and quartzofeldspathic gneisses (Fig. 7a). A well-developed east-northeasterly trending gneissosity, defined by millimetre- to centimetre-scale alternating leucocratic and melanocratic layers, is locally ptygmatically or isoclinally folded (Fig. 7b). The rock package is cut by, and sinistrally offset along, the late-tectonic, north-northeasterly trending Deadman Fault (DMF) and associated splays (Fig. 6).

The predominant rock type is quartzofeldspathic biotite(–cordierite–garnet) gneiss, with prominent millimetre- to centimetre-scale, garnet-rich, leucocratic layers defining a stromatitic migmatite texture locally containing 50 cm long, garnet-rich, leucocratic boudins (Fig. 7c). These leucocratic layers are interpreted to be leucosomes that developed during crustal anatexis at peak metamorphism. The gneisses also contain biotite-rich lenses up to two metres thick, which are interpreted as metamorphosed remnants of pelitic horizons, and psammitic layers up to 10 m thick (Fig. 7c,d). The entire package is intruded by pegmatite veins (Fig. 7a) up to 10 m wide. Fine-grained amphibolite-rich layers up to five metres thick are also locally intruded by thin, leucocratic veins, interpreted as leucosome melts. Each unit strikes east-northeasterly, parallel to the gneissic banding. A northerly trending, 700 m long, 10 m wide, postmetamorphic dolerite dyke cuts across all other fabrics in the area.

The southern half of the field area, around Paradise Well, is dominated by migmatitic quartzofeldspathic biotite–cordierite–sillimanite–spinel(–garnet) gneisses interleaved with discontinuous pods of mafic granulite, psammite, pelite, pegmatite and amphibolite. The gneisses have been interpreted as a pelitic metatexite (Johnson et al., 2010; Sheppard et al., 2010; Johnson et al., 2011b). The occurrence of leucosomes and melanosomes in addition to psammitic horizons (Fig. 7d) suggests an interlayered psammite and pelite protolith to the gneisses; most melting would have originated from the pelitic horizons as pelites typically have a lower partial-melting temperature than psammites (e.g. experimental results by Brown and Korhonen, 2009). The presence of cordierite, sillimanite and spinel suggests that rocks south of the inferred thrust reached granulite facies, whereas gneisses hosting the Glenburgh deposits to the north — which typically lack this high-temperature metamorphic assemblage — may have been metamorphosed to only upper amphibolite or lower granulite facies. This difference could be explained by 'normal' P–T gradients over the few kilometres separating the north and the south of the field-mapping area if the succession was tilted through 90° subsequent to metamorphism; alternatively, rocks of different metamorphic grade could have been juxtaposed by faulting, or have had different melting temperatures because of differences in internal fluid activities.

A ferruginous, coarse-grained metasandstone unit overprinted by magnetite lies to the north of the deposit trend and runs strike-parallel to the main east-northeasterly regional structures. It forms a prominent magnetic high within the TMI image (Fig. 8) and has been used as a marker unit for exploration and delineating fault offsets.

### Structure

The region hosting the Glenburgh deposit has been exposed to two major deformation and metamorphic events corresponding to the subduction phase of the Glenburgh Orogeny ($D_{1g}/M_1$) and the collisional phase (Yilgarn Craton with the amalgamated Glenburgh Terrane – Pilbara Craton) of the Glenburgh Orogeny ($D_{2g}/M_2$).

The oldest identifiable fabric is the main gneissic layering ($S_{1g}$). The gneissic layering dominantly strikes east-northeasterly and dips steeply to the north and south, and the mineral lineation typically plunges steeply north

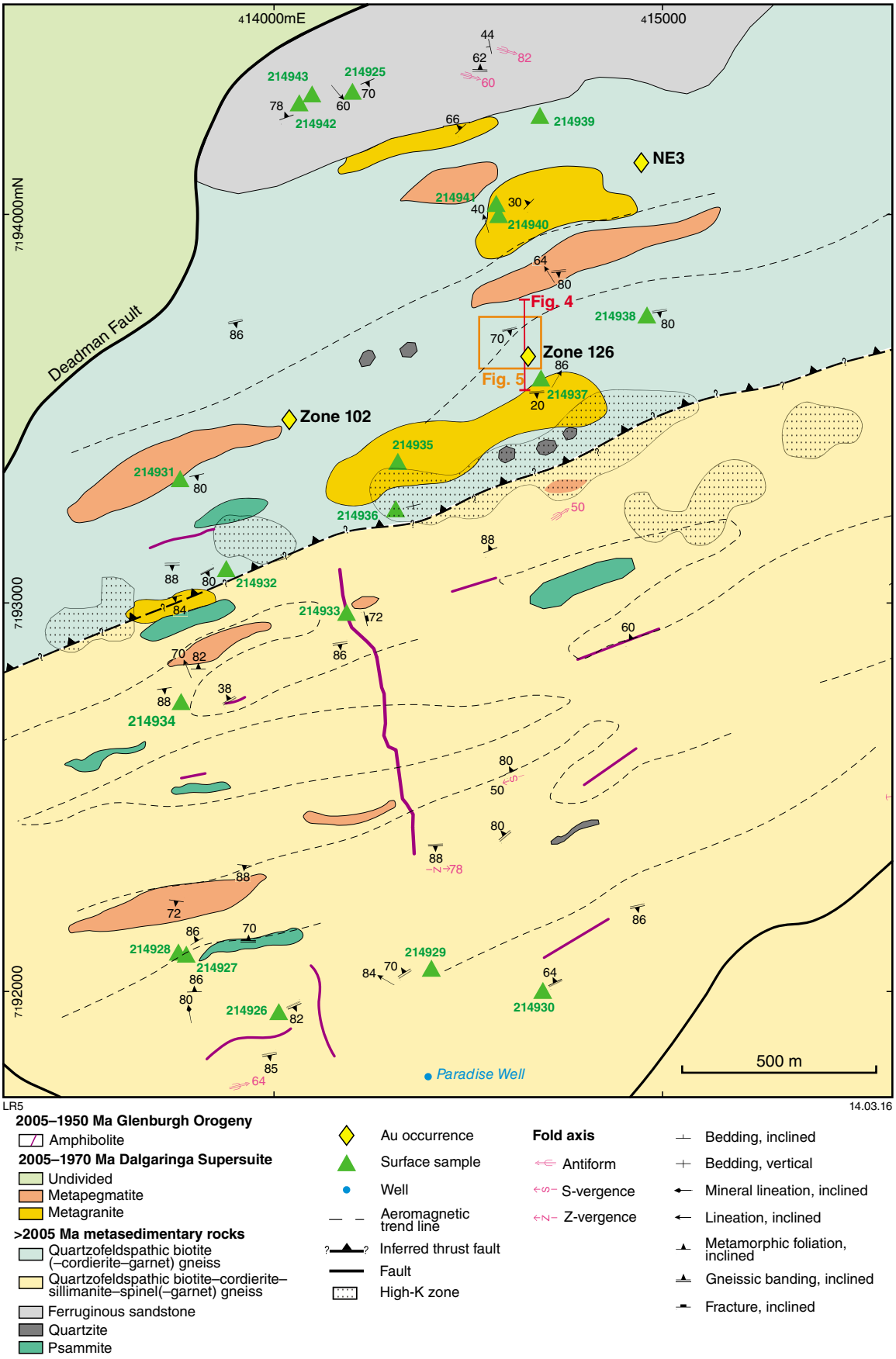


**Figure 6. Interpreted bedrock geology map of the field mapping area. See Figure 3 for location**

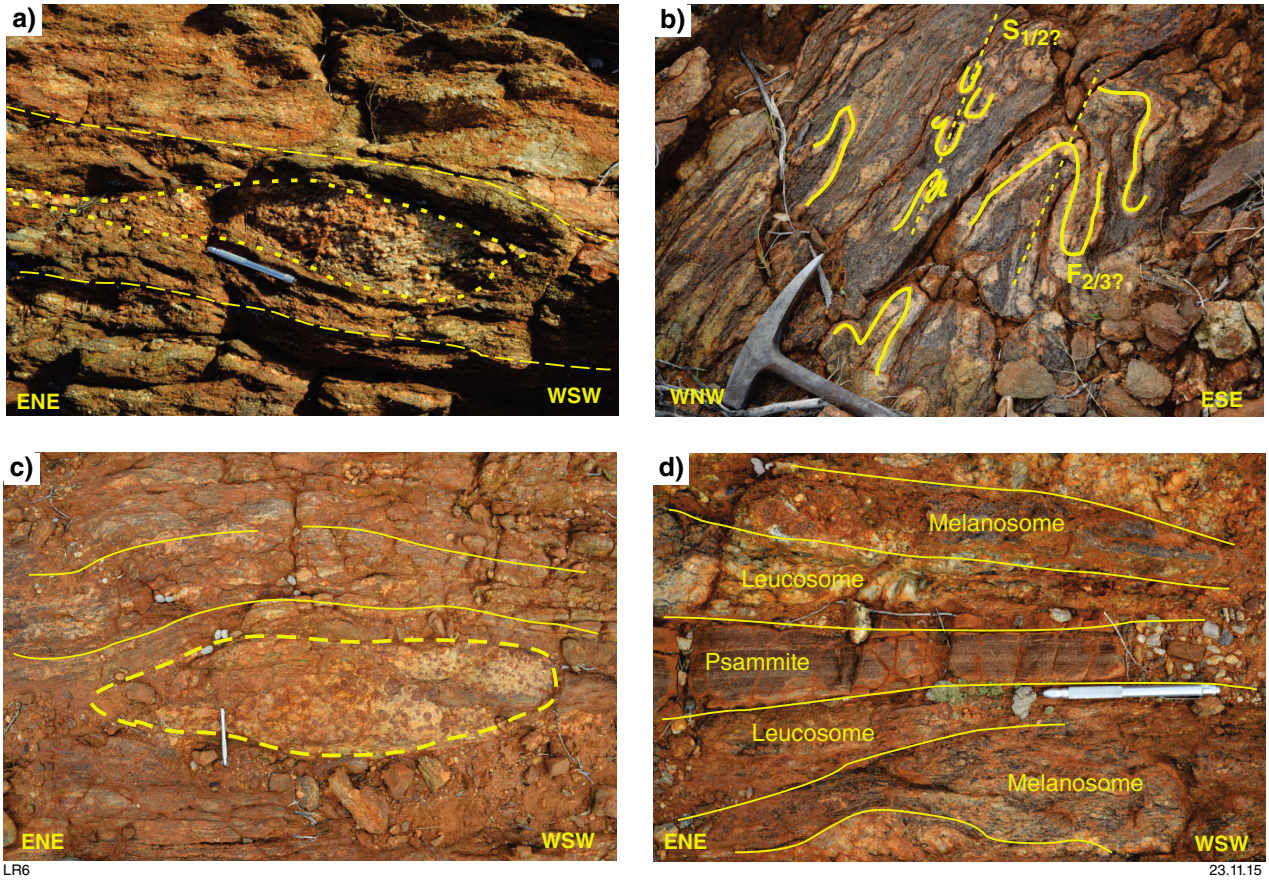


**Figure 7. Photos of key field outcrops for structure: a) pegmatite boudin within pelitic gneiss, view from above; b) leucocratic layers folded within biotite melanosome, potentially recording local $S_1$ or $S_2$ foliation (differentiated?) folded by ?$F_{2/3}$; c) boudin of quartz–plagioclase–garnet leucosome (note the large percentage of garnets); d) psammite layer bounded by melanosome and leucocratic layers. Note that a pen is used for scale in a), c) and d).**

(Fig. 9). This fabric is defined by coherent layer-parallel leucosomes, suggesting that the oldest deformation event in the area ($D_{1g}$) was accompanied by peak metamorphism ($M_1$). Peak metamorphism, partial melting and leucosome crystallization have been dated at Paradise Well at 1997 + 10 Ma (Wingate et al., 2010; Johnson et al., 2010, 2011b).

The gneissic fabric is locally folded about isoclinal $F_2$ folds (Fig. 10a). $F_2$ folds are characterized by east-northeasterly trending axial planes and moderately easterly plunging fold axes (Figs 6 and 9). Ptygmatic and isoclinal folding of the gneissic fabric could represent continuing $D_{1g}$ or correspond to the later $F_2/D_{2g}$ event. Retrogression is more prevalent to the north, marked by common biotite clots as pseudomorphs after garnet. The replacement of garnet — a $D_{1g}$ peak metamorphic mineral — led to the interpretation that retrogression was associated with $D_{2g}$ in some localities.

Landsat, aeromagnetic and radiometric data have been used to extrapolate and interpret the geology of the surrounding region. Asymmetry in magnetic response as seen in the 1VD-TMI image supports a north-northwesterly dip direction of folded gneissic units (Fig. 8). Asymmetric closures of magnetic trends (Fig. 8) are interpreted as regional-scale, east-northeasterly trending, S- or Z-verging folds whose orientations are consistent with field observations. There is an increase in magnetic susceptibility of the host rocks immediately to the south of the deposit trend (Fig. 8), which corresponds with a high-K anomaly in the radiometric data (Fig. 11).

The TMI data also show that the region is cut by a number of significant faults. The northeasterly trending Deadman Fault and associated splays appear to be relatively late structures inasmuch as they offset both $D_{1g}$ and $D_{2g}$ fabrics, though the absolute timing of the fault movement is unknown. There has been at least 1.6 km of sinistral movement along the Deadman Fault, defined by offset of the ferruginous metasandstone marker unit in the northern part of the mapping area (Fig. 8). If the effects of movement along the DMF are removed so that the ferruginous metasandstone unit is restored to a continuous unit, and the effects of other faulting are also then removed in the correct order, the Glenburgh gold deposits then define three parallel, east-northeasterly trending bands, rather than a single linear trend (Michael Dunbar, 2014, written comm., 20 August). The higher grade Zone 126 and Zone 102 lodes would then have occupied

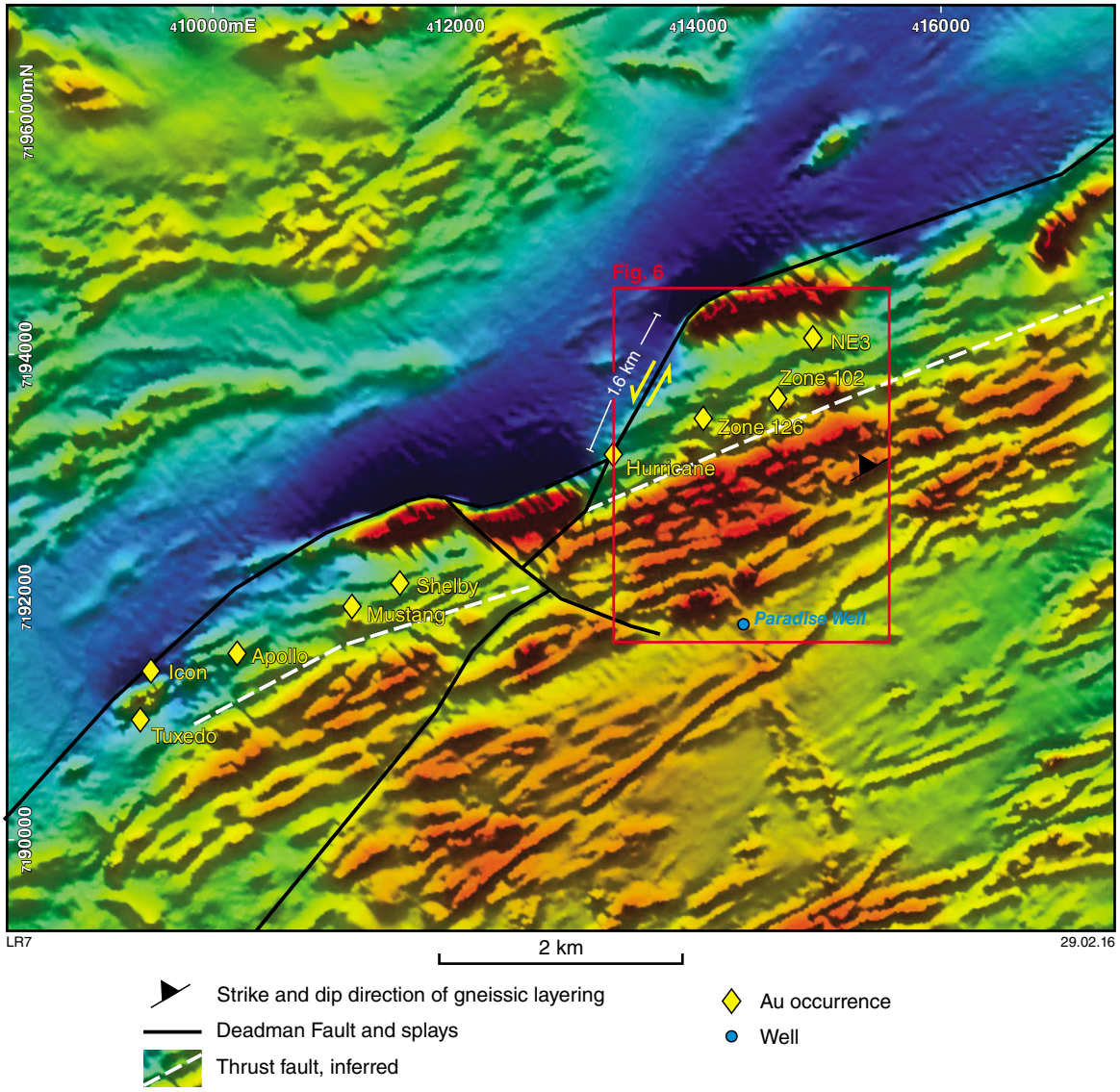


**Figure 8.** **First vertical derivative (1VD) of the total magnetic intensity (TMI) image over the project area (Gascoyne Resources Ltd, written comm., February 2014) and location of the known mineral deposits (yellow diamonds). Dashed line represents the inferred location of a thrust fault. Red frame shows field mapping area (see Fig. 6). Red line shows location of cross-section in 4b).**

the southern band, with a central band containing the Hurricane, Shelby, NE3 and Mustang lodes, and the larger, lower grade Icon, Tuxedo and Apollo lodes occupying the northernmost trend.

The TMI data also reveal that the rocks to the south of the ferruginous metasandstone and DMF are dominated by east-northeasterly trending magnetic anomalies, commonly with a relatively high magnetic intensity, whereas the rocks north of the ferruginous metasandstone have a distinctly suppressed magnetic signature. Radiometric data show higher potassium (K) and thorium (Th) concentrations in the south compared to the north, and Landsat imagery shows relatively higher levels of ferrous iron in the south, and a higher clay and vegetation signature in the north. The northern package is interpreted by Aitken et al. (2014) as a potentially younger package of Dalgaringa Supersuite, juxtaposed along the DMF against older Dalgaringa Supersuite hosting the Glenburgh mineralization.

## Visual and hyperspectral logging of drillhole samples

Several rock units are visually recognizable in the drill samples: biotite–quartz–anorthite(–garnet) gneiss, biotite–phlogopite(–garnet) gneiss, amphibolitic gneiss and late-stage quartz(–chlorite) veins (Fig. 12). Metapegmatitic and metagranitic units observed in the field, including within the ore zone, were not intersected in the drillholes.

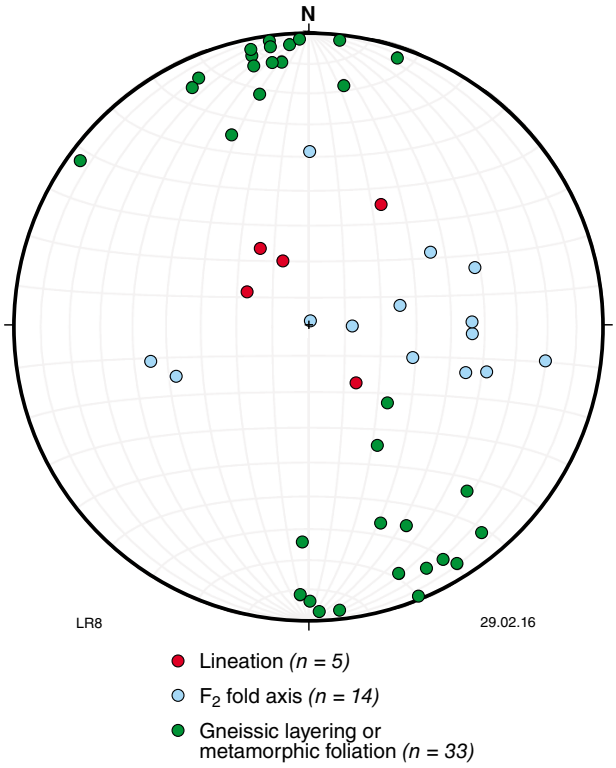


**Figure 9. Lower-hemisphere equal-area stereographic projection of field structural measurements. Green dots represent poles to gneissic layering showing a consistent east-northeasterly trend and dipping steeply either to the north-northwest or to the south-southeast (*n* = 33); red dots represent steeply (mostly) north-plunging mineral lineations (*n* = 5), blue dots represent $F_2$ fold axes which (mostly) plunge moderately to the east (*n* = 14)**

A strong gneissic fabric affects all rocks in the core — except the late stage quartz(–chlorite) veins — striking east-northeasterly and dipping steeply (~80°) north-northwest (Fig. 10b,c).

Gneissic banding is defined by alternating leucosomes, of predominantly quartz – plagioclase feldspar, and melanosomes largely comprising biotite–phlogopite. Disseminated sulfides — predominantly pyrrhotite, pyrite and minor chalcopyrite — can be seen in a preferred crystal orientation in line with gneissic banding ($S_{1g}$). Some melanosomes contain either discontinuous bands or blebs of coarse (~1 cm) quartz and feldspar or quartz–feldspar as fine-grained aggregates in thin bands, suggesting stretching or flattening (Fig. 10b,c).

Garnet porphyroblasts are common in melanosomes and leucosomes, and are much larger and abundant in the latter (up to 2–3 cm in diameter). Cordierite was detected from 180–200 m downhole in GBD011 (Fig. 13) and has been confirmed in thin section (GSWA 214901). Cordierite is a good indicator of metamorphic conditions and suggests high temperatures and low pressures. Isoclinal folds have been documented in quartz-rich leucosomes, garnet accumulations and melanosomes (in thin section) and have axial planes that strike moderately east-northeasterly (Fig. 10a). The complete package of rock types at the Glenburgh deposit is interpreted to be tightly folded along this orientation, with the exception of the late quartz–chlorite veins, which cross-cut the gneissosity and post-date all the gneissic fabrics and folds.

The amphibolitic gneisses contain minor quartz-only veins that are folded by east-northeasterly trending $F_2$ folds, indicating that quartz-vein emplacement was prior to, or contemporaneous with, development of the dominant east-northeasterly trending, folded gneissosity. Interpretation of thin sections and XRD and SEM data has resulted in identifying the presence of hornblende, tschermakite, actinolite and tremolite. Tschermakite is a rare amphibole, and, although XRD and SEM results are semiquantitative, Ca-rich amphibole is classified as tschermakite from here onwards.

Hyperspectral data have been used to further validate visual drillhole logging and test for differences in visually similar rock types. Rock units dominated by leucosomes, melanosomes or amphibolite were clearly distinguished in the data from the abundant presence of quartz, micas, amphiboles or plagioclase (Fig. 13). The predominant white micas are muscovite and paragonite, and the dark micas are predominantly biotite and phlogopite.

Hornblende is the predominant amphibole detected by the HyLogger. Tschermakite, tremolite and actinolite were only locally detected, even in intervals where their presence had been confirmed in thin section. Amphiboles are best identified in the SWIR wavelength range; however, the mineral reference database used for mineral identification contains no SWIR data for tschermakite. Amphiboles can be identified in the TIR range, although the response is highly dependent on crystal orientation (Hancock et al., 2013), and TIR reference spectra for amphiboles other than hornblende are only available for crystals in upright orientations, which are likely to be uncommon in these highly deformed rocks. Therefore, hornblende abundance, in respect to other amphibole compositions, is potentially over-represented in the TIR HyLogger results.

Rock chips from the RAB pre-collars for diamond holes GBD011, GBD013, GBD016 and GBD021 (Appendix 3; Table 1) have been scanned in the SWIR and VNIR ranges using HyChips, and highlight a high proportion of white mica and chlorite at the Icon lode relative to the Zone 126 lode, where dark micas dominate (Appendix 3). Chlorite and biotite have very similar absorption spectra, with troughs at 2254 and 2347 nm for chlorite and at 2255 and 2350 nm for biotite (Pontual, 2008). The apparent abundance of chlorite may be an artefact of interpretation by the software, which typically prefers chlorite over biotite. However, core from another drillhole at the Icon lode (GBD031; Appendix 3) that was scanned across the VNIR, SWIR and TIR range also contains abundant chlorite and white mica, suggesting that substantial late-stage alteration has taken place at the Icon lode.

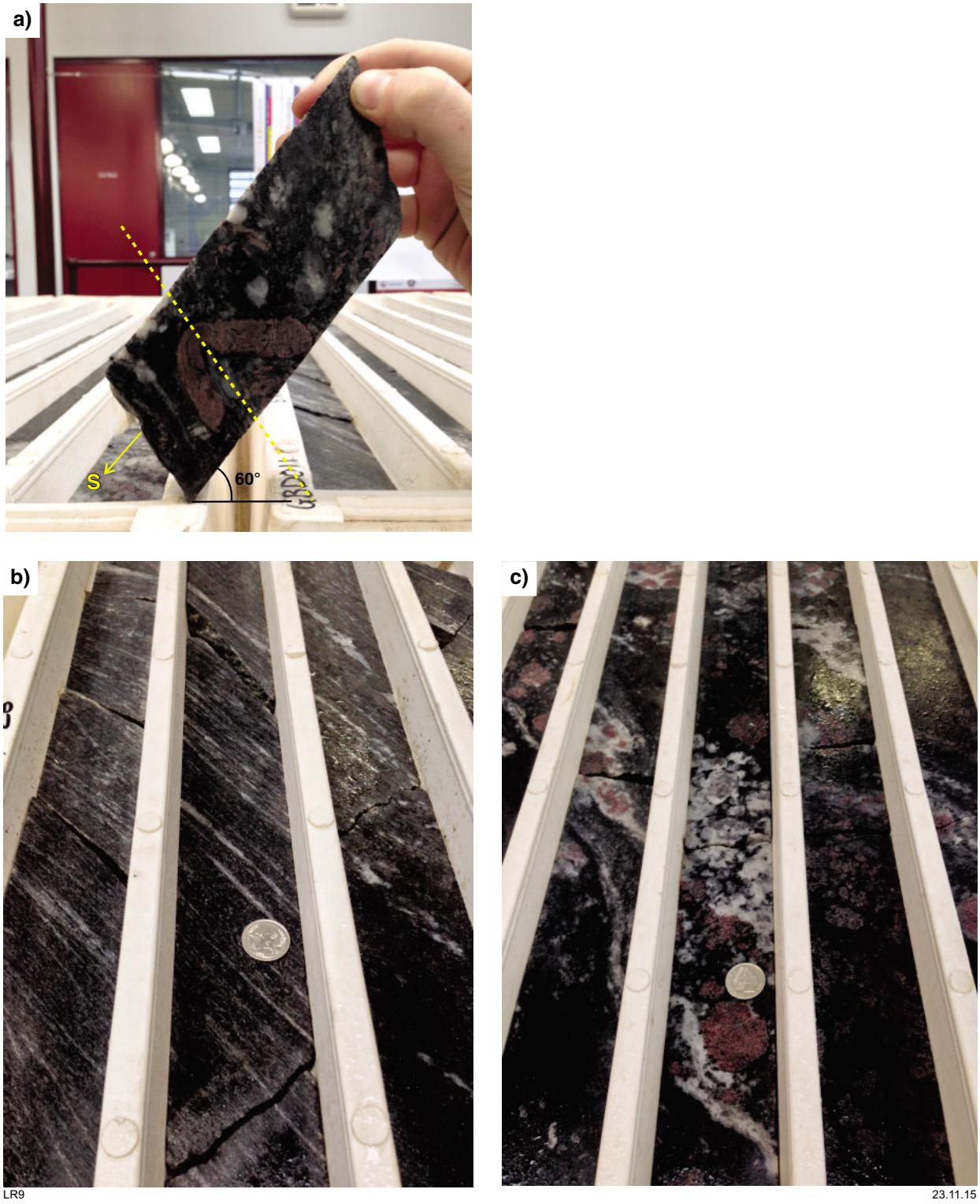


**Figure 10. Oriented drillcore (5 cm diameter) with folded garnet aggregates and migmatites deformed to varying levels of strain: a) orientated core (plunging 60° towards 185°; GBD011 222.3 – 222.4 m) with a folded garnet aggregate; gneissic layering dips north; b) highly strained and stretched biotite–quartz–feldspar gneiss (GBD011 291–293 m); c) weakly deformed biotite–quartz–feldspar gneiss; quartz and feldspar clasts are coarse and show little evidence of stretching (GBD011 178 – 180.5 m)**

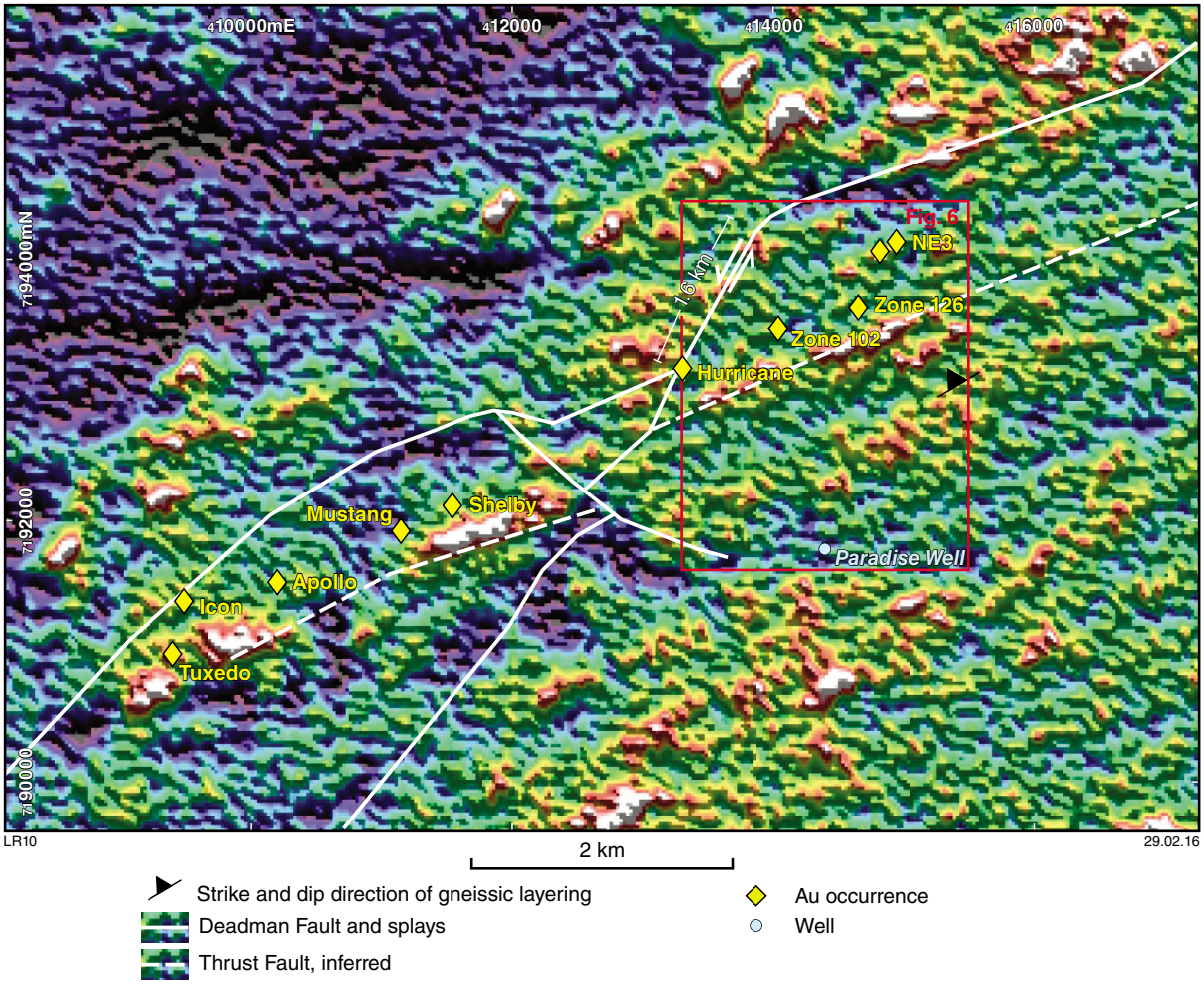


**Figure 11. Potassium radiometrics image of the project area (white – highest potassium values; blue – lowest potassium value). Image processed with north shading. Note the strong correlation (white dashed line) between the Glenburgh deposit trend and a possible boundary between granulite facies rocks and upper amphibolite facies rocks (shown in Fig. 6). Red frame shows field mapping area (see Fig. 6). *Source*: Gascoyne Resources Ltd**

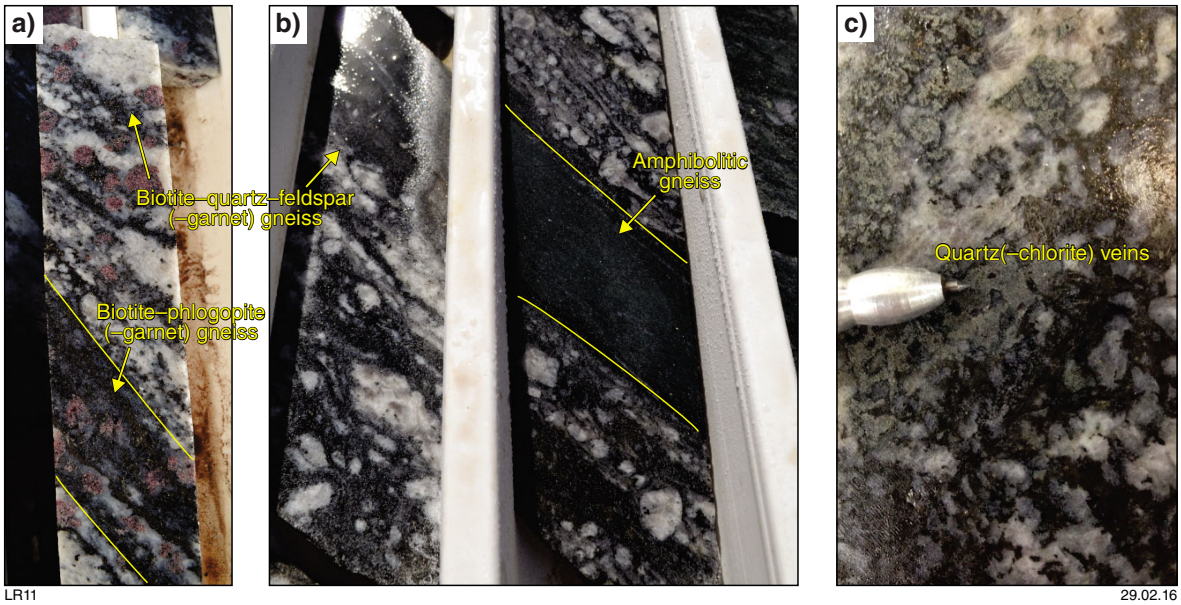


**Figure 12. Representative images of drillcore lithologies: a) core with biotite–quartz–feldspar(–garnet) gneiss and biotite–phlogopite(–garnet) gneiss; b) biotite–quartz–feldspar(–garnet) gneiss and amphibolitic gneiss; c) quartz(–chlorite) veins**

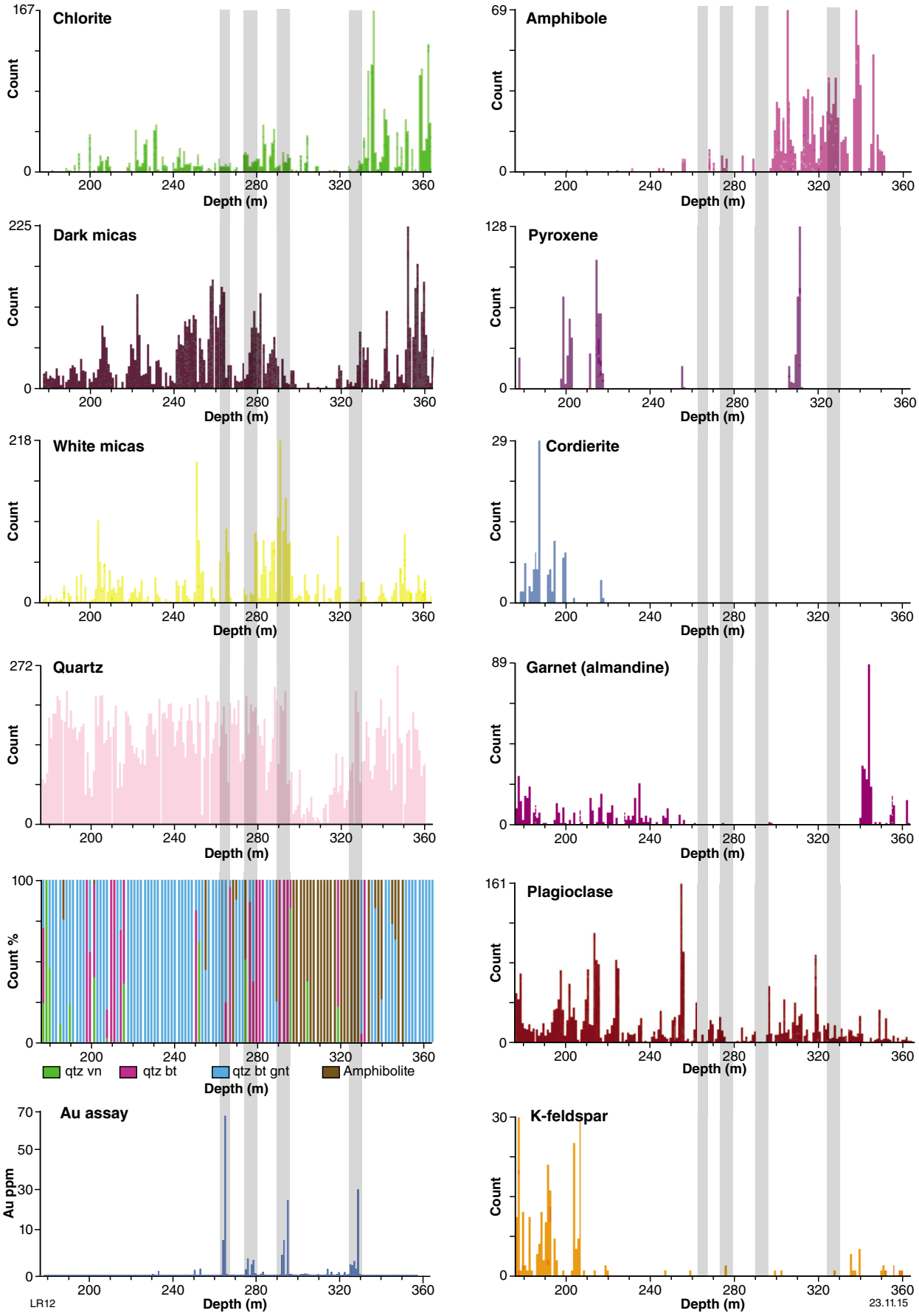
Chlorite
Count
167
0
200
240
280
320
360
Depth (m)
Amphibole
69
Dark micas
225
Pyroxene
128
White micas
218
Cordierite
29
Quartz
272
Garnet (almandine)
89
Count %
100
qtz vn
qtz bt
qtz bt gnt
Amphibolite
Plagioclase
161
Au assay
Au ppm
70
50
30
10
K-feldspar
LR12
23.11.15

**Figure 13. (left) HyLogger results for drillhole GBD011, highlighting each major mineral group relative to gold content. Intervals of high gold grade have been highlighted by grey shading. Count rate specifies how many times the sample was found in a metre interval. This shows that there is no obvious relationship between gold grades and specific minerals. Simplified lithological logging was added (bottom left) including: qtz vn = quartz vein; qtz bt = quartz–biotite gneiss; qtz bt gnt = quartz–biotite–garnet gneiss**

Drillholes at the Icon lode typically intersected a surface clay horizon to a depth of about 20 m, which can be interpreted as nontronite and montmorillonite based on HyLogger results. The clay horizon at the Zone 126 lode was typically only about two metres deep, suggesting a much deeper weathering profile that may be a result of more intense alteration at the Icon lode, perhaps related to its close proximity to the DMF.

Assay data have been compared with visual and hyperspectral logging to determine if there are detectable systematic relationships between host-rock mineralogy and gold mineralization, which might reflect alteration or pathfinder elements towards and within ore zones. Occurrences of visible gold and collective gold grades greater than 1 ppm show no preference for any specific lithological unit, although intervals of relatively high-grade mineralization (>10 ppm Au) do appear to be contained in amphibolite, biotite–quartz gneiss and, in one observation, a quartz–chlorite vein. The boundaries of an amphibole-rich region bounded by downhole depths of 300 and 330 m in drillhole GBD011 correspond with gold grades up to 35 ppm. There are also a few cases where gold grades greater than 5 ppm exist within a metre of the contact between gneiss and either amphibolite or quartz veins (e.g. GBD013 at 200 m, GBD016 at 180 m, GBD011 at 275 m), although this is not a consistent relationship. The HyLogger cannot presently recognize sulfides from SWIR or TIR data, although a measurement of the infrared background offset does highlight domains in the drillcore with high reflectance, the peaks of which commonly correspond to visible sulfides — in this case, pyrrhotite. Significant gold assays do not always correspond with the presence of sulfides, and vice versa; so the presence of sulfides alone in the drillcore and chips is not an indication of gold mineralization (Fig. 14). The possible presence of pyrrhotite, a magnetic sulfide and magnetite, was determined by measuring magnetic susceptibility with a KT-10 meter on dry drill samples, typically at one-metre intervals, although at closer spacing (~30 cm) towards ore zones. There is no correlation between gold grades and magnetic susceptibility (Fig. 15).

# Petrography

## Host-rock mineralogy

The thin-section mineralogy of rock types at the Glenburgh deposit can shed light on metamorphic conditions, structural history and mineral paragenesis (Fig. 16), and was as expected from field mapping. All gneiss samples comprise prograde assemblages of biotite–quartz–plagioclase–feldspar(–garnet), which are stable at upper amphibolite-facies conditions. The gneissic banding is predominantly defined by alternating leucosomes and melanosomes. Microcline is not prominent, although is locally abundant in several of the gneissic, granitic and pegmatite units (GSWA 214926, 214928, 214929, 214932, 214934, 214935, 214940), and gneissic banding is sporadically defined by alternating coarser and finer grained quartz and microcline crystals.

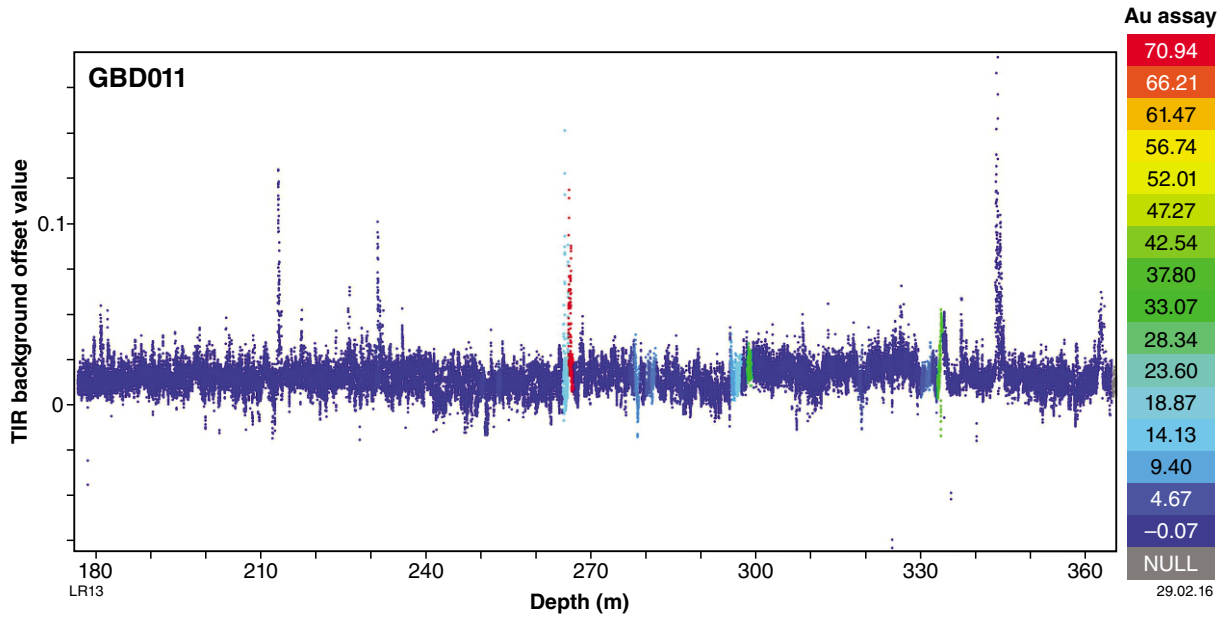


**Figure 14. Downhole Au assay values (ppm) compared to the thermal infrared background offset (TIRBkgOffset) values. Peaks (high reflectivity ~0.1) in TIRBkg Offset readings highlight areas where sulfides have been detected.**

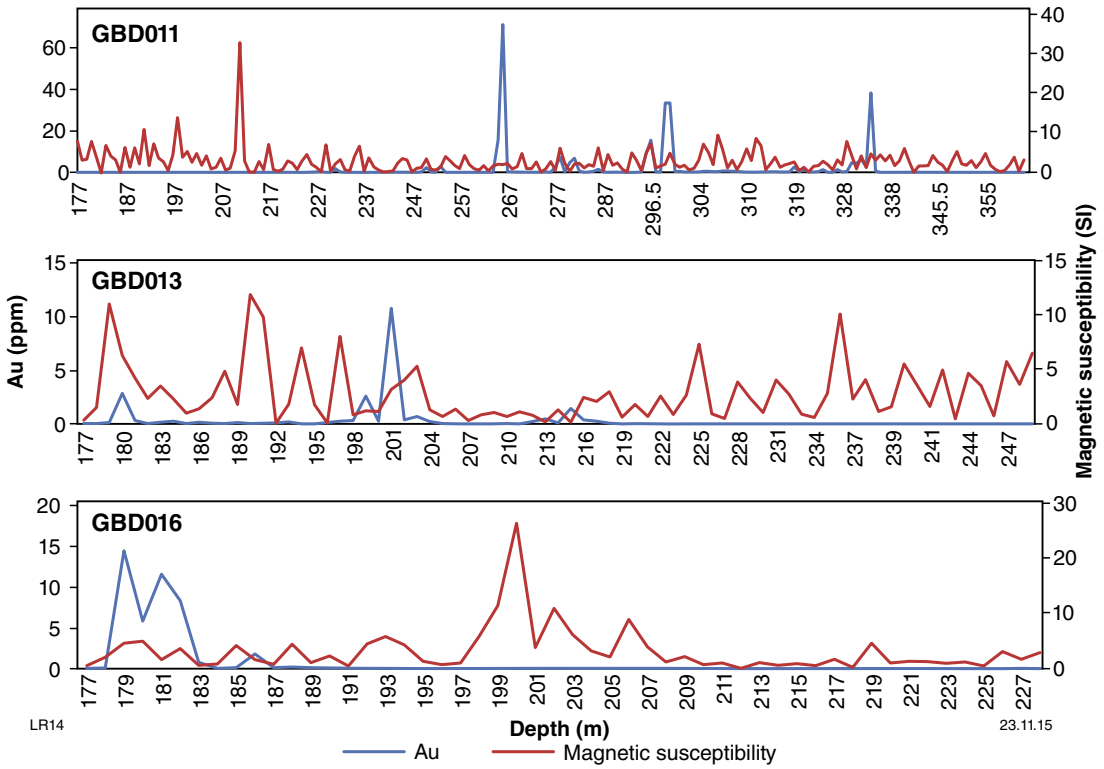


**Figure 15. Magnetic susceptibility measurements (SI units) against Au assays downhole for drillholes GBD011, GBD013, GBD016 (from Zone 126)**

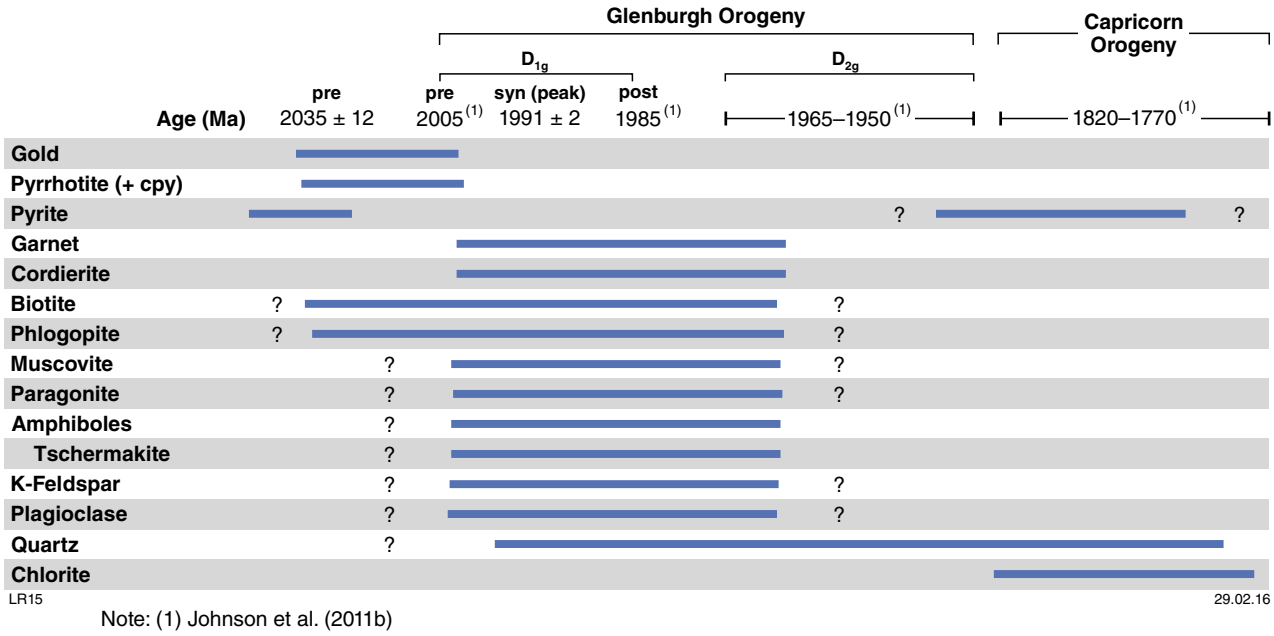


Note: (1) Johnson et al. (2011b)

**Figure 16. Paragenetic table outlining the relative timing of crystallization of minerals observed in thin section. Horizontal axis shows timing of events in the Glenburgh Orogeny in millions of years. Refer to text for discussion of new dates from this study (2035 + 12, 1991 + 2)**

Leucosomes are coarse grained (>0.5 mm), consist of quartz–plagioclase–feldspar(–garnet–cordierite–tschermakite), and are folded and aligned with the regional east-northeasterly striking gneissosity. Scanning electron microscopy data show that the dominant plagioclase feldspar within the leucosomes is likely to be anorthite (Table 5). X-ray diffractometer results suggest the garnet is likely to be almandine, or possibly a Ca-poor and Mg-rich variety (GSWA 214901, 214910). Garnet grains are commonly heavily fractured (Fig. 17a). Cordierite was observed in association with quartz-rich leucosomes in several samples (GSWA 214901, 208326, 208331, 208344; Fig. 17b) and, as with garnet, is a useful indicator of metamorphic conditions, suggesting high temperatures and relatively low pressures. The melanosomes are fine grained, consist of biotite and phlogopite with quartz(–garnet), and are folded and aligned with the regional east-northeasterly striking gneissosity.

Amphibolites comprise hornblende–quartz(–orthopyroxene–plagioclase–chlorite–tremolite–tschermakite), as validated by SEM and XRD (Appendix 2). The calcic amphiboles have crystallized with long axes subparallel to the axial plane of isoclinal folds, suggesting crystallization prior to, or during, the $D_{1g}$ deformation event. Tschermakite was identified in two main associations through SEM analysis across several samples (Table 4): with Au in an amphibolite in sample GSWA 214909 (Fig. 18) and, secondly, as trains that are folded with quartz–biotite gneiss and are associated with the leucocratic minerals and along margins of folded biotite layering (e.g. GSWA 214906; Fig. 19a).

## Gold textures and geochemistry

The textural relationships between gold and other silicate and sulfide phases have been examined to determine timing of mineralization relative to deformation and metamorphism. Sample GSWA 214909 contains several disseminated, commonly subrounded gold grains up to about 100 µm in size that are not associated with any sulfides (Fig. 18). Smaller gold grains are concentrated around the edges of larger grains. The main minerals associated with gold in this sample are tschermakite and ilmenite (Figs 18 and 20a). The boundaries of some elongate gold grains are aligned with those of the surrounding tschermakite grains (Fig. 18). Gold fills fractures in both minerals (Fig. 20b) and appears along sealed fractures in a large ilmenite grain or as trails of inclusions. Two grains of apatite were identified in sample GSWA 214909 using SEM, and both were associated with gold grains (Fig. 20c). The larger apatite grain fills a void within the tschermakite and contains a void in the middle of the grain itself, suggesting growth was from the outside in (Fig. 20c). The smaller apatite grain contains small (<1 µm) inclusions of gold in bands close to the grain boundary on two, opposite, sides and not along the fractured side.

Acid etching of single gold grains reveals polygranular structures with variably sized subgrains ranging from 2 µm up to 30 µm across. A high-purity gold 'veinlet' between subgrains is present in GSWA 214909. The veinlets are pronounced, and highlighted by darker outer rims showing initial disintegration of subgrains (Fig. 21a).

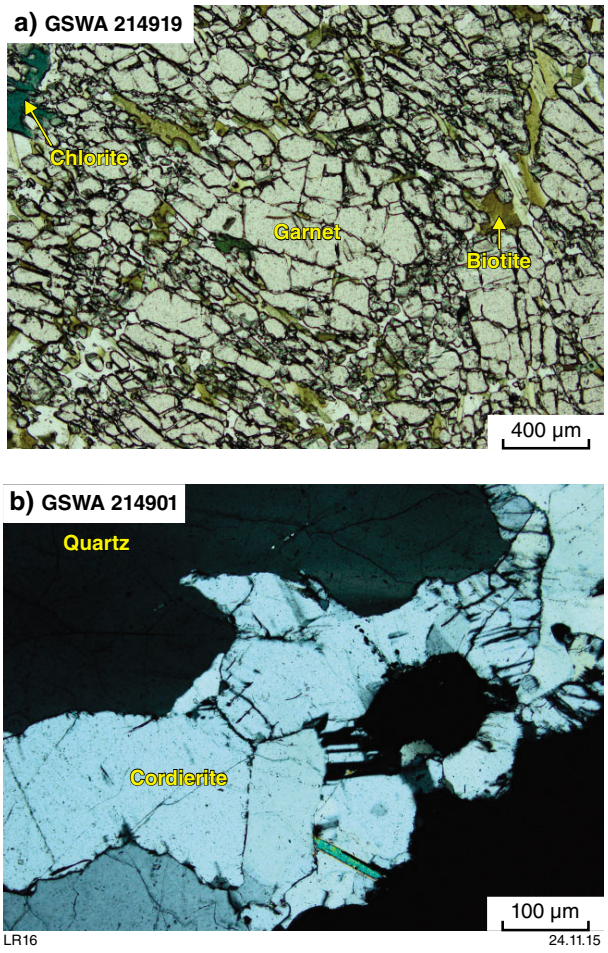


**Figure 17. Photomicrographs of garnet and cordierite in thin sections from drillcore: a) fractured garnet grain with minor biotite and chlorite within a quartz–feldspar–biotite–garnet gneiss (GSWA sample 214919, plane-polarized light; GBD013); b) cordierite associated with quartz in quartz–feldspar–garnet gneiss (GSWA 214901; crossed polars; GBD011)**

**Table 4. Element quantities taken using the SEM of an unknown mineral (214909a 5, location of reading shown in Fig. 14a) associated with gold grains. Elements suggest this mineral is a calcium amphibole and most likely tschermakite.**

| *Spectrum* | *O* | *Na* | *Mg* | *Al* | *Si* | *K* | *Ca* | *Ti* | *Fe* |
|---|---|---|---|---|---|---|---|---|---|
| GSWA 214909 | 42.185 | 1.349 | 5.543 | 9.358 | 19.663 | 0.294 | 7.917 | 0.516 | 13.175 |

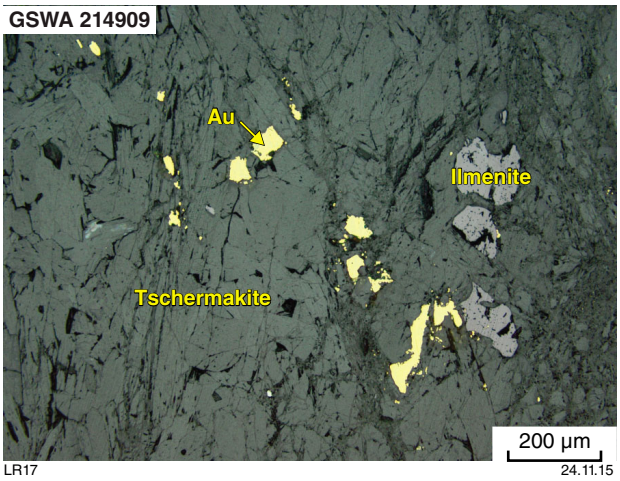


**Figure 18.** Reflected light photomicrograph showing gold grains in tschermakite (main groundmass) and ilmenite (grey); GSWA 214909

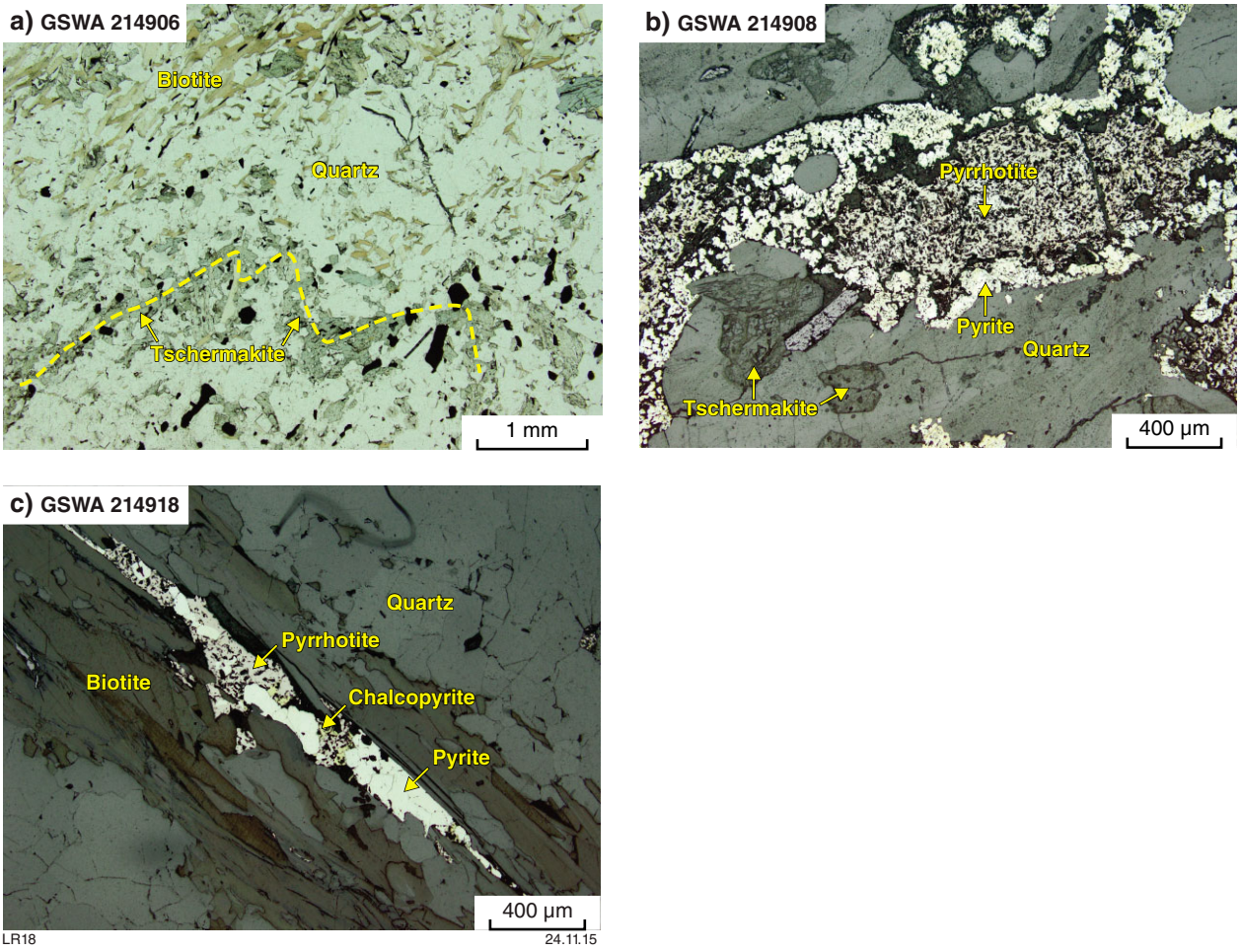


**Figure 19.** Photomicrographs of thin sections from dillcores GBD011 and GBD013 showing sulfide and tschermakite relationships: a) calcic amphibole (tschermakite) folded (dashed yellow line) within fine-grained leucocratic material. Biotite is aligned in the same direction. Quartz–feldspar–biotite gneiss GSWA 214906 (plane-polarized light); b) pyrrhotite replaced by pyrite around grain boundary. Quartz–amphibole–biotite gneiss GSWA 214908 (reflected light); c) pyrite, pyrrhotite and chalcopyrite association within biotite–quartz gneiss. Early and late pyrite phases are seen. GSWA 214918 (reflected light)

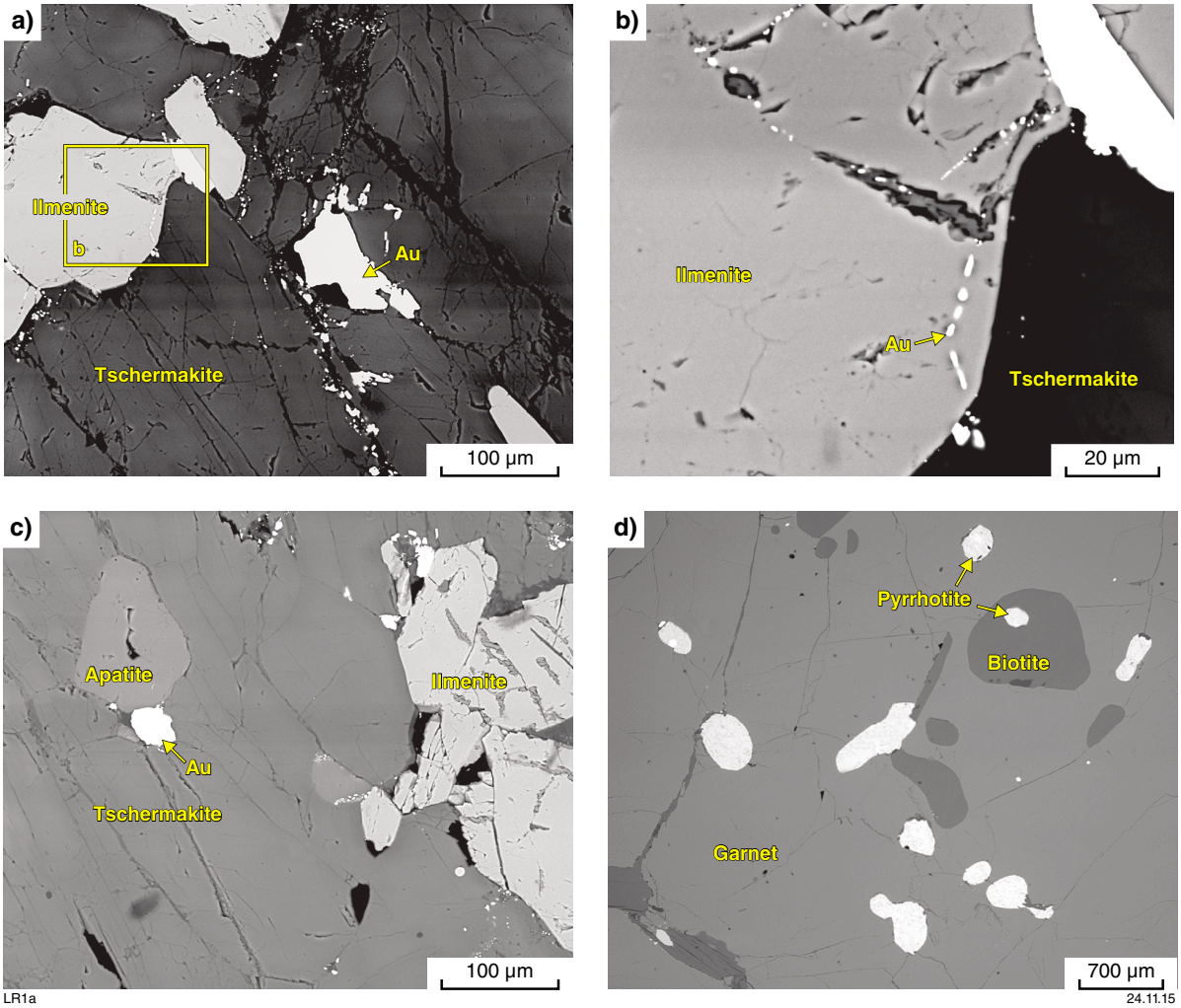


**Figure 20.** SEM images of gold grains and sulfides with associated host rocks: a) gold (brightest) with ilmenite (grey) and tschermakite (dark); b) gold grains along sealed fractures (or as inclusions) within an ilmenite grain; c) gold associated with two apatite grains. The labelled apatite grain to the top left appears to have grown from the outside inwards, within a fracture zone in the tschermakite host, indicating late growth timing; d) well-rounded pyrrhotite grains (light grey) with chalcopyrite inclusions. Blebby biotite (darkest) with distinctive cleavage planes (lower left). Both within a garnet grain. Note the well-rounded inclusion of pyrrhotite within a rounded biotite grain. Samples numbers: a)–c) GSWA 214909; d) 214901

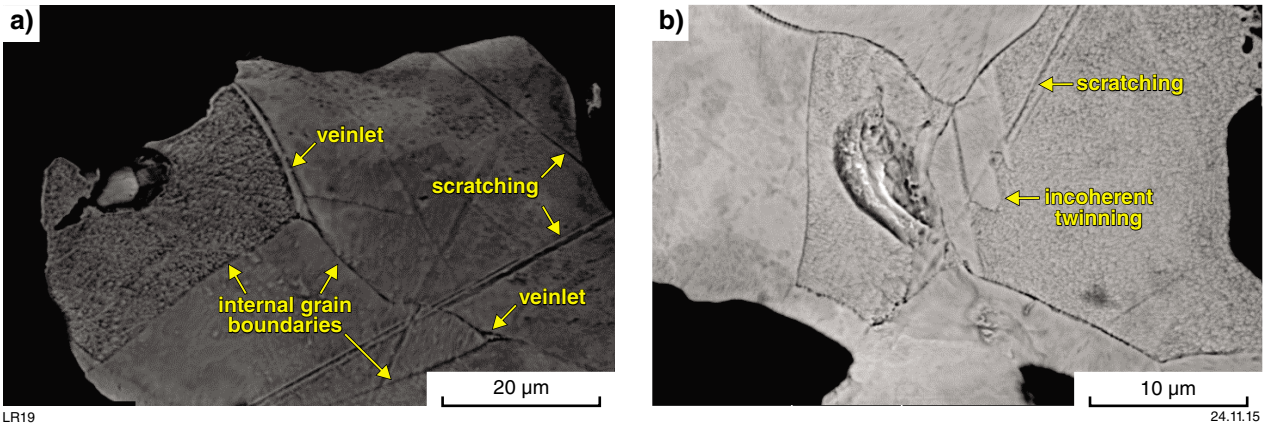


**Figure 21.** Etched gold under SEM. Scratching along the surface of gold grains should not be confused with grain boundaries; a) internal grain boundaries and intergranular high-purity gold veinlets (highlighted by arrows), likely to have been caused by silver leaching on grain boundaries (GSWA 214909); b) incoherent twinning broken off at the edges of an internal gold grain (highlighted by arrow), characteristic of thermal annealing (GSWA 214909)

**Table 5. Element quantities taken using the SEM (repeated in several locations and averaged) of plagioclase feldspar. Elements suggest this mineral is anorthite.**

| *Chemistry* | *$SiO_2$* | *$Al_2O_3$* | *$Fe_2O_3$* | *CaO* | *$Na_2O$* |
|---|---|---|---|---|---|
| GSWA 214902 | 44.35 | 33.01 | 3.12 | 16.11 | 1.37 |

This veinlet possibly formed during leaching of silver along internal grain boundaries, which is an idea further supported by the typically very low silver contents (between 0.5 and 2% Ag) within all gold grains analysed by SEM (Fig. 21a). Incoherent twinning was observed in the same grain (Fig. 21b).

Sixty-seven trace elements (including Ag) have been determined in native gold and neighbouring minerals, using LA–ICP–MS (Table 2). Only the largest (~100 μm) gold grains returned values free of contamination from the surrounding host rock (Au-only spot analyses 1, 2 and 3 in Table 2), and their composition is taken as being representative of the composition of gold from the Glenburgh deposit. Elements returning a robust, consistent response above 1000 cps comprise silicon, silver, copper, mercury and palladium (Si: 120 000–540 000 cps; Ag: 6 200 000–11 300 000 cps; Cu: 40 000–65 800 cps; Hg: 51 000–65 800 cps; Pd: 3000–3400 cps). The elements Ag, Hg, Cu and Pd can exist in solid solution with Au (Nikolaeva et al., 2004). Their presence in the Au-only spot analyses of the Glenburgh deposit samples, and the positive correlation between Au and each of these elements, suggest that they exist in solid solution within the gold grains, rather than representing submicroscopic mineral inclusions from surrounding host rocks (e.g. see spot analyses 8, 9 and 21, host-rock only). The presence of Si may be derived from submicroscopic mineral inclusions of host rock. Alternatively, a silicon torch was used during analyses, so all silicon results are discounted from further consideration.

## Sulfide mineralogy

Pyrrhotite is the major sulfide in the drillcore (between 0.1 and 5%), and is disseminated and associated with grain boundaries of minerals such as biotite, quartz and garnet. Trace chalcopyrite inclusions are common. Pyrite commonly rims or replaces pyrrhotite (Fig. 19b,c), and is observed as veins that cross-cut the gneissic fabric. Trace amounts of pentlandite and cobaltite were also identified using the SEM, as inclusions within pyrrhotite, although these are rare. Pyrrhotite and pyrite are less prominent in the amphibolite and do not show a clear association between the leucosomes and melanosomes. Bands of disseminated sulfides commonly parallel the folded $D_{2g}$ architecture of the leucosomes and melanosomes. Sulfides are also locally intergrown with anorthite. Well-rounded pyrrhotite grains with chalcopyrite inclusions are commonly present along grain boundaries and cracks within garnet grains, although they also appear as inclusions within the garnet. One garnet grain contains rounded inclusions of biotite, of which one contains a subrounded grain of pyrrhotite (Fig. 20d). The composition of pyrrhotite in the majority of cases was nearly 2:1 Fe:S. Oxidation of sulfides will reduce the sulfur present in the sample; however, this ratio is still rather high.

# Geochronology

A total of 228 zircons from the four samples collectively yielded 234 U–Pb SHRIMP analyses results, of which 205 showed <5% discordance and were subsequently used for age interpretations by Wingate et al. (2015a,b,c,d). There are 105 detrital zircon ages that define significant age components (i.e. based on three or more analyses) ranging between 2981 and 2035 Ma (Table 6, Fig. 22). The majority of detrital zircon ages are between c. 2700 and 2500 Ma (Fig. 23). Sedimentary precursors to the migmatites are younger than 2035 ± 12 Ma, the conservative estimate for the maximum depositional age of sample GSWA 208325. Samples GSWA 208326, 208331 and 208344 yield older maximum depositional ages of 2527 ± 6, 2499 ± 13, and 2620 ± 6 Ma, respectively. The average age of high-grade metamorphism is 1991 ± 2 Ma (based on 100 analyses with a mean square weighted deviation of 1.8), determined from analyses of zircon rims or in crystals that are featureless in cathodoluminescence (CL) images.

**Table 6. Significant detrital zircon age components in four combined samples**

| *Age component (Ma)* | *Number of analyses* | *Age component (Ma)* | *Number of analyses* |
|---|---|---|---|
| 2035 | 3 | 2608 | 15 |
| 2307 | 3 | 2619 | 20 |
| 2394 | 3 | 2627 | 19 |
| 2496 | 8 | 2649 | 17 |
| 2503 | 7 | 2676 | 11 |
| 2518 | 9 | 2724 | 4 |
| 2529 | 10 | 2749 | 3 |
| 2555 | 9 | 2916 | 3 |
| 2584 | 14 | 2931 | 3 |
| 2599 | 15 | 2981 | 3 |

**NOTE**: a 'significant' age component is one with an age-probability contribution from three or more analyses

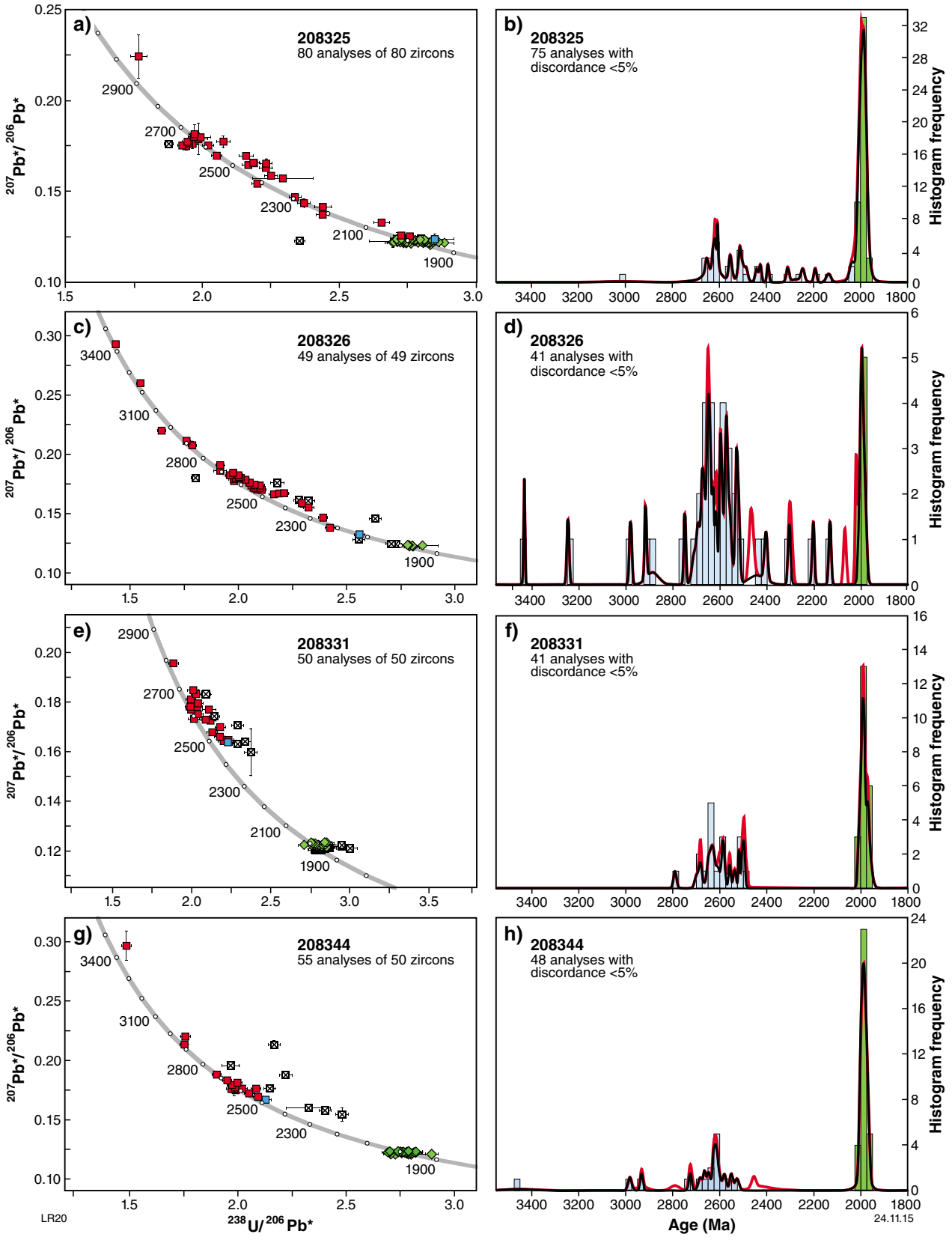


**Figure 22. U–Pb analytical data for zircons from four pelitic migmatite drillcore samples from the Glenburgh deposit (GSWA 208325, 208326, 208331 and 208344). In concordia diagrams (a, c, e, g), blue squares indicate the youngest detrital zircon; red squares indicate older detrital zircons; green diamonds indicate metamorphic zircons; black squares indicate analyses affected by radiogenic-Pb loss; and crossed squares indicate analyses with discordance >5%. In the probability density diagrams (b, d, f, h), the thick curve (black) and frequency histogram (blue bars, bin width 25 Ma) include only data with discordance <5%; the curve (red) includes all data. Green histogram bars indicate analyses of metamorphic zircons.**

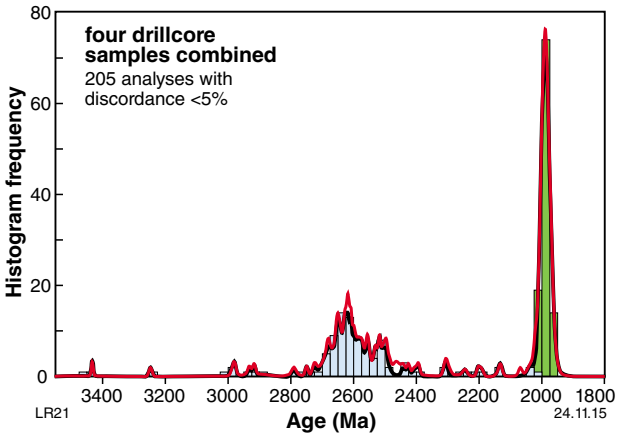


**Figure 23. Probability density diagram for combined zircon ages from four samples (GSWA 208325, 208326, 208331, 208344). The thick curve (black) and frequency histogram (blue bars, bin width 25 Ma) include only data with discordance <5% (*n* = 205); the curve (red) includes all data (*n* = 234). Green histogram bars indicate analyses of metamorphic zircons.**

# Discussion

## Age of gold mineralization

Gold mineralization hosted by amphibolite to granulite facies rocks is unlikely to coincide with the peak of metamorphism. Hydrothermal fluids are unable to pass through and react with these rocks due to the prevailing temperature and pressure conditions. Hydrothermal-fluid movement is particularly inhibited if the rocks have undergone partial melting during metamorphism, because the melt would absorb any such fluid phase (Loucks and Mavrogenes, 1999; Bastrakov et al., 2000; Tomkins and Grundy, 2009; Phillips and Powell, 2009).

Migmatites are compelling evidence of partial melting in high-grade metamorphic rocks. The presence of relatively coarse, euhedral, randomly orientated crystals in leucosomes indicates crystallization from at least a partially molten phase that was less influenced by solid-state deformation, in contrast to the aligned, subhedral to anhedral crystals seen in melanosomes, which would have dominantly grown by metamorphic recrystallization (Vernon and Collins, 1988; Tanner and Behrmann, 1997). The presence of garnet, orthopyroxene and cordierite within, or on the margins of, migmatitic leucosomes also supports melting in the absence of a hydrothermal fluid phase (Tomkins and Grundy, 2009). Migmatites with this combination of features are evident in the Glenburgh region, implying that partial melting of host rocks happened in the absence of a hydrothermal fluid during high-grade metamorphism. Therefore, gold could not have been introduced by a hydrothermal fluid at this time.

Elevated gold concentrations (>2 ppm) show no correlation with domains of postpeak metamorphic retrogression, alteration (including late-stage pyrite) or late veining and faulting, or low-temperature minerals. Therefore, mineralization has not been superimposed subsequent to regional prograde metamorphism. However, it can be difficult to demonstrate that gold mineralization occurred prior to the peak of prograde metamorphism, because original textures and mineral assemblages are invariably recrystallized or otherwise overprinted during the metamorphic event. Nevertheless, there are a number of relationships between gold, sulfides and host rocks that collectively provide a strong argument for mineralization at Glenburgh prior to peak metamorphism:

- Scanning electron microscopy and LA–ICP–MS results indicates that gold from the Glenburgh deposit is of high fineness (>98 wt% Au). High gold purity is atypical of primary hypogene gold, which commonly contains 5–20% Ag (Boyle, 1979; Hough et al., 2007), although near-pure hypogene gold can precipitate within tellurides (Shackleton et al., 2003) and stibnite (Nikolaeva, et al., 2004), which are not observed at Glenburgh.
- Gold fineness is commonly thought to increase by depletion of other elements, particularly silver, during postdepositional processes such as metamorphism, deformation or weathering by acidic fluids (Petrovskaya, 1973). Elevated temperatures can drive diffusion of silver and volatile elements such as Hg, Sb, Bi and As through gold crystal lattices to grain boundaries (Nikolaeva et al., 2004). Leaching by surface weathering seems unlikely, given that this sample (GSWA 214909) was collected from a depth of about 330 m below surface and there is no evidence of oxidation.
- Gold at Glenburgh contains trace Ag, Cu, Hg and Pd. No tellurium was detected. This signature is chemically significantly different to other gold deposits in the Capricorn Orogen, such as Gaffneys Find and Cobra (Fig. 24a,b; Hancock et al., 2009). Gaffneys Find and Cobra both contain higher trace element values of Cu, Hg, P and Sb, and significantly higher Ag. Neither Gaffneys Find nor Cobra is believed to have undergone metamorphism after deposition (Hancock et al., 2009).
- High-purity gold veinlets are observed between internal gold-grain boundaries (Fig. 18). These are interpreted to be locations where silver and other volatile components have been leached out during high-temperature metamorphism. Conditions during primary crystallization and intra- and post-ore transformations will dictate the internal structure of gold. Experiments have revealed that when gold is heated to 300–600°C, individual crystals comprising a grain begin to separate from one another (Petrovskaya, 1973). Silver is highly mobile and can easily diffuse from a Au–Ag solid solution during postdepositional events such as deformation, temperature elevation, or contact with aggressive solutions (Nikolaeva et al., 2004).

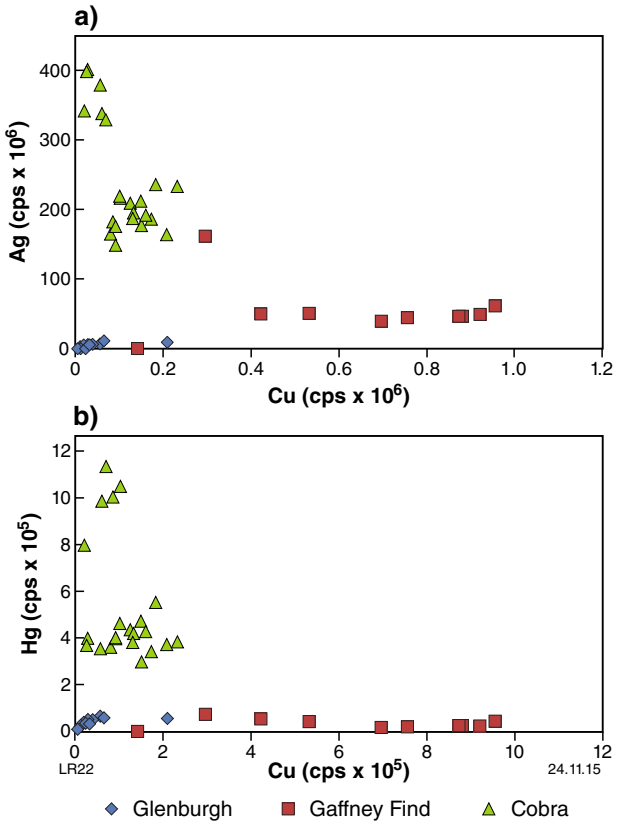


**Figure 24. LA–ICP–MS data for element content of Glenburgh deposit gold grains compared with LA–ICP–MS results for gold from the Gaffneys Find and Cobra deposits in the Ashburton area (detailed in Hancock et al., 2009): a) Ag versus Cu bivariate element plot. This shows the relatively low values of Ag and Cu in Glenburgh Au deposit compared to gold from Gaffneys Find and Cobra; b) Hg versus Cu bivariant plot, again showing the depleted nature of the Glenburgh deposit relative to Gaffneys Find and Cobra.**

- Nikolaeva (2004) argued that features of high-purity gold veinlets can indicate whether leaching has been by interaction with acidic fluids or temperature elevation. The veinlets found in a Glenburgh sample do not display corrosive rims, and are pronounced and highlighted by darker outer rims showing initial disintegration of subgrains (Fig. 21a). These features are more characteristic of veinlets formed during high-temperature metamorphism. Determining whether this gold is completely recrystallized is hampered by the small grain size and limited samples available for this study.

- The internal structure of the etched gold grain displays incoherent twinning (Fig. 21b). This type of grain structure is interpreted to have formed by thermal annealing at elevated temperatures and deformation of the gold grain (Hough et al., 2007).

- Pyrrhotite forms well-rounded inclusions within garnet and biotite, indicating the presence of a pre-peak metamorphic sulfide phase that recrystallized to reduce internal free energy by reducing the total surface area of grain boundaries, as it was engulfed by other prograde metamorphic minerals (Vernon, 1976; Poirier, 1985). This textural relationship also exists at the granulite-hosted Challenger and Griffins Find gold deposits, which are interpreted to be metamorphosed deposits (Tomkins et al., 2004a; Tomkins and Grundy, 2009).

- Pyrrhotite is the most abundant sulfide observed. The abundant pyrrhotite is believed to have formed by sulfidation of the host rock contemporaneously with gold mineralization. A possible explanation for the observed decoupled gold and sulfide distribution could be that gold, originally in solid solution with pyrite, was partly liberated and mobilized into a free phase during metamorphic desulfidation and conversion of pyrite to pyrrhotite.

- Hyperspectral scanning has been particularly useful for mapping differences in dark, fine-grained units, using compositional variations in white mica (muscovite and paragonite), dark mica (biotite and phlogopite) and amphiboles. At the Glenburgh deposit there is no apparent relationship between any specific mica composition and gold mineralization, although there does seem to be an abundance of dark micas (biotite and phlogopite), and a corresponding lack of garnet (almandine), pyroxenes and cordierite, in the general region of high gold grades (Fig. 13). Any alteration that may be associated with gold mineralization is extremely cryptic and requires further multi-element assay and petrographic investigation, or else is non-existent. Changes in muscovite–paragonite and biotite–phlogopite compositions are commonly taken as indicative of alteration (e.g. Tropicana gold deposit; Blenkinsop and Doyle, 2014).

- The presence of almandine and cordierite in the leucosomes and melanosomes suggests an argillaceous sedimentary rather than granitic protolith (Brown and Korhonen, 2009) for the host rocks of the Glenburgh deposit.

The combination of the above characteristics of gold mineralization at the Glenburgh deposit suggests that mineralization must have occurred before the peak of metamorphism and — logically — after deposition of the sedimentary protoliths to the host rocks. The youngest detrital zircons in pelitic migmatite from the Zone 126 lode provide a maximum depositional age of 2035 ± 12 Ma (Wingate et al., 2015b). The same rocks contain zircons interpreted to have grown during high-grade metamorphism at 1991 ± 2 Ma (Wingate et al., 2015a–d). These results are similar to the maximum depositional and metamorphic ages of 2083 ± 7 Ma and 1997 ± 7 Ma, respectively, obtained from a sample of pelitic diatexite collected about two kilometres to the southwest of the deposit trend, near Paradise Well (GSWA 185942; Wingate et al., 2010, Johnson et al., 2010; Johnson et al., 2011c). Therefore, the absolute age of gold mineralization, including uncertainties, is constrained to a window of about 58 million years between 2047 Ma and 1989 Ma.

## Original style of gold mineralization

McFarlane et al. (2007) noted that it is commonly difficult to determine the original style of a metamorphosed gold deposit, because prograde metamorphism and associated deformation can significantly transform and obscure primary textures and mineral assemblages by:

- converting typically fine-grained, hydrous alteration assemblages into coarse-grained, anhydrous assemblages
- modifying the bulk composition of protoliths by extracting components, including potentially diagnostic accessory minerals, into partial melts
- physically rearranging the geometry of the primary deposit structure and alteration zones.

Clues to the original mineralization style might be derived from a consideration of the tectonic setting in which mineralization took place, and from a comparison with the features of other metamorphosed gold deposits that have an inferred primary style.

The rock units hosting gold mineralization were probably sedimentary in origin and dominantly pelitic, although little can be deduced from their present form regarding their depositional setting. The metagranitic rocks of the 2005–1970 Ma Dalgaringa Supersuite intruded this metasedimentary package along the southern margin of the Glenburgh Terrane during the peak of metamorphism ($D_{1g}/M_{1g}$) in the earliest stages of the Glenburgh Orogeny (Fig. 2). The Dalgaringa Suite has whole-rock major- and trace-element, and Nd isotopic signatures consistent with formation in a supra-subduction, Archean continental-margin, arc setting (Occhipinti et al., 2004; Sheppard et al., 2004). Present-day continental-arc settings are favourable for porphyry Cu–Mo–Au, epithermal Au, polymetallic (Sn, W) skarn and orogenic Au mineralization. If the host rocks at Glenburgh were deposited in a back-arc basin, the gold mineralization may be 'orogenic' in style, forming during basin inversion and greenschist- to lower amphibolite-facies metamorphism accompanying the early stages of the Glenburgh Orogeny. It might also have been a porphyry Cu–Au deposit, although copper abundance is low in the system.

The Glenburgh deposit shows similarities with other, extensively studied gold deposits in high-grade metamorphic rocks, particularly those at Challenger and Griffins Find (Fig. 25; Tomkins and Mavrogenes, 2002; Tomkins and Grundy, 2009). The Challenger deposit is surrounded by Archean pelitic migmatites in the northwest Gawler Craton, South Australia. Gold is associated with, and forms as inclusions in, löllingite and arsenopyrite, predominantly within leucosomes in a shoot in the hinge zone of a fold. Mineralization is interpreted to have been mobilized into the silicate melt during peak granulite-facies metamorphism and partial melting of the parent rock at 800–850°C and about 7.5 ± 1.5 kbars (Tomkins and Mavrogenes, 2002). McFarlane et al. (2007) were able to recognize pre-metamorphic hydrothermal alteration using textural, mineralogical and lithogeochemical criteria by factoring in the effects of partial melting and mass changes during peak metamorphism. They found a 50 m-wide halo surrounding Au mineralization, characterized by losses of Si, Na, Ca and Sr, and increases in Al, K, Fe and Mg relative to the composition of the unaltered distal gneisses. McFarlane et al. (2007) concluded that these characteristics are consistent with quartz–sericite or quartz–alunite alteration in the Au-rich domains and feldspar-destruction and chloritization of proximal host rocks, prior to prograde metamorphism. They suggested a high-sulfidation epithermal style for the gold deposit rather than orogenic, based on the broad alteration halo, the primary alteration mineralogy, and the interpreted setting in a back-arc basin proximal to an active volcanic arc.

The Griffins Find deposit is in the southwestern Yilgarn Craton, in a greenstone belt metamorphosed to granulite facies. Gold is associated with, and forms as inclusions in, löllingite–arsenopyrite–pyrrhotite. The silicate host rocks are depleted in Fe and enriched relatively in Al and Mg. Quartz–calcite assemblages are commonly preserved within the deposit. Tomkins and Grundy (2009) documented sulfides as rounded inclusions in metamorphic minerals. Mineralogical features of the migmatites implied vapour-absent melting. The presence of rounded sulfide inclusions in metamorphic minerals indicated that sulfides existed prior to peak granulite-facies metamorphism. Tomkins and Grundy (2009) believe that pyrite and arsenopyrite formed at greenschist-facies conditions by sulfidation of Fe-bearing silicates (a process suggested by Goldfarb et al., 2005), thereby depleting the silicate bulk composition in Fe. Progression to amphibolite facies metamorphism converted pyrite and arsenopyrite to pyrrhotite and löllingite, liberating sulfur (Toulmin and Barton, 1964; Kretschmar and Scott, 1976), which then combined with silicate Fe to form new pyrrhotite and further deplete silicate host rocks in Fe, and relatively enrich them in Al and Mg. Quartz–calcite assemblages would not be preserved if hydrothermal fluids were introduced at temperatures above 750°C, inferring an original silica–carbonate alteration by a $H_2O$–$CO_2$ fluid, typical of an orogenic gold system formed at greenschist- or lower amphibolite-facies conditions (Goldfarb et al., 2005).

Several similarities can be drawn between pre-peak metamorphic mineralization at the Glenburgh, Griffins Find and Challenger deposits. Each deposit has similar host-rock mineralogy dominated by quartz–feldspar–biotite–garnet–cordierite–pyrrhotite assemblages. Gold at the Challenger deposit was mobilized into leucosomes during metamorphism of a pre-existing deposit, whereas gold at the Griffins Find deposit is distributed between garnet–biotite gneiss, mafic granulite, sillimanite–cordierite gneiss and microcline-rich gneiss. A distinction between the Griffins Find – Challenger deposits and the Glenburgh deposit is the lack of arsenic within the latter. Both the Challenger and Griffins Find deposits have significant amounts of löllingite and arsenopyrite associated with both free and lattice-hosted gold.

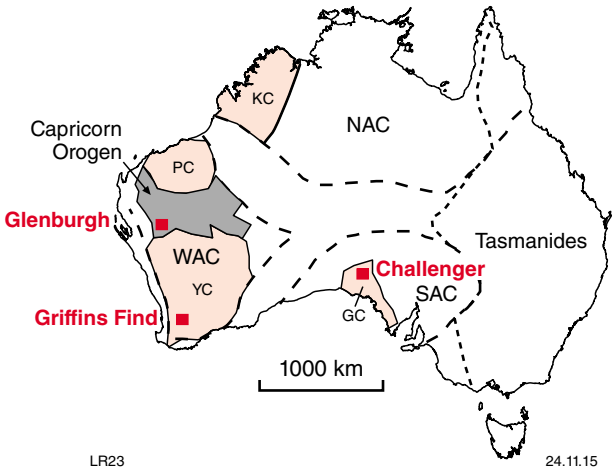


**Figure 25. Location map for the Glenburgh, Griffins Find and Challenger Au deposits relevant to cratons (refer to Fig. 1 for abbreviations)**

Glenburgh would appear to be more analogous to the Griffins Find deposit than Challenger in having a poorer correlation between mineralization and rock type, and a potentially similar alteration signature (to be discussed below).

Silica–carbonate or potassic alteration are both common in orogenic Au deposits (Groves, 1993; Goldfarb et al., 2005). Gold associated with a calcic amphibole at the Glenburgh deposit could be an indication of metamorphosed carbonate alteration. The K anomaly in radiometric data (Fig. 11) may represent a potassic alteration halo, although sulfidation might also cause a shift to more potassic compositions, as suggested by Tomkins and Grundy (2009) for the Griffins Find deposit.

The observed mineralogical, lithogeochemical features and interpreted tectonic setting of mineralization at the Glenburgh deposit suggest an orogenic gold deposit style. However, further detailed studies are needed to properly investigate whether there is cryptic alteration, which would include a close examination of multi-element assay data to determine if there are systematic enrichment or depletion patterns in Ca, K, Fe and Mg contents within and beyond mineralization.

## Gold-exploration vectors and regional prospectivity

Geologists at Helix Resources determined early in their exploration campaign that the only obvious chemical pathfinder to Au at the Glenburgh deposit was Au itself. Therefore, multi-element assay data were not collected during the majority of drilling campaigns (Savcin, 2004), with the result that, if gold lodes were not exposed in outcrop, a deposit may have been overlooked. Furthermore, gold assays greater than one gram per tonne have been returned from gneissic banding dominated by biotite–quartz–feldspar–garnet gneiss, amphibolite gneiss containing tschermakite and, in one observed case, within quartz–chlorite veining, meaning that no specific lithology can be targeted for mineralization.

The presence of an identifiable alteration halo around gold mineralization would provide an important, greatly expanded exploration footprint. When dealing with metamorphosed (hydrothermal) mineral deposits, it is important to understand low-temperature fluid–rock interaction, and the likely mineralogical and textural evolution of the hydrothermal assemblages during prograde metamorphism in order to be able to recognize pre-metamorphic hydrothermal alteration (McFarlane et al., 2007). Nevertheless, such alteration, if it exists, should be visible if it was distinct from the original host rock, even if it has been metamorphosed.

Visual and hyperspectral logging of the Glenburgh deposit drillcore and chips did not reveal any obvious alteration pattern associated with zones of gold mineralization. It may be that there is simply no alteration to see. Alternatively, it may be that the drilling did not extend beyond any potentially widespread alteration halo and high-grade metamorphism may also have rendered cryptic any alteration assemblage, so that it is now manifested in whole-rock or mineral chemistry for which there are presently few data to review.

This study of the Glenburgh deposit has identified a few potential gold-exploration vectors for further evaluation. The intergrowth of anorthite with sulfides, and the local association of tschermakite with gold (GSWA 214909), could be an indication of a pre-peak metamorphic carbonate alteration associated with gold mineralization, or alternatively that a calcium-rich sediment was present in the region before metamorphism. Given the small sample set of visible gold to analyse, and the difficulty of identifying tschermakite in HyLogger data for comparison against gold assays, it has not been unequivocally demonstrated that tschermakite is always proximal to gold, and this should be further tested.

The area of high-potassium evident in radiometric data immediately south of the Glenburgh mineralization trend (Fig. 11) could be a surface expression of the alteration associated with gold mineralization — if mineralization was related to a potassic hydrothermal fluid. Potassium enrichment within this region is suggested by the abundance of microcline, biotite, phlogopite and muscovite in samples collected from outcropping gneiss, metagranite and metapegmatite. Biotite, phlogopite and muscovite are abundant within drilling samples, although there is a distinct lack of microcline and intrusive granitic rocks associated with mineralization, and further studies are required to determine whether the potassium anomaly is related to alteration and mineralization or to differences in protolith or extent of outcrop.

Lastly, the marked difference in magnetic susceptibility of the Glenburgh host rocks (Fig. 8) could be associated with an alteration feature. It is possible that during sulfidation, Fe is sequestered to form sulfides (pyrrhotite) and thus creates an iron-deficient anomaly within the exposed silicate rocks and a relative enrichment in Mg and Al.

Alternatively, the difference in magnetic susceptibility represents a change from magnetite to hematite.

There could be at least three potential pathfinders to mineralization, including:

- calcium abundance (due to the presence of calcium-rich tschermakite and anorthite associated with gold and sulfides)
- potassium abundance (visible in radiometric data due to the abundance of micas and microcline)
- a reduction in magnetic susceptibility of the host rocks relative to the surrounding area (hematite and magnetite relationship, or a change in Fe distribution).

The true gold endowment of the Glenburgh Terrane may be underappreciated if alteration is cryptic, because big hydrothermal footprints have not been identified. This research was not extensive enough to clearly identify robust pathfinders to the Glenburgh system, although has hinted at some possible fruitful avenues for further work.

# Conclusion

The Glenburgh gold mineralization has been shown to have formed within a package of metasedimentary rocks before the peak of high-grade metamorphism during the 2005–1950 Ma Glenburgh Orogeny. The presence of rounded sulfide inclusions within peak metamorphic garnet porphyroblasts, illustrates that mineralization predates garnet crystallization. Incoherent twins, intergranular high-purity gold bands and low trace element inclusions within the gold grains provide evidence for thermal annealing and silver leaching of the gold. The lack of any typical alteration assemblage or association with a specific lithology suggests the alteration assemblage and mineralization were recrystallized and perhaps remobilized during high-grade metamorphism and deformation. Three potential pathfinders to mineralization have been identified: calcium abundance, potassium abundance and lower magnetic susceptibility.

Dating of detrital zircon grains to obtain the maximum depositional age from pelitic migmatite provided an upper constraint for mineralization at 2035 + 12 Ma. Including the uncertainties, this provides a window for mineralization of about 58 million years between 2047 and 1989 Ma.

The Gascoyne Province and Capricorn Orogen have few working gold mines; however, it is now known that the beginning of the Glenburgh Orogeny was associated with significant gold mineralization. The true endowment of the Glenburgh Terrane is poorly understood, and perhaps underappreciated, because alteration is cryptic, making the detection of large, hydrothermal footprints difficult. Further work on the Glenburgh deposit should focus on determining the effects of metamorphism on the alteration assemblage and delineation of pathfinder elements in, and adjacent to, the Glenburgh deposit. This could lead to more successful targeting for similar deposits in the surrounding Glenburgh Terrane, particularly in the Dalgaringa Arc region.

# Acknowledgements

This Report is derived from research undertaken as part of a Master of Ore Deposit Geology supported by GSWA and completed through The University of Western Australia. I thank Gascoyne Resources, particularly Mike Dunbar and Julian Goldsworthy, for agreeing to participate in the collaborative research, and for providing sample material and logistical support. I thank Michael Verrall (CSIRO) for assisting with SEM analyses, Ralph Bottrill (Mineral Resources Tasmania) for XRD analysis, and Cameron Scadding (TSW Analytics) for the LA–ICP–MS analysis.

# References

Aitken, ARA, Joly, A, Dentith, MC, Johnson, SP, Thorne, AM and Tyler, IM 2014, 3D architecture, structural evolution, and mineral prospectivity of the Gascoyne Province: Geological Survey of Western Australia, Report 123, 94p.

Bastrakov, E, Cassidy, KF and Shvarov, YV 2000, Gold transport at Archaean lode gold deposits: gold solubility along the rock-buffered pathways, *in* Geological Society of Australia Abstracts: Geological Society of Australia; 15th Australian Geological Convention, Sydney, Australia, 3 July 2000, p. 25.

Blenkinsop, TG and Doyle, MG 2014, Structural controls on gold mineralization on the margin of the Yilgarn craton, Albany-Fraser orogen: The Tropicana deposit, Western Australia: Journal of Structural Geology, v. 67, p. 189–204.

Bottrill, RS and Woolley, RN 2014, XRD Analyses: Glenburgh gold deposit, WA: Mineral Resources Tasmania, Hobart, Tasmania, 11p. (unpublished).

Boyle, RW 1979, The geochemistry of gold and its deposits: Canadian Geological Survey Bulletin, v. 280, p. 584.

Brown, M and Korhonen, FJ 2009, Some remarks on melting and extreme metamorphism of crustal rocks, *in* Physics and Chemistry of the Earth's Interior *edited by* AK Gupta and S Dasgupta: Springer, New York, p. 67–87.

Cawood, PA and Tyler, IM 2004, Assembling and reactivating the Proterozoic Capricorn Orogen: lithotectonic elements, orogenies, and significance: Precambrian Research, v. 128, p. 201–218.

Chown, EH, Hicks, J, Phillips, GN and Townend, R 1984, The disseminated Archaean Big Bell gold deposit, Murchison Province, Western Australia; an example of premetamorphic hydrothermal alteration *edited by* RP Foster: Gold '82; The Geology, Geochemistry and Genesis of Gold Deposits, p. 305–324.

Colvine, AC, Andrews, AJ, Cherry, ME, Durocher, ME, Fyon, JA, Lavigne, MJ, Macdonald, AJ, Marmont, S, Poulsen, KH, Springer, JS and Troop, DG 1984, An integrated model for the origin of Archean lode gold deposits: Ontario Geological Survey, Report 5524, 98p.

Doyle, MG, Blenkinsop, TG, Crawford, AJ, Fletcher, IR, Foster, J, Fox-Wallace, LJ, Large, RR, Mather, R, McNaughton, NJ, Meffre, S, Muhling, JR, Occhipinti, SA, Rasmussen, B and Savage, J 2014, Tropicana deposit, Western Australia: an integrated approach to understanding granulite-hosted gold and the Tropicana Gneiss, *in* Albany–Fraser Orogen seismic and magnetotelluric (MT) workshop 2014: extended abstracts: Geological Survey of Western Australia, Perth, Western Australia, Record 2014/6, p. 69–76.

Doyle, MG, Savage, J, Blenkinsop, TG, Crawford, A and McNaughton, NJ 2013, Tropicana – Unravelling the complexity of a +6 million ounce gold deposit hosted in granulite facies metamorphic rocks: The Australasian Institute of Mining and Metallurgy; World Gold 2013, p. 87–94.

Frost, R, Mavrogenes, JA and Tomkins, AG 2002, Partial melting of sulfide ore deposits during medium- and high-grade metamorphism: The Canadian Mineralogist, v. 40, p. 1–18.

Gascoyne Resources 2014, High grade domains identified within updated Glenburgh gold mineral resource: Report to Australian Stock Exchange, 24 July 2014, 24p.

Goldfarb, RJ, Baker, T, Dube, B, Groves, DI, Hart, CJR and Gosselin, P 2005, Distribution, character, and genesis of gold deposits in metamorphic terranes: Economic Geology, v. 100, p. 407–450.

Groves, DI 1993, The crustal continuum model for late-Archaean lode-gold deposits of the Yilgarn Block, Western Australia: Mineralium Deposita, v. 28, no. 6, p. 366–374.

Groves, DI, Barley, ME, Barnicoat, AC, Cassidy, KF, Fare, RJ, Hagemann, SG, Ho, SE, Hronsky, JMA, Mikucki, EJ, Mueller, AG, McNaughton, NJ, Perring, CS, Ridley, JR and Vearncombe, JR 1992, Lode gold deposits of the Yilgarn Craton; a depositional continuum from deep sourced hydrothermal fluids in crustal scale plumbing systems, *in* The Archeaen; terrains, processes and metallogeny *edited by* JE Glover and SE Ho: Geology Department and Extension, University of Western Australia 20, p. 325–337.

Groves, DI, Goldfarb, RJ, Gebre-Mariam, M, Hagemann, SG and Robert, F 1998, Orogenic gold deposits: a proposed classification in the context of their crustal distribution and relationship to other gold deposit types: Ore Geology Reviews, v. 13, no. 1–5, p. 7–27.

Hancock, EA, Green, AA, Huntington, JF, Schodlok, MC and Whitbourn, LB 2013, HyLogger-3: Implications of adding thermal-infrared sensing: Geological Survey of Western Australia, Record 2013/3, 24p.

Hancock, EA and Huntington, JF 2010, The GSWA NVCL HyLogger: rapid mineralogical analysis for characterizing mineral and petroleum core: Geological Survey of Western Australia, Record 2010/17, 21p.

Hancock, EA, Thorne, AM, Morris, PA, Watling, RJ and Cutten, HNC 2009, Mineralogy and trace element chemistry of lode and alluvial gold from the western Capricorn Orogen: Geological Survey of Western Australia, Record 2009/6, 29p.

Hawke, ML, Meffre, S, Stein, H, Hilliard, P, Large, R and Gemmell, JB 2015, Geochronology of the DeGrussa volcanic-hosted massive sulphide deposit and associated mineralisation of the Yerrida, Bryah and Padbury Basins, Western Australia: Precambrian Research, v. 267, p. 250–284.

Hough, RM, Butt, CRM, Reddy, SM and Verrall, M 2007, Gold nuggets: supergene or hypogene?: Australian Journal of Earth Sciences, v. 54, p. 959–964.

Johnson, SP 2013, The birth of supercontinents and the Proterozoic assembly of Western Australia: Geological Survey of Western Australia, Perth, Western Australia, 78p.

Johnson, SP, Cutten, HN, Tyler, IM, Korsch, RJ, Thorne, AM, Blay, OA, Kennett, BLN, Blewett, RS, Joly, A, Dentith, MC, Aitken, ARA, Goodwin, JA, Salmon, M, Reading, A, Boren, G, Ross, J, Costelloe, RD and Fomin, T 2011a, Preliminary interpretation of deep seismic reflection lines 10GA–CP2 and 10GA–CP3: crustal architecture of the Gascoyne Province, and Edmund and Collier Basins, *in* Capricorn Orogen seismic and magnetotelluric (MT) workshop 2011: extended abstracts *edited by* SP Johnson, AM Thorne and IM Tyler: Geological Survey of Western Australia, Record 2011/25, p. 49–60.

Johnson, SP, Sheppard, S, Rasmussen, B, Wingate, MTD, Kirkland, CL, Muhling, JR, Fletcher, IR and Belousova, E 2010, The Glenburgh Orogeny as a record of Paleoproterozoic continent–continent collision: Geological Survey of Western Australia, Record 2010/5, 54p.

Johnson, SP, Sheppard, S, Rasmussen, B, Wingate, MTD, Kirkland, CL, Muhling, JR, Fletcher, IR and Belousova, EA 2011b, Two collisions, two sutures: punctuated pre-1950 Ma assembly of the West Australian Craton during the Ophthalmian and Glenburgh Orogenies: Precambrian Research, v. 189, no. 3–4, p. 239–262, doi: 10.1016/j.precamres.2011.07.011.

Johnson, SP, Sheppard, S, Wingate, MTD, Kirkland, CL and Belousova, EA 2011c, Temporal and hafnium isotopic evolution of the Glenburgh Terrane basement: an exotic crustal fragment in the Capricorn Orogen: Geological Survey of Western Australia, Report 110, 27p.

Johnson, SP, Thorne, AM, Tyler, IM, Korsch, RJ, Kennett, BLN, Cutten, HN, Goodwin, J, Blay, OA, Blewett, RS, Joly, A, Dentith, MC, Aitken, ARA, Holzschuh, J, Salmon, M, Reading, A, Heinson, G, Boren, G, Ross, J, Costelloe, RD and Fomin, T 2013, Crustal architecture of the Capricorn Orogen, Western Australia and associated metallogeny: Australian Journal of Earth Sciences, v. 60, no. 6–7, p. 681–705, doi:10.1080/08120099.2013.826735.

Kisters, AFM, Kolb, J and Meyer, FM 1998, Gold mineralization in high grade metamorphic shear zones of the Renco Mine, southern Zimbabwe: Economic Geology, v. 98, p. 587–601.

Kolb, J, Dziggel, A and Bagas, L 2015, Hypozonal lode gold deposits: a genetic concept based on a review of the New Consort, Renco, Hutti, Hira Buddini, Navachab, Nevoria and The Granites deposits: Precambrian Research, v. 262, p. 20–44.

Kretschmar, U and Scott, SD 1976, Phase relations involving arsenopyrite in the system Fe-As-S and their application: Canadian Mineralogist, v. 14, p. 364–386.

Loucks, RR and Mavrogenes, JA 1999, Gold solubility in supercritical hydrothermal brines measured in synthetic fluid inclusion: Science, v. 284, p. 2159–2163.

Martin, DM and Morris, PA 2010, Tectonic setting and regional implications of ca 2.2 Ga mafic magmatism in the southern Hamersley Province, Western Australia: Australian Journal of Earth Sciences, v. 57, no. 7, p. 911–931.

McFarlane, CR, Mavrogenes, JA and Tomkins, AG 2007, Recognizing hydrothermal alteration through a granulite facies metamorphic overprint at the Challenger Au deposit, South Australia: Chemical Geology, v. 243, no. 1–2, p. 64–89.

Nikolaeva, LA, Gavrilov, AM, Nekrasova, AN, Yablokova, SV and Shatilova, LV 2004, Native gold in lode and placer deposits of Russia, Atlas: TsNIGRI, Moscow.

Occhipinti, SA, Sheppard, S, Passchier, C, Tyler, IM and Nelson, DR 2004, Palaeoproterozoic crustal accretion and collision in the southern Capricorn Orogen: the Glenburgh Orogeny: Precambrian Research, v. 128, p. 237–255.

Overton, N 2000, Summary report on exploration for period 1994 to 2000 (Project Glenburgh); Helix Resources NL and Eagle Mining Pty Ltd: Geological Survey of Western Australia, Statutory mineral exploration report, A62826 (open file).

Pearson, JM, Taylor, WR and Barley, ME 1996, Geology of the alkaline Gifford Creek Complex, Gascoyne Complex, Western Australia: Australian Journal of Earth Sciences, v. 43, no. 3, p. 299–309.

Petrovskaya, NV 1973, Native Gold: Nauka, Moscow, Russia, p. 347.

Phillips, GN 1985, Interpretations of Big Bell/Hemlo-type gold deposits: Precursors, metamorphism, melting and genetic constraints: Transactions of the Geological Society of South Africa, v. 88, p. 159–173.

Phillips, GN and Powell, R 2009, Formation of gold deposits: Review and evaluation of the continuum model: Earth-Science Reviews, v. 94, no. 1–4, p. 1–21.

Pirajno, F 2004, Metallogeny in the Capricorn Orogen, Western Australia: Precambrian Research, v. 128, p. 411–439.

Pirajno, F and Gonzalez-Alvarez, I 2014, The ironstone veins of the Gifford Creek ferrocarbonatite complex, Gascoyne Province: Geological Survey of Western Australia, Record 2013/12, 19p.

Pirajno, F, Thorne, AM, Mernagh, TP, Creaser, RA, Hell, A and Cutten, H 2010, The Abra deposit: a polymetallic mineral system in the Edmund Basin, Capricorn Orogen, Western Australia, *in* 13th Quadrennial IAGOD Symposium Proceedings *edited by* NJ Cook and Others: International Association on Genesis of Ore Deposits (IAGOD); Giant Ore Deposits Down-Under, Adelaide, South Australia, 6 April 2010, p. 112–114.

Poirier, J-P 1985, Creep of crystals: high-temperature deformation processes in metals, ceramics and minerals: Cambridge University Press, Cambridge, UK, 260p.

Pontual, S 2008, GMEX spectral analysis guides for mineral exploration (3rd edition): AusSpec International Ltd, 10 vols.

Rasmussen, B, Fletcher, IR and Sheppard, S 2005, Isotopic dating of the migration of a low-grade metamorphic front during orogenesis: Geology, v. 33, p. 773–776.

Savcin, S 2004, Annual report for period 28/04/03-27/04/04 - Glenburgh Tenement E09/644; Helix Resources: Geological Survey of Western Australia, Statutory mineral exploration report, A68722 (open file) 72p.

Shackleton, JM, Spry, PG and Bateman, R 2003, Telluride mineralogy of the Golden Mile deposit, Kalgoorlie, Western Australia: Canadian Mineralogist, v. 41, p. 1503–1524.

Sheppard, S, Bodorkos, S, Johnson, SP, Wingate, MTD and Kirkland, CL 2010, The Paleoproterozoic Capricorn Orogeny: intracontinental reworking not continent-continent collision: Geological Survey of Western Australia, Report 108, 33p.

Sheppard, S, Occhipinti, SA and Tyler, IM 2004, A 2005-1970 Ma Andean-type batholith in the southern Gascoyne Complex, Western Australia: Precambrian Research, v. 128, no. 3–4, p. 257–277.

Tanner, DC and Behrmann, JH 1997, Study of strain and partial-melt transfer in a banded migmatite: Journal of Structural Geology, v. 19, p. 1405–1417.

Tomkins, AG 2010, Windows of metamorphic sulfur liberation in the crust: Implications for gold deposit genesis: Geochimica et Cosmochimica Acta, v. 74, no. 11, p. 3246–3259.

Tomkins, AG, Dunlap, WJ and Mavrogenes, JA 2004a, Geochronological constraints on the polymetamorphic evolution of the granulite-hosted Challenger gold deposit: Implications for assembly of the northwest Gawler Craton: Australian Journal of Earth Sciences, v. 51, no. 1, p. 1–14.

Tomkins, AG and Grundy, C 2009, Upper temperature limits of orogenic gold deposit formation: Constraints from the granulite-hosted Griffin's Find deposit, Yilgarn Craton: Economic Geology, v. 104, no. 5, p. 669–685.

Tomkins, AG and Mavrogenes, JA 2002, Mobilization of gold as a polymetallic melt during pelite anatexis at the Challenger Deposit, South Australia: A metamorphosed Archaean gold deposit: Economic Geology, v. 97, p. 1249–1271.

Tomkins, AG, Pattison, DRM and Zaleski, E 2004b, The Hemlo gold deposit, Ontario: an example of melting and mobilization of a precious metal-sulfosalt assemblage during amphibolite facies metamorphism and deformation: Economic Geology, v. 99, no. 6, p. 1063–1084.

Toulmin, PI and Barton, J 1964, A thermodynamic study of pyrite and pyrrhotite: Geochimica et Cosmochimica Acta, v. 56, p. 227–243.

Vernon, RH 1976, Metamorphic processes: reactions and microstructure development: Allen and Unwin, London, 247p.

Vernon, RH and Collins, WJ 1988, Igneous microstructures in migmatites: Geology, v. 16, p. 1126–1129.

White, R and Powell, R 2002, Melt loss and preservation of granulite facies mineral assemblages: Journal of Metamorphic Geology, v. 20, p. 621–632.

Wingate, M and Kirkland, C 2014, Introduction to geochronology information released in 2014: Geological Survey of Western Australia, Record, 5p.

Wingate, MTD, Kirkland, CL, Johnson, SP and Sheppard, S 2010, 185942: pelitic diatexite, Paradise Well; Geochronology Record 861: Geological Survey of Western Australia, 5p.

Wingate, MTD, Kirkland, CL, Korhonen, FJ, Roche, LK and Johnson, SP 2015a, 208344: semipelitic gneiss, Glenburgh deposit; Geochronology Record 1246: Geological Survey of Western Australia, 6p.

Wingate, MTD, Kirkland, CL, Korhonen, FJ and Johnson, SP 2015b, 208325: pelitic migmatite, Glenburgh deposit; Geochronology Record 1236: Geological Survey of Western Australia, 6p.

Wingate, MTD, Kirkland, CL, Korhonen, FJ and Johnson, SP 2015c, 208326: pelitic migmatite, Glenburgh deposit; Geochronology Record 1237: Geological Survey of Western Australia, 6p.

Wingate, MTD, Kirkland, CL, Korhonen, FJ and Johnson, SP 2015d, 208331: pelitic migmatite, Glenburgh deposit; Geochronology Record 1238: Geological Survey of Western Australia, 6p.

# Appendix 1

# Field and drillhole sample location and descriptions

**Table 1.1a. Field sample locations**

| *GSWA number* | *MGA easting* | *MGA northing* | *Zone* | *Field description* | *Petrography* |
|---|---|---|---|---|---|
| 214926 | 414012 | 7191949 | 50 | Migmatitic gneiss | Coarse-grained plagioclase, microcline, quartz, minor biotite |
| 214927 | 413770 | 7192088 | 50 | Psammitic schist intruded by pegmatite | Banded amphiboles, quartz, plagioclase |
| 214928 | 413770 | 7192088 | 50 | Pegmatite intruding psammitic schist | Biotite, quartz, microcline, plagioclase |
| 214929 | 414334 | 7192050 | 50 | Migmatitic gneiss with pegmatite and psammitic lenses | Fine-grained quartz, plagioclase, microcline |
| 214930 | 414692 | 7192003 | 50 | Migmatite | Large (~1cm) garnet, biotite, quartz, plagioclase |
| 214931 | 413758 | 7193320 | 50 | Biotite with feldspar and quartz clots | Biotite, quartz, plagioclase |
| 214932 | 413872 | 7193079 | 50 | Leucosome | Fine-grained quartz, plagioclase, microline, minor biotite |
| 214933 | 414187 | 7192976 | 50 | Amphibolite | Plagioclase, weathered amphibole |
| 214934 | 413761 | 7192747 | 50 | Granite | Microcline, quartz |
| 214935 | 414318 | 7193365 | 50 | Mafic schist intruded by granite | Coarse-grained quartz veins throughout fine-grained quartz, plagioclase, microcline, minor biotite and hornblende |
| 214936 | 414313 | 7193243 | 50 | Garnet-bearing migmatite | Garnet, biotite, quartz |
| 214937 | 414687 | 7193580 | 50 | Migmatitic gneiss with amphibolite lenses | Hornblende, plagioclase, quartz; fine-grained hornblende, ilmenite |
| 214938 | 414960 | 7193742 | 50 | Migmatite | Garnet, quartz, plagioclase, with fine-grained clots of biotite, quartz |
| 214939 | 414687 | 7194255 | 50 | Gneissic amphibolite(?) | Coarse-grained quartz, plagioclase with clots of hornblende, pyroxene |
| 214940 | 414579 | 7193999 | 50 | Pegmatite with biotite clots forming a lineation | Fine-grained quartz with coarse-grained microcline |
| 214941 | 414579 | 7193999 | 50 | Migmatite | Fine-grained bands of biotite with fine- and coarse-grained interbands of quartz and minor microcline and plagioclase |
| 214942 | 414065 | 7194288 | 50 | Ferruginous sandstone | Quartz matrix, muscovite, corderite and small clots of fine-grained plagioclase |
| 214943 | 414065 | 7194288 | 50 | Ferruginous sandstone | Magnetite overprinting a coarse-grained quartz matrix |

**Table 1.1b. Drillcore samples**

| *GSWA sample number* | *Drillhole number* | *Depth (m)* | *Logging description* | *Petrographic results* |
|---|---|---|---|---|
| 214901 | GBD011 | 182.3 | Quartz garnet biotite gneiss | Pyrrhotite and biotite inclusions in garnet. Quartz, garnet, cordierite leucosomes |
| 214902 | GBD011 | 199.05 | Amphibolite | Hornblende, orthopyroxene, plagioclase and minor pyrrhotite and chalcopyrite |
| 214903 | GBD011 | 241.1 | Quartz biotite garnet gneiss | Quartz, microcline, plagioclase with minor biotite bands throughout |
| 214904 | GBD011 | 252.06 | Quartz biotite gneiss with multiple sulfide inclusions | Large pyrrhotite grain with chalcopyrite inclusions and pyrite rimming the pyrrhotite. Quartz groundmass |
| 214905 | GBD011 | 267.9 | Contact between amphibolite and quartz biotite gneiss | Transition from predominantly quartz, plagioclase, garnet to garnet quartz biotite to fine-grained biotite. Trace sulfides (pyrrhotite) predominantly along the contact |
| 214906 | GBD011 | 331.4 | Sulfides within foliation of biotite quartz garnet gneiss | Foliated fine-grained biotite and coarse-grained quartz along a fold, separated out into leucosomes and melanosomes. Ilmenite and tschermakite associated with biotite and folded. Sulfides (pyrrhotite) associated with leucocratic material and tschermakite |
| 214907 | GBD011 | 332.35 | Sulfides within foliation of biotite quartz garnet gneiss | Pyrrhotite forms linear discontinuous bands and is generally associated with fine-grained zones of quartz |
| 214908 | GBD011 | 334.1 | Sulfides in biotite quartz gneiss | Quartz and tschermakite with pyrrhotite and trace chalcopyrite |
| 214909 | GBD011 | 333.9 | Au in amphibolite | Disseminated Au in tschermakite groundmass with minor ilmenite and apatite |
| 214910 | GBD011 | 343.55 | Biotite quartz garnet gneiss | Quartz biotite garnet gneiss with minor pyrrhotite |
| 214911 | GBD011 | 343.85 | Biotite quartz garnet gneiss | Sulfides (pyrrhotite and pyrite) rim the outside of garnet crystals and within cracks within a biotite quartz tremolite groundmass |
| 214912 | GBD011 | 346.65 | Mineral banding in a biotite quartz gneiss | Quartz tremolite biotite garnet tschermakite muscovite bands and sulfides (pyrrhotite/chalcopyrite) associated with garnet? |
| 214913 | GBD011 | 348.22 | Amphibolite | Hornblende with minor quartz |
| 214914 | GBD011 | 362.65 | Pyrite overprinting quartz garnet gneiss | Coarse-grained quartz, fine-grained tremolite(?) and garnet. Pyrite within garnet fractures |
| 214915 | GBD013 | 179.1 | Amphibolite | Hornblende and chlorite with minor quartz, plagioclase, biotite and pyrrhotite/chalcopyrite |
| 214916 | GBD013 | 181.96 | Large ~4 cm quartz crystals in quartz plagioclase biotite gneiss | Leucocratic quartz plagioclase bands with minor biotite tschermakite and pyrite |
| 214917 | GBD013 | 187.5 | Folded coarse-grained biotite, quartz and plagioclase gneiss/ migmatite | Biotite, microcline, plagioclase and quartz |
| 214918 | GBD013 | 200.85 | Biotite quartz gneiss with sulfides | Pyrite and pyrrhotite bands within quartz biotite garnet gneiss. Sulfides more often in contact with biotite |
| 214919 | GBD013 | 229.9 | Biotite quartz garnet gneiss | Garnet contains inclusions of biotite and sulfides within fractures, though sulfides are most often associated with biotite. |
| 214920 | GBD013 | 233.95 | Biotite quartz garnet chloriteorite gneiss | Coarse-grained biotite and quartz surrounded by fine-grained quartz, chlorite, biotite, minor garnet, plagioclase, microcline within coarse-grained zones |
| 214921 | GBD013 | 244.65 | Amphibolite band with sulfides | Fine-grained chlorite-altered tremolite(?), dissmeninated pyrite, pyrrhotite, chalcopyrite. Minor muscovite, quartz, plagioclase |
| 214922 | GBD016 | 189.42 | Sulfides associated with biotite quartz chlorite gneiss | Fine-grained hornblende, biotite, tremolite, tschermakite and coarse-grained quartz feldspar, garnet. Larger sulfides (pyrrhotite, chalcopyrite, pyrite) associated with leucocratic material |
| 214923 | GBD016 | 207.54 | Biotite quartz gneiss with sulfides in contact with amphibolite | Coarse-grained quartz feldspar throughout biotite with pyrrhotite,chalcopyrite and replacement pyrite |
| 214924 | GBD016 | 220.19 | Biotite quartz chlorite gneiss | Biotite quartz feldspar gneiss with chlorite-altered amphiboles/ tremolite(?). Minor disseminated sulfides (pyrite, pyrrhotite, chalcopyrite) |

**Drillhole-collar locations**

GBD011: MGA 414566E, 7193743N; Zone 126 lode

GBD013: MGA 4146470E, 7193731N; Zone 126 lode

GBD016: MGA 414563E, 7193675N; Zone 126 lode

# Appendix 2

# Sample information and XRD results

**Table 2.1. XRD samples and results**

| *GSWA number* | *Drillhole number* | *Depth (m)* | *Drillcore description* | *XRD mineralogy* |
|---|---|---|---|---|
| 214901 | GBD011 | 182.3 | Garnet–biotite–quartz gneiss | Almandine (50–60%)<br>Biotite (25–35%)<br>Quartz (5–10%)<br>Pyrrhotite[1] (2–5%)<br>Cordierite (2–5%)<br>Unknown[2] phase (<2%) |
| 214906 | GBD011 | 331.4 | Sulfides within foliation of interleaved quartz–biotite–garnet gneiss and amphibolite | Amphibole (35–50%)<br>Quartz (35–50%)<br>Mica (?biotite, 2–5%)<br>Chlorite (2–5%)<br>Plagioclase (<2%)<br>Pyrrhotite[1] (<2%)<br>Calcite (<2%) |
| 214910 | GBD011 | 343.55 | Quartz–garnet–biotite gneiss | Almandine (35–50%)<br>Quartz (35–50%)<br>Biotite (10–15%)<br>Pyrrhotite1 (2–5%)<br>Amphibole (2–5%)<br>Chlorite (<2%) |
| 214913 | GBD013 | 348.22 | Amphibolite | Amphibole[3] (65–80%)<br>Quartz (10–15%)<br>Amphibole[4] (5–10%)<br>Chlorite (<2%) |
| 214917 | GBD013 | 187.5 | Coarse-grained biotite–quartz–plagioclase gneiss | Biotite (50–65%)<br>Plagioclase (15–25%)<br>Quartz (10–15%)<br>Chlorite (<2%) |

**NOTES:**

1 Confirmed by heating to 575° — pyrrhotite converts to hematite

2 Very small peaks at 7.14 Å and 3.55 Å which disappear when heated to 575°C (chlorite?); very small peak at 6.14 Å which disappears when heated to 575°C (unidentified mineral)

3 XRF analyses on this sample yielded high Ca, Fe and Al and are consistent with a Ca–Fe–Al amphibole (hornblende)

4 Composition based on XRF analyses on this sample. Second amphibole consistent with another calcic amphibole, perhaps a retrograde calcic amphibole like tremolite–actinolite

# Appendix 3

# HyLogger downhole logs

## Introduction

The main HyLogger mineral groups identified within the core have been displayed downhole (X axis in metres). ‘Count’, on the Y axis, is the number of times the specific mineral has been measured per metre interval of core.

Gold assay intervals have been included where available. Grey rectangles highlight regions of higher gold grade throughout the graphs.

Where available, simplified core logging has also been incorporated.

## Rock Chip pre-collars

The HyLogger scans each chip tray twice; hence, the count rate is always two. Rock Chip scanning is only available in the VNIR and SWIR wavelengths. This means minerals only visible in the TIR (e.g. plagioclase, garnet and quartz) are not detectable.

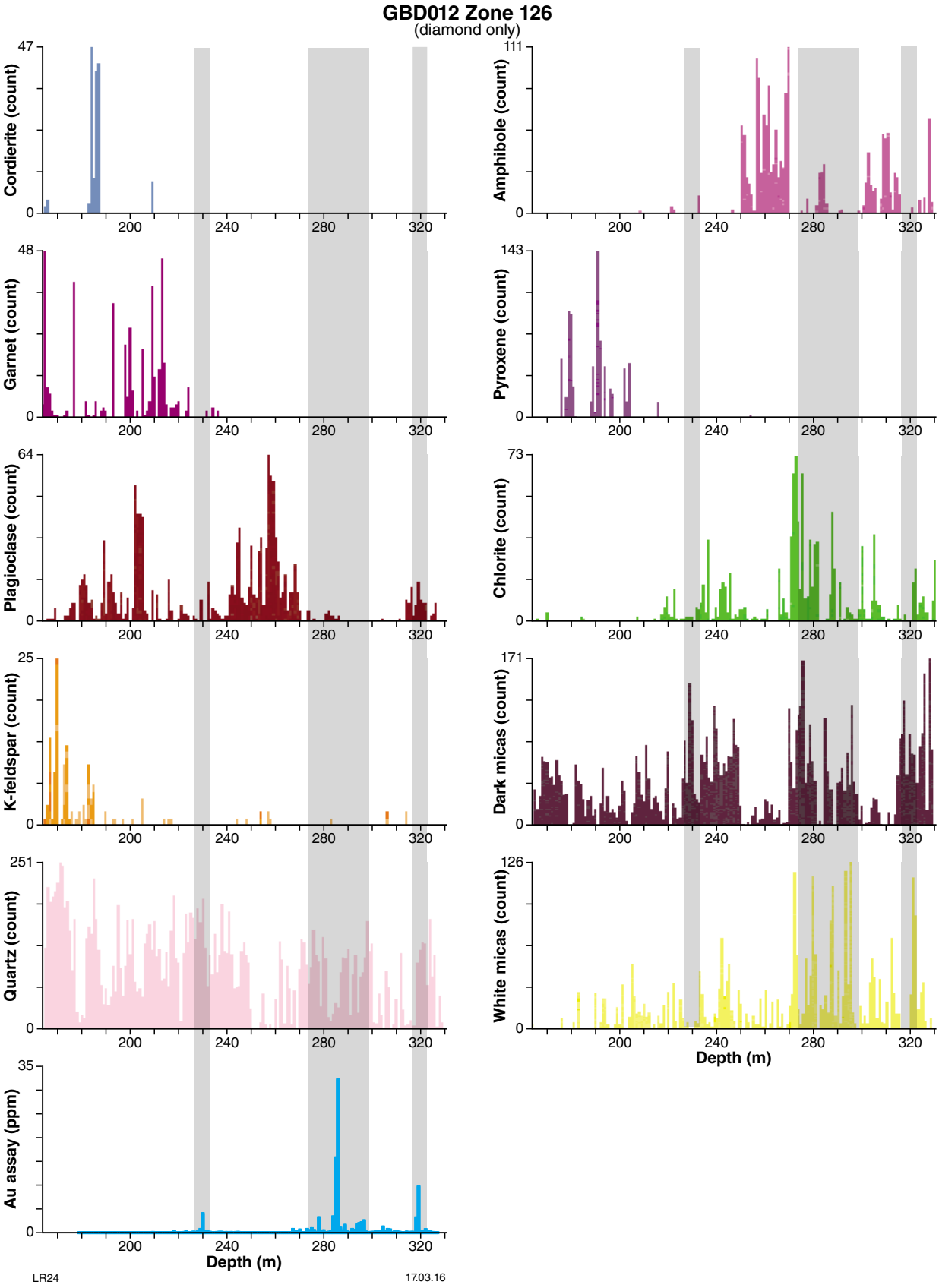


**Figure 3.1. HyLogger results for diamond drillhole GBD012 at Zone 126, highlighting each major mineral group relative to gold content. Regions of high gold grade have been highlighted by grey shaded regions. Count rate specifies how many times the sample was found in a metre interval. This shows that there is no obvious relationship between gold grades and specific minerals.**

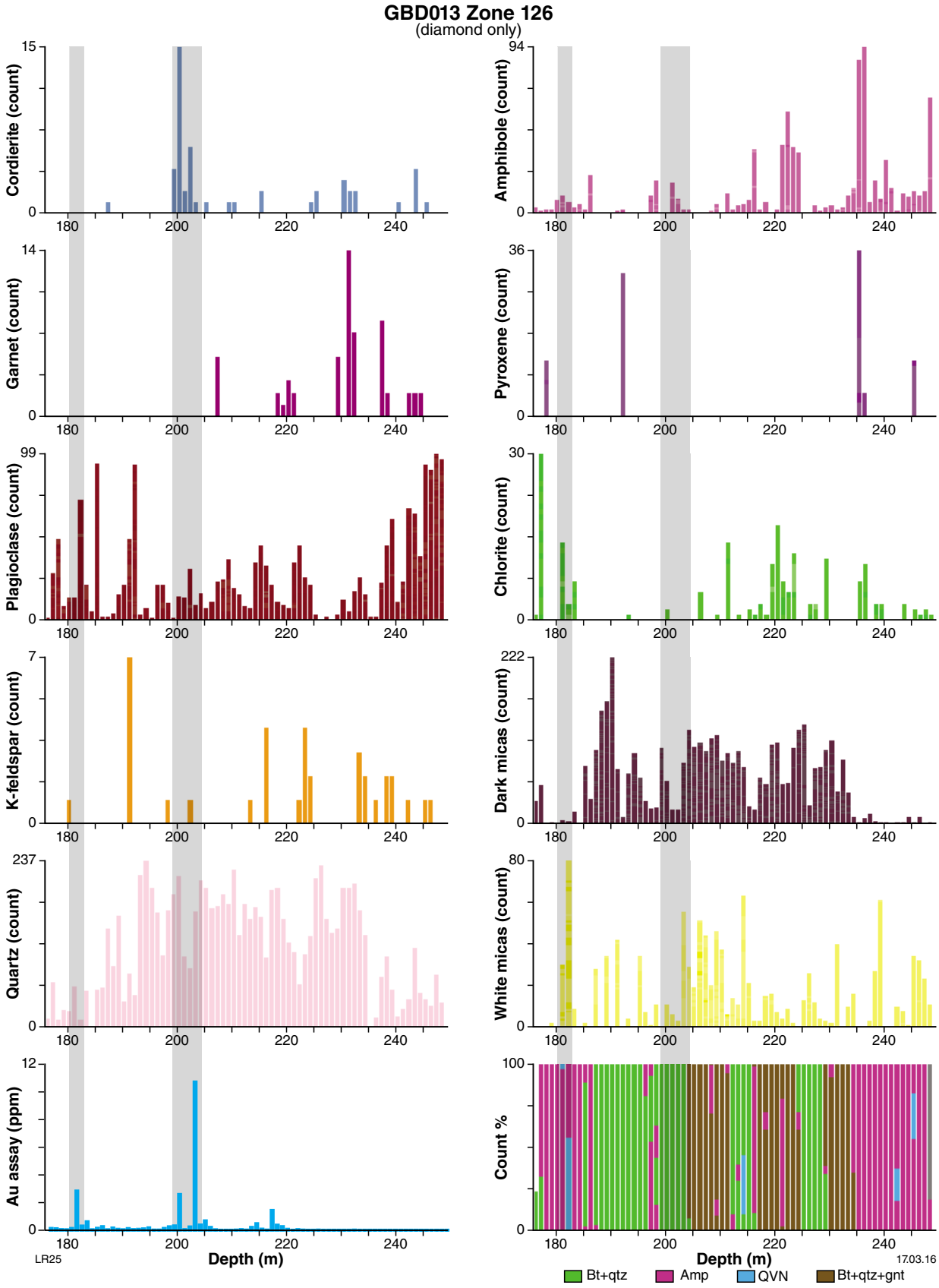


**Figure 3.2. HyLogger results for diamond drillhole GBD013 at Zone 126, highlighting each major mineral group relative to gold content. Regions of high gold grade have been highlighted by grey shaded regions. Count rate specifies how many times the sample was found in a metre interval. This shows that there is no obvious relationship between gold grades and specific minerals. Simplified lithological logging was added (lower right) including bt+qtz, biotite–quartz–gneiss; Amp, amphibolite; QVN, quartz vein; and bt+qtz+gnt, biotite–quartz–garnet gneiss.**

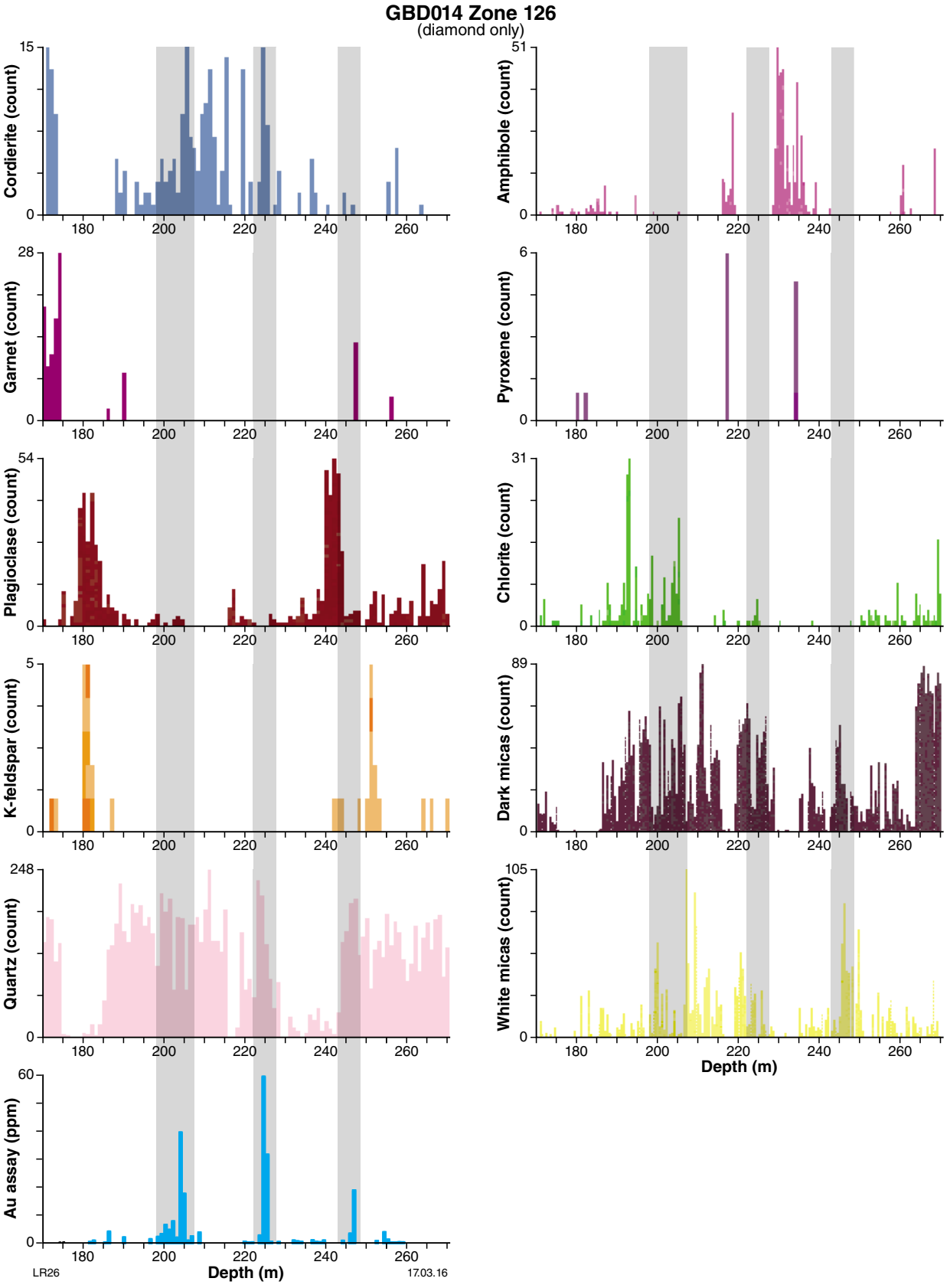


**Figure 3.3. HyLogger results for diamond drillhole GBD014, highlighting each major mineral group relative to gold content. Regions of high gold grade have been highlighted by grey shaded regions. Count rate specifies how many times the sample was found in a metre interval. This shows that there is no obvious relationship between gold grades and specific minerals.**

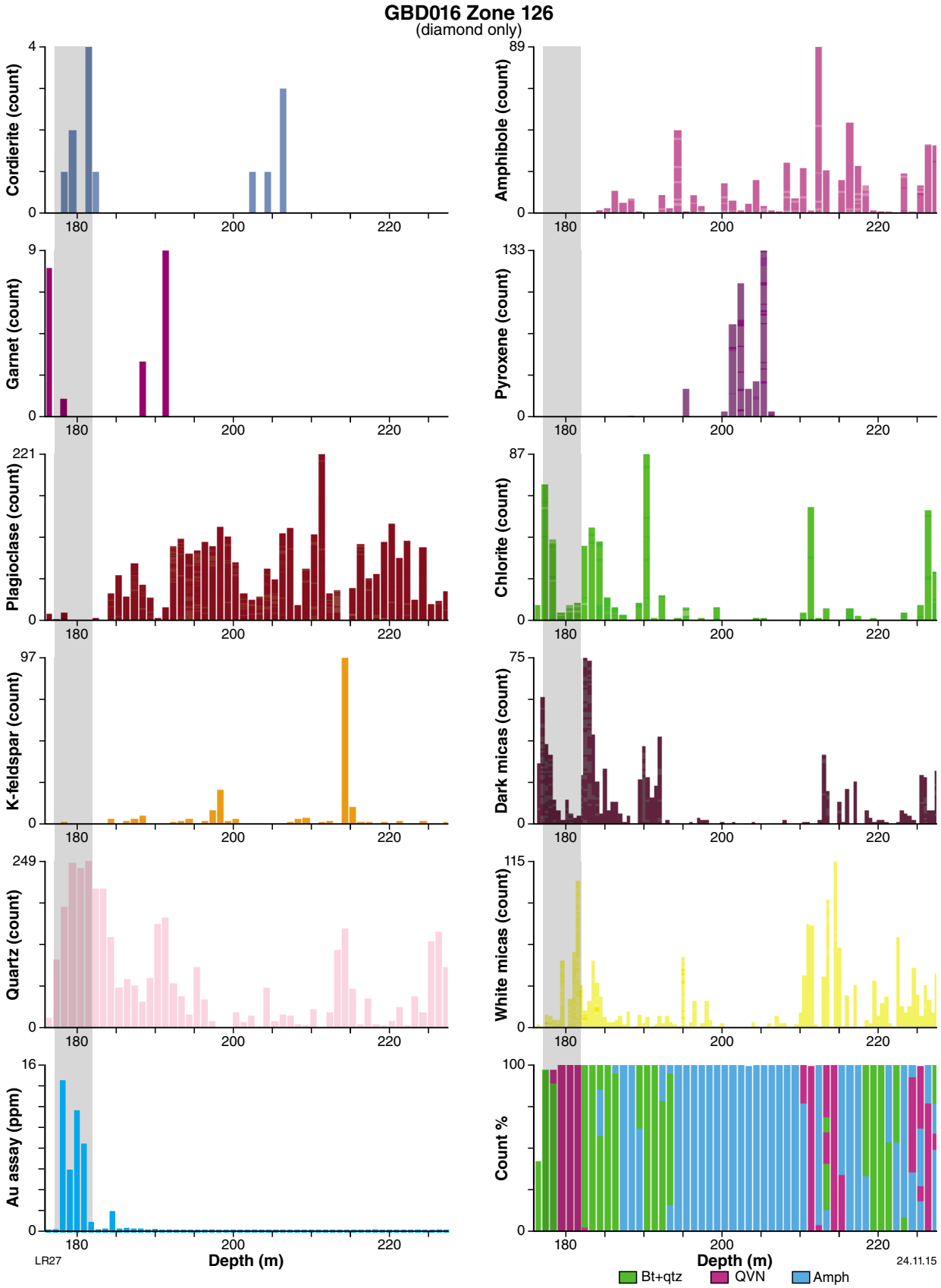


**Figure 3.4. HyLogger results for diamond drillhole GBD016 at Zone 126, highlighting each major mineral group relative to gold content. Regions of high gold grade have been highlighted by grey shaded regions. Count rate specifies how many times the sample was found in a metre interval. This shows that there is no obvious relationship between gold grades and specific minerals. Simplified lithological logging was added (lower right) including bt+qtz, biotite–quartz–gneiss; QVN, quartz vein; and Amp, amphibolite.**

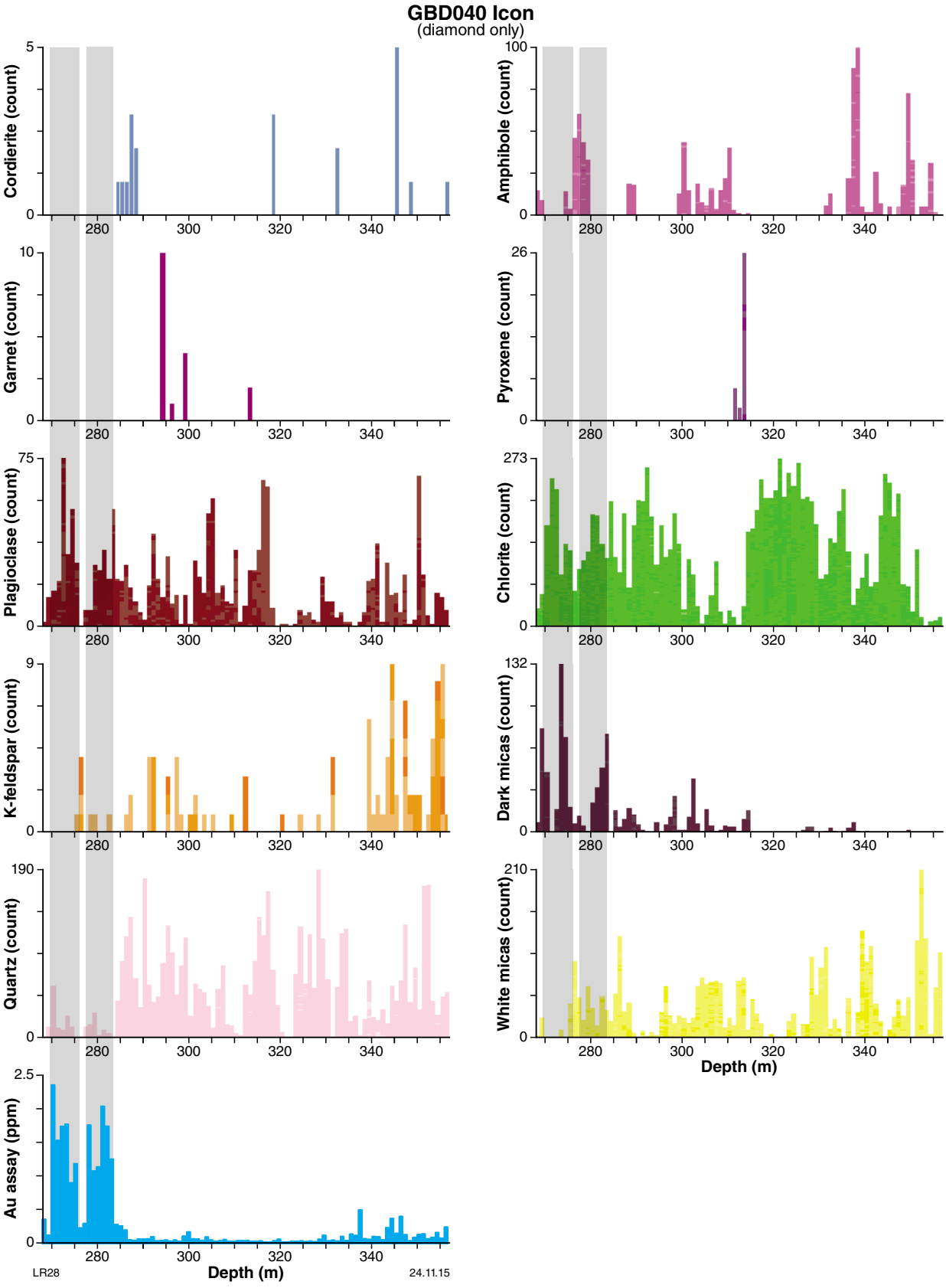


**Figure 3.5. HyLogger results for diamond drillhole GBD040 at Icon, highlighting each major mineral group relative to gold content. Regions of high gold grade have been highlighted by grey shaded regions. Count rate specifies how many times the sample was found in a metre interval. This shows that there is no obvious relationship between gold grades and specific minerals.**

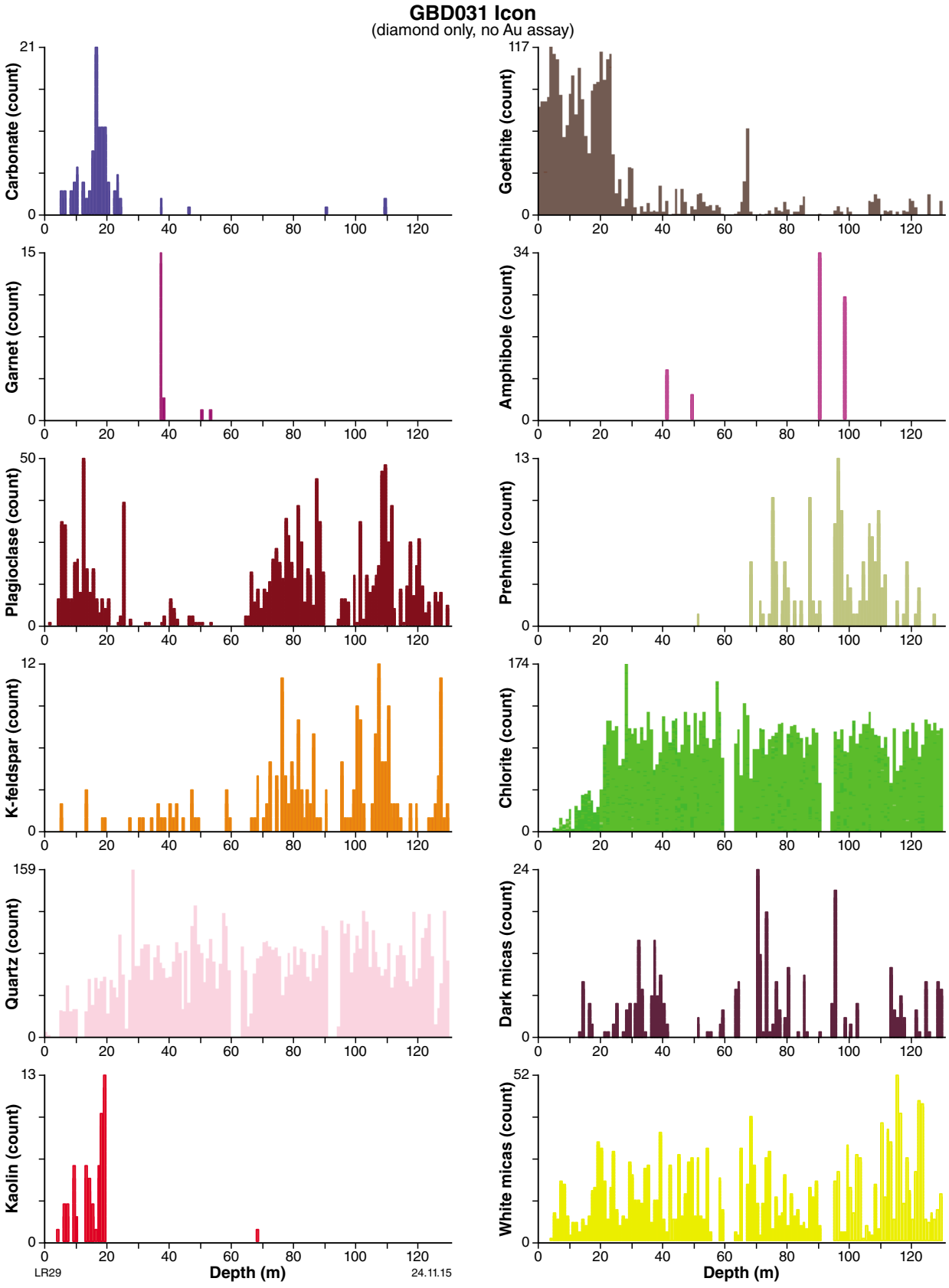


**Figure 3.6. HyLogger results for diamond drillhole GBD031 at Icon, highlighting each major mineral group downhole. No assays available for this hole. Count rate specifies how many times the sample was found in a metre interval.**

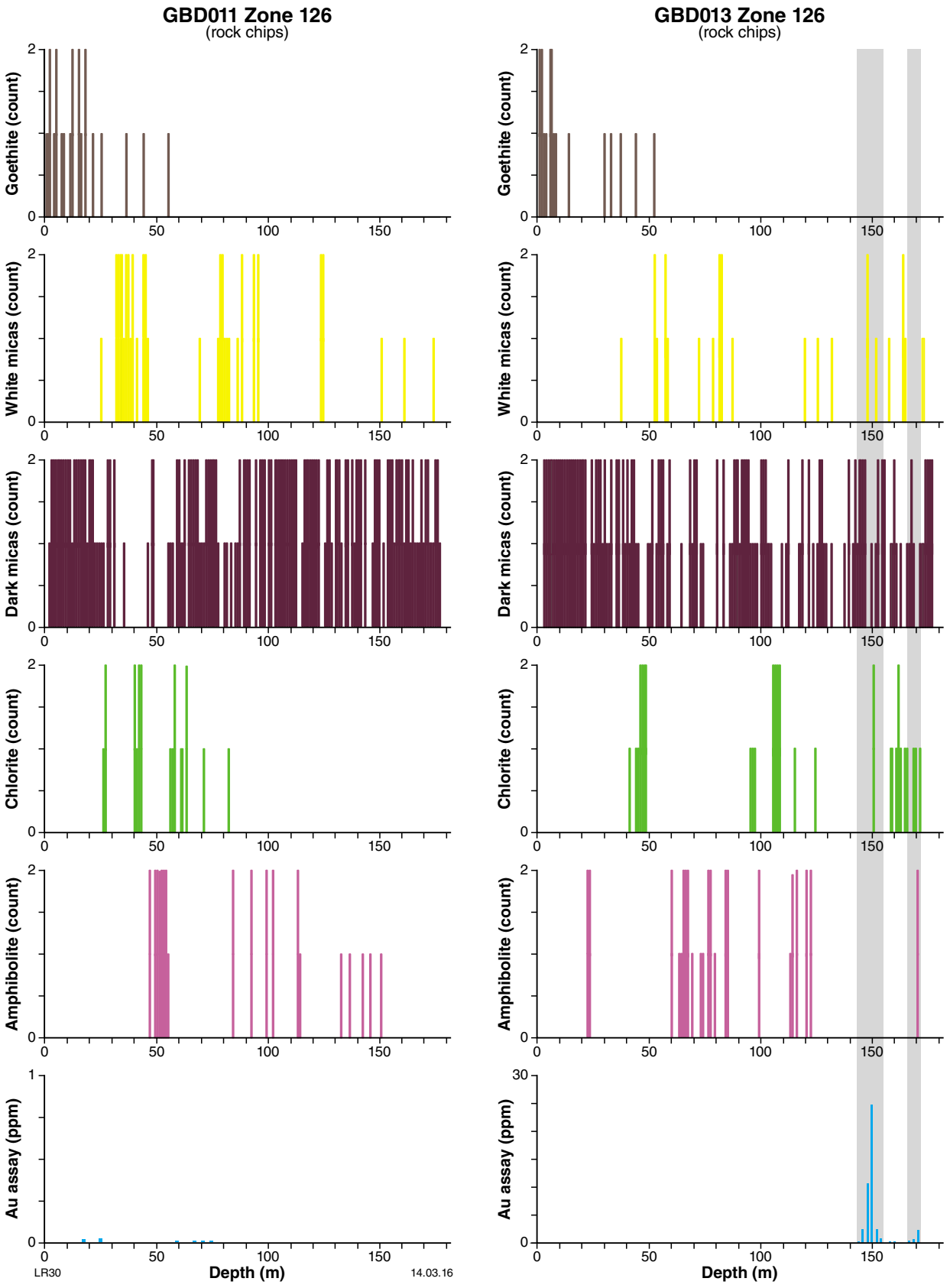


**Figure 3.7. HyLogger results for reverse circulation pre-collar chips GBD011 (left column) at Zone 126 and GBD013 (right column) at Zone 126. Each major mineral group relative to gold content was highlighted. Regions of high gold grade have been highlighted by grey shaded regions. Count rate specifies how many times the sample was found in a metre interval. Note that each chip tray can only be scanned twice and hence count rate has a maximum of two. This shows that there is no obvious relationship between gold grades and specific minerals.**

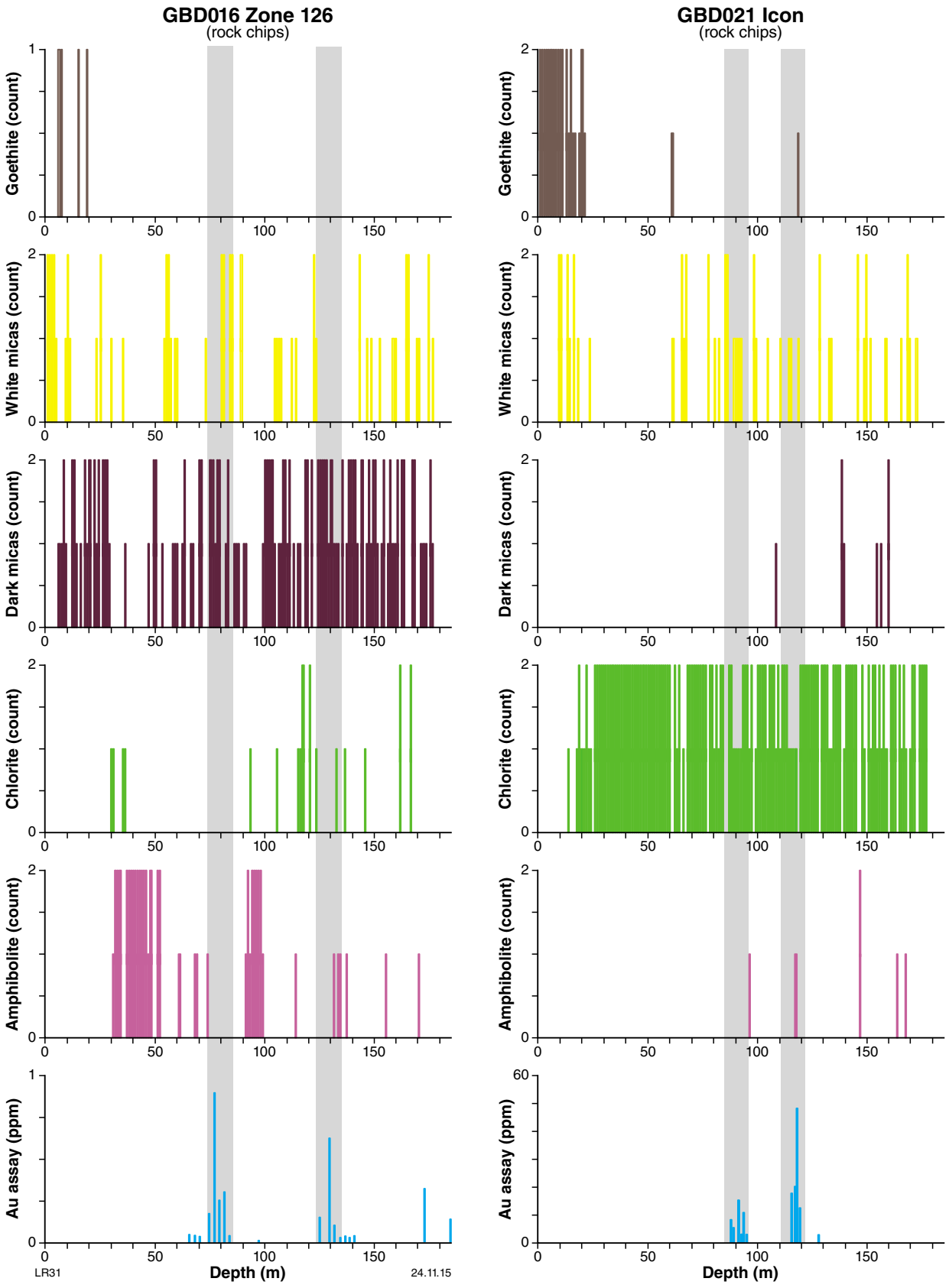


**Figure 3.8. HyLogger results for reverse circulation pre-collar chips GBD016 (left column) at Zone 126 and GBD021 (right column) at Icon. Each major mineral group relative to gold content was highlighted. Regions of high gold grade have been highlighted by grey shaded regions. Count rate specifies how many times the sample was found in a metre interval. Note that each chip tray can only be scanned twice and hence count rate has a maximum of two. This shows that there is no obvious relationship between gold grades and specific minerals.**

This report is the culmination of work conducted as part of the Geological Master's Program through the Geological Survey of Western Australia (GSWA). Gold deposits are rare in upper-amphibolite to granulite facies environments. Known examples commonly attract debate about whether they formed at these high temperatures, or instead represent metamorphosed, metasomatic or superimposed (retrograde) mineralization. The one-million ounce Glenburgh gold deposit formed in the Paleoproterozoic, upper-amphibolite to granulite facies Glenburgh Terrane in the southern Gascoyne Province of Western Australia.

Evidence from field mapping, visual and hyperspectral logging of drill samples, thin-section petrography, gold-microstructure analysis and zircon U–Pb geochronology of the Zone 126 and Icon lodes at the Glenburgh deposit demonstrates that this is a metamorphosed gold deposit. Features within the internal structure of gold grains, such as high-purity gold veinlets, incoherent twinning and low silver content, suggest the gold has been through postdepositional processes such as metamorphism and deformation. The presence of rounded sulfide inclusions within almandine, a peak metamorphic mineral, illustrates there was a sulfide phase present prior to the peak of metamorphism. The lack of a definitive alteration assemblage further suggests that the alteration assemblage and mineralization were recrystallized and perhaps remobilized during deformation and metamorphism. Geochronology data based on U–Pb indicates that mineralization must have formed later than c. 2035 Ma — the maximum depositional age of the metasedimentary host rocks — and prior to c. 1991 Ma — the peak of metamorphism during the Glenburgh Orogeny.

Further details of geological products and maps produced by the Geological Survey of Western Australia are available from:

Information Centre
Department of Mines and Petroleum
100 Plain Street
EAST PERTH WA 6004
Phone: (08) 9222 3459  Fax: (08) 9222 3444

www.dmp.wa.gov.au/GSWApublications

ROCHE

UNRAVELLING THE UPPER-AMPHIBOLITE FACIES GLENBURGH GOLD DEPOSIT, GASCOYNE PROVINCE — EVIDENCE FOR METAMORPHOSED MINERALIZATION

REPORT 155